SPREADING AND JAMMING PHENOMENA OF PARTICLE-LADEN INTERFACES

by

Hsin-Ling Cheng

B.S., National Tsing Hua University, 2000

M.S., National Tsing Hua University, 2002

Submitted to the Graduate Faculty of

Swanson School of Engineering in partial fulfillment

of the requirements for the degree of

Doctor of Philosophy

University of Pittsburgh

2009

UNIVERSITY OF PITTSBURGH

SWANSON SCHOOL OF ENGINEERING

This dissertation was presented

by

Hsin-Ling Cheng

It was defended on

July 10, 2009

and approved by

Di Gao, Ph.D., Assistant Professor, Department of Chemical and Petroleum Engineering

Prashant N. Kumta, Ph.D., Professor, Departments of Bioengineering, Chemical and

Petroleum Engineering, Mechanical Engineering and Materials Science, Oral Biology

Stephen Garoff, Ph.D., Professor, Department of Physics (Carnegie Mellon University)

William J. Federspiel, Ph.D., Professor, Departments of Chemical and Petroleum

Engineering, Surgery, Bioengineering

Dissertation Director: Sachin S. Velankar, Ph.D., Associate Professor, Department of

Chemical and Petroleum Engineering

SPREADING AND JAMMING PHENOMENA OF PARTICLE-LADEN INTERFACES

Hsin-Ling Cheng, PhD

University of Pittsburgh, 2009

Partially wettable particles tend to adsorb irreversibly at interfaces of two immiscible fluids. The fluid-fluid interface can be the oil-water interface such as in an emulsion, or the polymer-polymer interface such as in a binary polymer blend. This work aims to have fundamental understanding on two interface-attributed phenomena and then to demonstrate the applications.

A spreading event against the direction of gravity of particle-fluid films, termed as film-climbing, occurs as a result of drop coalescence in an unstable Pickering emulsion. We study the generality of this phenomenon, confirm the film structure, and investigate effects of substrate hydrophobicity and prewetting. The calculation and measurement of surface pressure, as well as a wall-coverage calculation are provided to support the proposed mechanism.

We develop the spinning drop tensiometer method to conduct a systematic study on interfacial-tension-driven jamming. Specific interfacial area is correlated to a particle packing model. We identify the important characteristics for jamming such as hysteresis and dynamics-dependence. The difference between jamming of polar-nonpolar and nonpolar-nonpolar fluid interfaces is contrasted.

For applications of jamming, we first demonstrate that the interfacial jamming can stabilize a bicontinuous morphology. Hand-blending a partially miscible system of polyisoprene (PI) and polyisobutylene (PIB) produces an evolving bicontinuous morphology. Interfacially-

active particles are added to affect the domain coarsening rate. A bicontinuous, jammed structure (a.k.a. bijel) is realized.

Interfacial jamming also affects the morphology of a droplet-matrix blend of PI and polydimethylsiloxane (PDMS). We use the drop coalescence induced by shear flow to generate elongated drops. Particle jamming on drop surface affects the relaxing kinetics of elongated drops. We utilize rheology as the tool to trace the drop relaxation and drop size change, as well as the elastic recovery of blends after cessation of shear flow. Another focus of PI/PDMS blends is the observation of particle-assisted network structures as we increase particle loading. The stabilization of network structures is attributed to interfacial effect.

With these examples on polymer blends, we show the applications of jamming on creating particle-polymer composite materials of desired morphologies.

TABLE OF CONTENTS

vi

LIST OF TABLES

LIST OF FIGURES

xiv

PREFACE

I would like to express my deep gratitude to my advisor Dr. Sachin Velankar for his support, advice and patience. He created enjoyable learning environment and imparted knowledge to me, and most importantly, shared the constant enthusiasm for research with me. I am also very grateful to my committee members, Dr. Federspiel, Dr. Gao, Dr. Garoff and Dr. Kumta for their encouragement, valuable suggestions and helpful insight into my work.

I thank the members of my group: Dr. Jeffery Martin, Dr. Prachi Thareja, Candice DeLeo; they were not only helpful in experiments and discussion but also made my life in the lab enjoyable and memorable. I would also like to thank my undergraduate colleagues (Melissa, Sean, Patrick, Danielle and Brian) who worked closely with me in various projects. Especially, I thank Brian Novicki for his contribution in part of the phase continuity tests and shear cell experiments in chapter 6.

I also thank Dr. John Barnard for generously providing us the access to the pendant drop apparatus and AFM, and Dr. Srinivasa Raghavan in University of Maryland for the access to an environmental SEM. I would also take this opportunity to thank my former advisor, Dr. Martin Lo in University of Maryland for encouraging me to pursue research directions of my own interest while I was there. The one-year PhD education in Food Science made me gain independence in research and became my cherishable memory.

Finally, I would share the joy of completing the dissertation with my family and my friends. I thank my parents (Mr. Kuo-Chen Cheng and Mrs. Mei-Ying Chang) for their unconditional love and faith, and my husband Cheng-Chun for the mutual support during our "adventures" in the US. This dissertation is dedicated to my husband and forever sunshine, Dr. Cheng-Chun Chang.

1.0   INTRODUCTION

Since the beginning of the twentieth century, it has been known that particles are capable to stabilize emulsions. Such emulsions are called Pickering emulsions[1]. The detailed mechanism was however not understood until the resurgence of researches on particle-laden interfaces in the past two decades.

Driven by the fundamental interests on particle behaviors or particle monolayer behaviors, numerous studies have given a deep insight on interparticle interaction whose influence on monolayer microstructures is enhanced by the presence of fluid meniscus[2, 3]. Due to the confinement effect of interface, interesting monolayer properties such as buckling with a finite wavelength[4], and jamming with nonspherical drop shapes[5] have just begun to be elucidated.

The applications of particle stabilization in emulsions and foams were continuously being pursued to realize long-term stability[6, 7], and have been extended to polymer foams[8] for enhanced mechanical properties. It has also been proposed that the interstitial space between close-packed particle monolayer on droplets can be selectively permeable to their contents in the so-called "colloidosomes" delivery vehicles[9].

More recently, the appreciation of using interfacial-assembly[10, 11] or interfacial jamming[12] to fabricate morphologies or structures that are otherwise difficult to achieve[13] has made particle-laden interfaces one of the advancing research fields. On the merging of colloids science,

surface science, polymer science and nanotechnology[14], more interfacial composite materials such as "bijels[12]" and "armored bubbles[15]" are expected to be possible and expected to draw more attention.

This thesis covers two phenomena of particle-laden interfaces—spreading (chapter 3) and jamming (chapter 4, 5, 6). Contrasting to each other, these two phenomena of particle-laden interfaces occur at the two particle concentration extremes of a particle monolayer. The spreading of a particle-fluid film occurs only when the interfacial particle concentration is sufficiently low and thus permits drop coalescence in a Pickering emulsion, while the jamming of fluid-fluid interfaces is to describe the situation when the interface loses mobility and displays solidlike characteristics due to sufficiently high concentration of particle adsorption. Table 1 shows the structure of the thesis. An overview of the organization of thesis is given as follows.

Table 1. Organization of this dissertation.

In chapter 3, a film-climbing phenomenon[16] resulting from an unstable Pickering emulsion is studied. Such a spreading event occurs when the droplet surfaces of a particle-

containing emulsion have incomplete particle coverage, and hence drop coalescence with an oil lens is permitted. A local surface pressure gradient induced by drop coalescence then drives a particle-fluid film to climb up on the glass wall in a vial, even though the gravity is in the opposing direction.

In chapter 4, we conduct a systematic study of interfacial-tension-driven jamming of a particle monolayer using a spinning drop tensiometer[17] (SDT). In a SDT, an oil drop surrounded by an immiscible fluid, ethylene glycol, is spun into a cylindrical shape. We decrease rpm and thus decrease interfacial area indirectly via the drop retraction driven by interfacial tension. With a fixed particle amount at the interface, jamming is induced as area decreases.

After the two fundamental studies of particle-laden interfaces in chapter 3 and chapter 4, we apply the concept of interfacial jamming to affect and control the morphology of two polymer blend systems in chapter 5 and chapter 6.

In chapter 5, we found that hand-mixed PI/PIB polymer blend has a bicontinuous morphology whose domain size coarsens with time. We use interfacially-active particles to affect the domain coarsening rate. As the domain coarsens, the interfacial area decreases and jamming is induced. A bicontinuous, jammed structure (a.k.a. bijel) is realized.

Hand-mixed PI/PDMS polymer blends have a droplet-matrix morphology. In chapter 6, we use drop coalescence induced by flow conditions to generate elongated drops. We observe that particle-coated elongated drops do not relax their shape over time, which is a signature of interfacial particle jamming. We utilize rheology as the tool to trace the drop relaxation and the change of the mean drop size, as well as the elastic recovery of the blend after cessation of shear stress.

Another highlight of chapter 6 is the observation of a particle-assisted network structure in the PI/PDMS blend which is known to have a simple droplet-matrix morphology. The

network structure is stable over time.   After careful examination of particle-free blends, we observe the existence of a very transient bicontinuous structure immediately after blending. The reason of its formation is discussed. We attribute the stability of the particle-assisted network structures mainly to interfacial effect.

Chapter 5 and chapter 6 together show that interfacial particle jamming not only determines the stabilized and arrested structure in a bicontinuous morphology, but also regulates the blend morphology in a droplet-matrix blend.   The applications of jamming are well demonstrated.

We conclude the thesis with summary and future work in chapter 7.

2.0   BACKGROUND

In Section 2.1, we give an overview of particle adsorption at fluid-fluid interfaces.   The consequences of particle adsorption: monolayer formation, interparticle interaction and Pickering emulsions will be introduced.   In Section 2.2, we discuss the properties of particle monolayers, which are relevant to the spreading behavior and the jamming behavior. We then switch focus to macromolecular fluid-fluid interfaces, i.e. the interface in polymer blends. In Section 2.3, we give background information on the morphology development of a droplet-matrix morphology and a bicontinuous morphology for particle-free polymer blends.   In Section 2.4, we introduce the bijel, which is a relatively-new composite material. In Section 2.5, the rheology method for polymer blends is covered.

2.1   PARTICLE ADSORPTION AT FLUID-FLUID INTERFACES

The contact angle is the angle at which a fluid-fluid interface meets the solid surface. Particles that have moderate affinity (i.e. partial wettability) towards two immiscible fluids tend to adsorb at the fluid-fluid interface while fulfilling the equilibrium contact angle (Figure 1). Partially wettable particles are confined in the 2D space (i.e. interface) because there is an energy benefit (i.e. the free energy of the system is lower) compared to when they are in the bulk fluids. This

benefit arises because the particle at interface replaces a certain area of the unfavorable fluid-fluid interface.
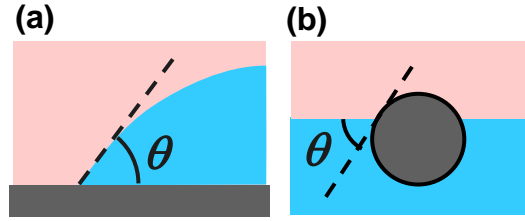
Figure 1. Schematic representation for (a) Contact angle θ. (b) A partially wettable particle at fluid-fluid interface.

The energy required to remove one particle from the interface (i.e. desorption energy) is $\pi R^2 \alpha_{AB} (1 \pm \cos\theta)^2$, where R is particle radius, θ is the contact angle, and α_{AB} is the interfacial tension between fluid A and B. In Figure 2, the energy required to move a hydrophilic particle ($0° < \theta < 90°$) into the oil phase, $\pi R^2 \alpha_{AB} (1 + \cos\theta)^2$, is larger than that needed to move it into water phase, $\pi R^2 \alpha_{AB} (1 - \cos\theta)^2$. Assuming some reasonable values for R (e.g. R ≥ 10 nm), α_{AB} (e.g. 20 mN/m) and θ (e.g. ~ 90°), the desorption energy calculated is generally several orders larger than thermal motion energy, characterized by $k_B T$. This implies that particles cannot be removed from the interface by thermal motion alone. Particle adsorption to the interface is generally considered to be irreversible.
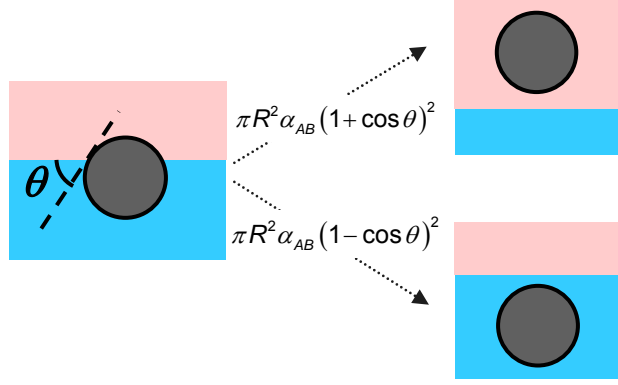
Figure 2. Schematic representation of particle desorption and the associated desorption energy.

θ is the equilibrium contact angle.

2.1.1 Particle monolayer, interparticle attraction

In a two-dimensional microscopic view, the ordered or random attachment of particles to the fluid-fluid interfaces forms particle monolayers of variable interfacial particle concentrations. The maximum concentration would be of 2D close packing, or a packing density of 0.91 for monodisperse, spherical particles (see Figure 3b). The interstitial space renders size sieving ability to the particle monolayer, and the monolayer is selectively permeable[9, 11]. The structure of monolayers is determined by interparticle interaction. When the system is dominated by interparticle repulsion, monodisperse and spherical particles forms ordered 2D lattice, as shown in Figure 3c.
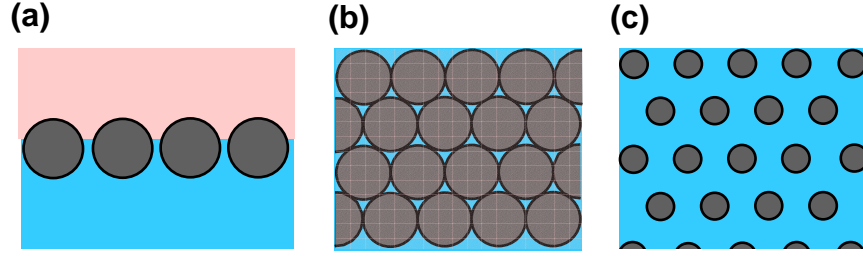
Figure 3. Schematic representation for particle monolayer.

(a) Sideview of a particle monolayer. (b) Topview of a close packed particle monolayer of monodisperse spherical particles. (c) Topview of an ordered particle monolayer of monodisperse spherical particles where interparticle repulsion keeps the particles apart.

The interparticle attraction at fluid-fluid interface is different from the interaction in single phase bulk fluid due to the additional capillary contribution. For charged particles at the interface, particles can also repel each other. The interparticle repulsion is discussed in Section 2.2.1. We are focusing the discussion on interparticle attraction for the current section.

While particles are confined at the interface, the particles attract each other through two possible mechanisms. The first one is through van der Waals interaction. The van der Waals interaction between two particles is the summation interaction of all atoms or molecules considered. The second mechanism is called capillary interaction. The origin of the lateral interaction between two particles at a liquid interface is the overlap of perturbations in the shape of a liquid surface due to the presence of attached particles[18]. As shown in Figure 4a, for large particles floating at a liquid interface, the particle weight causes the interfacial deformation. The gravitational potential energy of two particles decreases as they approach each other, and the force arisen is called flotation capillary force. For smaller particles, say radius < 5 μm, their weight cannot deform the liquid interface significantly, so there is no flotation capillary force[18]. However, if the three-phase (solid- fluid 1- fluid 2) contact line is somehow undulated, for

example due to particle surface roughness or due to local heterogeneity of particle chemistry, the convex and concave local deviations of the meniscus shape from planarity can be treated as capillary charges. Therefore, the capillary multipoles[18, 19] would determine the attraction force between two small particles.
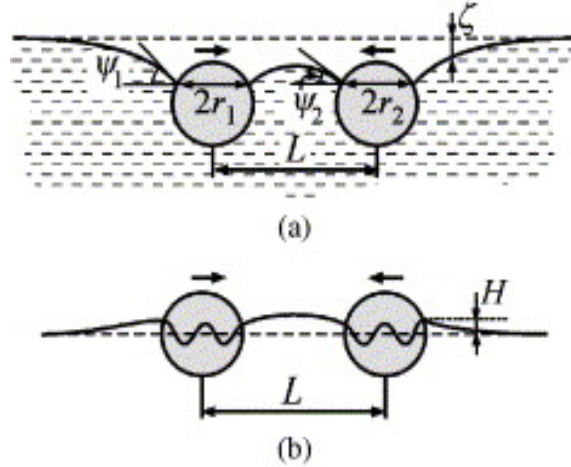
Figure 4. Lateral capillary forces between floating particles.

(a) Flotation capillary force for heavy particles. (b) Capillary force for small particles caused by an undulated

contact line. Reprinted with permission from (Ref. 19). Copyright (2005) Elsevier Inc.

The capillary attraction force at longer distance between spherical particles is proportional to d^{-4}, and therefore it is considered as a long range force (as compared to the van der Waals force). Loudt et al.[20] studied the capillary attraction between anisotropic colloidal particles and found that the attraction force was shape-dependent. Two micron-sized polystyrene or silica-coated ellipsoids were found to attract and approach each other at distance of tens of microns apart, while the interaction between spherical particles with the same surface chemistry was weaker. They suspected that the shape anisotropy of the ellipsoids produces more complex interfacial distortions and therefore leads to stronger capillary interactions[20]. Due to the

interparticle attraction, under conditions when the attraction force dominates, particles can form aggregated structure at the fluid-fluid interfaces[21].

2.1.2 Pickering emulsions

An emulsion is a mixture of two immiscible fluids, in which one fluid is dispersed as droplets in another fluid. Emulsions do not form spontaneously; energy input such as shaking must be provided to create this metastable or unstable state. Once an emulsion is formed, drop coalescence would occur to decrease the total interfacial area as well as the interfacial energy of the system, unless an emulsifier species is added to stabilize the emulsion. In Pickering emulsions, particles serve as emulsifiers instead of surfactants. In the section, we discuss factors that affect the stability of Pickering emulsions, including particle wettability and particle size. We then discuss two possible stabilization mechanisms and their relationship to the particle coverage on drop surface, which is also related to the stability of emulsions.

The particle wettability effect on stability of emulsions was studied by Binks and Lumsdon[22] on the system of fumed silica powders at water-toluene interface. They found that emulsions stabilized by particles of intermediate wettability (i.e. neither very hydrophilic nor very hydrophobic) were stable. They related the observations to the consideration of adsorption/desorption energy of particles[22, 23]. Particles of intermediate wettability adsorb efficiently at interface and have a strong capability to resist desorption, and therefore result in a stable emulsion. In addition, the wettability of particles also partially determines the emulsion types[22]. When the volume ratio of fluids is close to the phase inversion point, relatively

hydrophilic particles tend to stabilize oil in water (o/w) emulsions; relatively hydrophobic particles tend to stabilize water in oil (w/o) emulsions[24].

Particle size affects the size of drops formed in the emulsion. Binks and Lumson[25] investigated the effect of PS latex particles size for water/cyclohexane emulsions. They found that the average emulsion drop size increased with increasing particle size but the correlation then leveled off[25]. Because large drops tend to concentrate towards the surface or bottom of the emulsion depending on the relative density of the two phases, which is a phenomenon known as creaming, smaller particle size is beneficial for emulsion stability as long as the correlation between the particle size and drop size holds.

The most common stabilization mechanism of Pickering emulsions is concerned with the mechanical strength of particle layers. As shown in Figure 5b, the particle monolayer on each drop formed by particle adsorption serves as a steric barrier against drop coalescence, and thus stabilizes an emulsion. In recent years, it is found that if the contact angle permits particles to span over the *liquid 1-liquid 2* and *liquid 2-liquid 1* interfaces (i.e. particle bridging), stabilization of emulsion can be achieved even though the drops have surface coverage far from completeness[26] (see Figure 5c). In the particle bridging scenario, as two drops with dilute particle monolayers come close to each other, a dense particle monolayer in "disc" shape would form in the contact region as a result of strong capillary attraction caused by the menisci around them. This bridging event only occurs when the contact angle is away from 90°, for example 152°[26] and 130°[27, 28]. In most situations, high particle coverage on the drops is believed to be required to suppress drop coalescence efficiently. In short, the particle coverage on drops determines the stabilization mechanism and also affects the stability of emulsions.
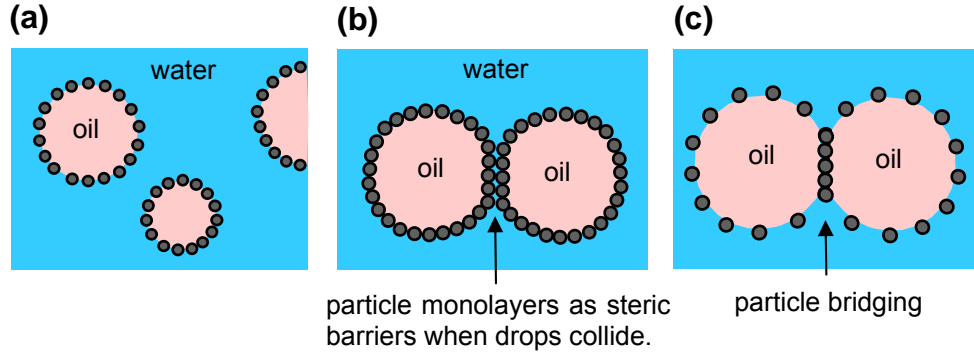
Figure 5. Schematic representation of a Pickering emulsion and its two stabilization mechanisms.
(a) Pickering emulsion (b) Steric stabilization due to the mechanical strength of particle monolayers (c) Bridging stabilization due to formation of a dense particle monolayer at the contact region.

2.2 PROPERTIES OF PARTICLE MONOLAYERS AT OIL-WATER INTERFACE

Due to the interparticle interaction at the fluid-fluid interface and the confinement effect (i.e. particles are trapped at interface), particle monolayers possess unique properties that contribute to the spreading and jamming phenomena. We first discuss the interparticle repulsion, which is the driving force of spreading. We then discuss the elasticity of particle monolayers, i.e. the buckling of monolayer under an external compression.

2.2.1 Interparticle repulsion and spreading pressure

Depending on the interparticle interaction, particle monolayers can display different spatial arrangements. If particles have experienced the attraction interaction between particles, they can form aggregated structures. When interparticle interaction is dominated by repulsion, particles

can form a highly ordered monolayer in a confined area. The interparticle repulsion is also the driving force for a spreading event. It can be measured as a quantity called surface pressure (viz. spreading pressure). In the following, we discuss the mechanism of repulsion, effect of salt and effect of wettability of particles, and then discuss how surface pressure is quantified.

Pieranski[3] noted first that the repulsion interaction between charged particles adsorbed at air/water or oil /water interface was enhanced over that interaction of particles in bulk solutions. He attributed the long-ranged ordering of particle monolayers to dipole-dipole repulsion between the particles. In his hypothesis, each particle possesses a dipole moment perpendicular to fluid interface due to the asymmetric distribution of counterions near the particles[3].

Later, Aveyard, et al.[29] studied the adsorption of polystyrene (PS) latex particles at air/water and octane/water interface. They found that there was a strong dependence of monolayer structure at air/water interface on the salt (sodium chloride) concentration, while particle monolayers at the octane/water interface remained highly ordered even on a concentrated salt solution. The difference of the salt effect on these two systems led them to hypothesize that the long-range repulsion results from Coulombic repulsion of the residual charges in the residual water trapped on the oil-side of particle surface due to particle roughness (see Figure 6).
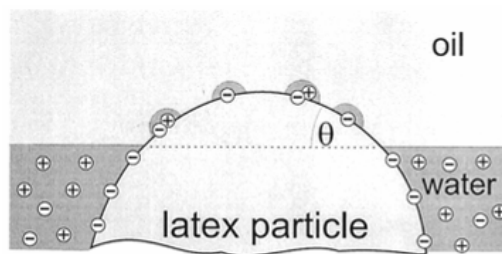
Figure 6. Schematic representation of residual charges with the residual water trapped on the oil-side of particle surface due to particle roughness. Reprinted with permission from (Ref. 29). Copyright (2000) American Chemical Society

13

Horozov, et al.[21] studied the effect of particle wettability on the microstructure of particle monolayers using monodisperse surface-modified silica particles at octane-water interface. Microscope observation showed that there was an order-disorder transition of the monolayer structure in a narrow interval of contact angle (between 115° and 129°). Disordered monolayers have random particle aggregates that may have a fractal like structure. In addition, their calculation suggested that Coulombic repulsion acting through the oil phase was the source of ordering of monolayer and the order-disorder transition. This was consistent with the earlier hypothesis of Aveyard, et al.[29]

Aveyard, et al.[4] also studied the compression of PS latex monolayer using a Langmuir trough. This trough had two movable barriers to compress or expand the monolayer while the surface pressure (π)-surface area (A) isotherm (viz. surface isotherm) was being measured. The surface pressure is defined as the decrease of interfacial tension by the presence of particles (or the presence of amphiphilic molecules, conventionally). As shown in Figure 7, they identified the three features of the isotherm during the compression: (1) a dilute state, region A; (2) steep rising of the surface pressure due to particle repulsion, region B; (3) collapsed surface pressure (π_{col}), region C. Upon reaching the collapsed surface pressure, further compression made the particle monolayers first slightly deform the hexagonal packing, then buckle, and finally collapse into the bulk phase (i.e. particle coated fluid lumps of top fluid phase sinks into the bottom fluid phase, or vice versa)[4]. Particle desorption from the interface was not observed.

This buckling of monolayer is an indication of monolayer elasticity. This leads us to the discussion in Section 2.2.2.
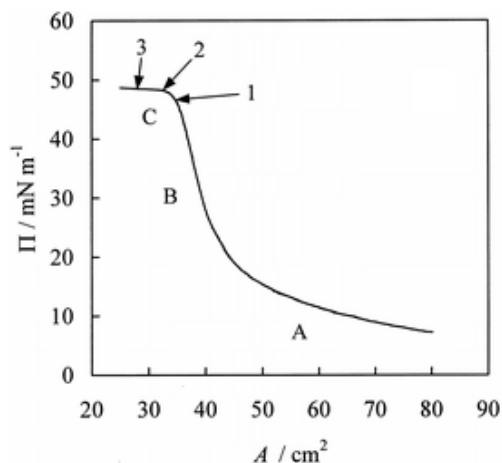
Figure 7. Surface isotherm of the particle monolayer formed by 2.6 μm diameter PS particles at octane/water interface.

Arrows 1, 2 and 3 correspond to the microstructure of monolayer being a planar monolayer with slightly deformed hexagonal packing, a planar monolayer with domain boundary, and a buckled monolayer, respectively. Reprinted with permission from (Ref. 4). Copyright (2000) American Chemical Society

2.2.2   Elasticity of monolayers: jamming and buckling

Elasticity is the physical property of a material when it deforms under stress, but returns to its original shape when the stress is removed. Adsorbed particles are confined at the interface due to the irreversible adsorption. Upon compression, particle monolayers become packed and jammed. Further compression makes particle monolayers buckle generally with a finite wavelength. It is an elastic property of monolayers because this buckling is a reversible process as long as there is no further compression that forces the folded particle layers together with the embedded fluid to enter into the other fluid phase. In the last section (Section 2.2.1), we only discussed the monolayer behaviors for monodisperse, spherical particles. In this section, we will extend the discussion to "non-ideal" particles, including flocculated silver nanoparticles and

15

fumed silica. However, we restrict the discussion to external compression of the interfacial area and exclude interfacial-tension-driven compression.

Schwartz, et al.[30] studied particle layers of flocculated silver nanoparticles at water/dichloromethane interface in a Langmuir trough. Their particles were considered as "soft" due to the flocculated structure. They obtained an isotherm similar to that of monodisperse particles (see Figure 7). In the region C of isotherm, particle layers buckled but could be flattened again upon expansion of monolayers. Combining with their other work and a literature survey, they concluded that the three-part isotherm (region A, B and C) was a generic behavior for particle layers. The particles could be nanoparticles, flocculated particles, or microsized spheres, and could also be a metal, an oxide or polymer[30].

Horozov, et al[31] studied monolayers of fumed silica particles at octane/water interface in a Langmuir trough, while varying particle hydrophobicity. They observed the buckling of monolayer at the region of steep rising in surface pressure (i.e. region B in Figure 7, instead of region C like others' observation). They attributed this unusual buckling behavior to the ability of fumed silica particles to form network structures[31].

A Langmuir trough is not the only way to study compression/expansion of particle monolayers. Fuller and co-workers[32, 33] used the sessile drop method to study the shape and buckling transitions of PS latex particle-covered water drops surrounded by decane. Using a syringe to withdraw the drop phase fluid, they were able to reduce/increase the interfacial area and thus compress/expand the particle-laden interface. The drop shapes were dictated by Young-Laplace equation before the monolayer was packed with particles. As shown in Figure 8, they observed the buckling of monolayers and the deflation of the drop.
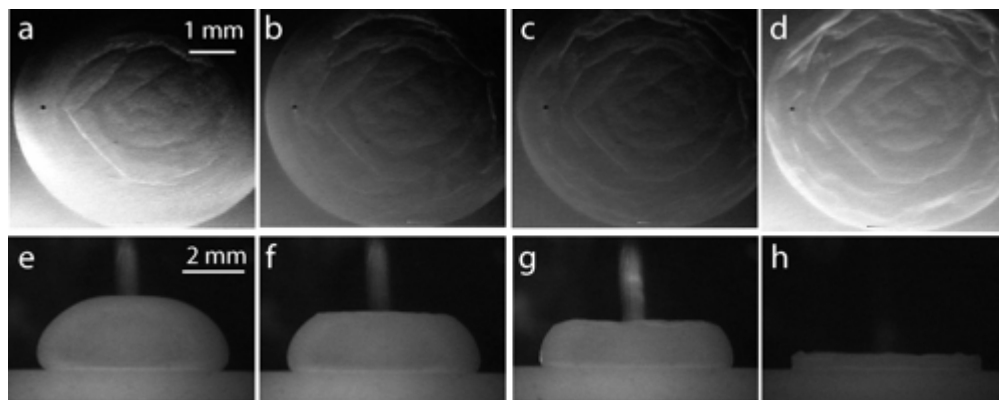
Figure 8. Shrinking drop experiments by Fuller and co-workers.

Topview (a-d) and side view (e-h). Reprinted with permission from (Ref. 32). Copyright (2005) American Chemical Society

For the theoretical model, Vella, et al.[34] developed a mechanical model for particle rafts (i.e. packed particle aggreates) that predicts the wavelength of buckling based on the relationship between Young's modulus (*E*) for particle rafts and the Beam equation which traditionally describes the buckling instability of a solid sheet. Although the model assumes a contact angle of 90° and perfectly spherical, hard spheres in close-packed hexagonal arrangement, they were able to obtain qualitative agreement between the predictions of model and a series of particle compression experiments in a Langmuir trough with different polydisperse particles[34].

To this point, we should note that most research focused on the buckling behaviors. Since the conventional compression process is externally-imposed, whether or not particle layers is jammed or packed is a spatulation based on the transition of isotherm, and also based on the microscope observation where particle edges are often ambiguous. In physics, jamming means the phase transition from a fluid state to an "apparent" solid state. Therefore, it is difficult to identify the "apparent solid state" on a externally-imposed compression experiment. In other words, the jammed state is past at the onset of the buckled state of particle monolayers. In

chapter 4, we discuss the development of an alternative way to study interfacial particle jamming.

2.3   MORPHOLOGIES OF PARTICLE-FREE POLYMER BLENDS AND DEVELOPMENT OF MORPHOLOGY

Blending two polymers together to create a material with desirable properties is an economic alternative to synthesizing new polymers. The morphology of a polymer blend often determines its properties, and thus determines the suitable end-uses of the blend. We discuss two possible morphologies for particle-free blends generated under a simple mixing flow: (1) droplet-matrix morphology; (2) bicontinuous morphology (viz. co-continuous morphology). We exclude the matrix-fiber and lamellar structures which are less related to our work and only appear under a complex flow such as melt mixing in polymer processing. The morphology type of a blend is primarily determined by the volume fractions and viscosities of each component. The strength and type of flows during mixing are relevant to the domain size of morphology, and to the morphology type if the blends are quenched (i.e. decreased in temperature) into a flow-induced morphology.

If the volume fraction of one of the two components is sufficiently small ($\phi_{drop} \ll 1$), a morphology with discrete drops in a continuous matrix (i.e. droplet-matrix morphology) is expected. As the volume fraction of the drop phase increases, eventually the blend undergoes a phase inversion process where the original drop phase becomes the continuous phase, and vice versa. Near the phase inversion point, the blend may or may not adopt a bicontinuous morphology (discussed in Section 6.3.1). In a simple model proposed by Paul and Barlow[35, 36],

18

two factors determine the phase inversion point: the component volume fractions and the viscosity ratio. In the equation form, it says $\frac{\phi_A}{\phi_B} \cdot \frac{\eta_B}{\eta_A} \cong 1$, where ϕ_A and ϕ_B are the volume fractions of component A and B at the phase inversion point, respectively. η_A and η_B are the viscosities for component A and B.

When viscosity is not matched (i.e. $\frac{\eta_B}{\eta_A} \neq 1$), the low-viscosity component tends to become the matrix phase. The high-viscosity component tends to become the drop phase (see Figure 9).
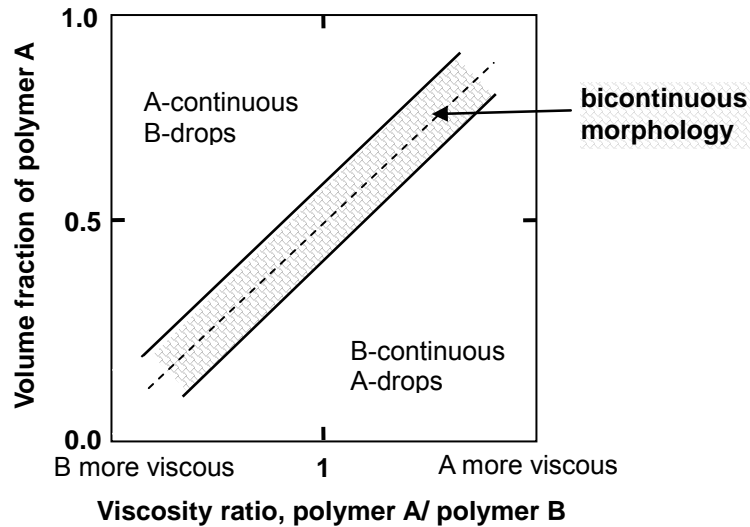
Figure 9. Relation between the volume fraction and the viscosity ratio for polymer blends. (adapted from Ref. 36). Dashed line is for a blend that does not show a bicontinuous morphology near phase inversion point. Copyright (2003) Taylor & Francis

2.3.1 Morphology development of a droplet-matrix blend under flow conditions

Under flow conditions, if interfaces exist in the system of interest, we need to consider three effects, namely viscous effect, interfacial effect and inertial effect. Because polymers have relatively high viscosities than other fluids, they offer a means to study systems where inertia is negligible. For a droplet-matrix blend, as affected by flow or change of flow conditions, the drops can undergo four possible behaviors: deformation and retraction, breakup and coalescence. Drop deformation and drop retraction are the opposite behavior of each other, and so are drop breakup and drop coalescence. Among these, drop retraction occurs when the flow is ceased (or reduced), and it is governed by interfacial tension and less related to effects of flow. We will discuss the drop retraction in blends which result in strain recovery of blends in Section 2.5.

In the following, we first focus on the single-drop behaviors under flow conditions, i.e. drop deformation and drop breakup. Then, we discuss two-drop behavior under flow (i.e. drop coalescence). Finally, we discuss the balance between drop coalescence and breakup in a blend under flow conditions.

2.3.1.1 Single drop deformation and breakup

When a drop is subjected to simple shear flow, it deforms, and orients with the flow to reduce drag force, and possibly breaks up. There is a competition between viscous forces that tend to deform the drop, and interfacial forces that try to minimize the interfacial area and thus resist the deformation. The relevant dimensionless quantity is the capillary number, Ca, given by:
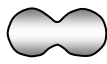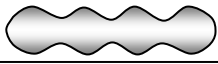
$$Ca = \frac{\text{viscous stress}}{\text{interfacial stress}} = \frac{R\eta_{matrix}\dot{\gamma}}{\alpha_{AB}} = \frac{[m][Pa.s][s^{-1}]}{[N/m]} = \text{dimensionless}$$

where R is drop radius, $\dot{\gamma}$ is the shear rate, α_{AB} is the interfacial tension, and η_{matrix} is the viscosity of the matrix phase.

Under steady-shear flow conditions, the steady-state deformed drop shape depends on both the viscosity ratio ($p = \dfrac{\eta_{drop}}{\eta_{matrix}}$) and capillary number ($Ca$). Different possibilities of drop shape are as follows, as well as summarized in Table 2.

(1) at low p and low Ca: drops tend to form ellipsoids.

(2) at low p and high Ca: drops tend to form sigmoidal shapes.

(3) at $p \approx 1$ and any Ca: drops tend to form ellipsoids.

(4) at high p and low Ca: drops tend to form ellipsoids.

(5) at high p and high Ca: drop shapes are slightly deformed spheres which rotate in flow.

Table 2. Summary of possible deformed drop shape and possible drop breakup modes.

	Steady-state deformed drop shape		Drop breakup modes @ $Ca > Ca_{crit.}$	
Viscous matrix	Low p, low Ca			
	Low p, high Ca		$p \ll 1$	
Viscosity match	$p \approx 1$, high Ca		$p = 1$	
Viscous drops	high p, low Ca		$1 < p < 3.7$	
	high p, high Ca			

Under shear flow, for any given value of p less than 3.7 ($p < 3.7$), there exists a critical capillary number ($Ca_{crit.}$), which determines whether or not drop breakup can occur. When the capillary number of this flow condition is larger than the critical capillary number, i.e. $Ca > Ca_{crit.}$, the drop will break up. When $Ca < Ca_{crit.}$, the drop will attain an equilibrium deformed shape,

oriented at some angle to the flow field. When $p > 3.7$, a drop under shear flow cannot deform its shape, but it exhibits rotational motion in the shear field[37].

As summarized in Table 2, when the drop does break up at $Ca > Ca_{crit.}$, there are different modes of breakup: (1) for Ca is slightly larger than $Ca_{crit.}$ and $p \approx 1$, the extended drop thins at the waist and pinches into two large drops, with or without satellite drops between the large drops; (2) for Ca is slightly larger than $Ca_{crit.}$ and $p \ll 1$, the drop forms a pointed sigmoidal shape and small droplets are released from the end (i.e. tip streaming); (3) for $p < 3.7$ and $Ca \gg Ca_{crit.}$, the drop stretches into a long fiber and breaks up by capillary instability. When $p > 3.7$, drops can only break under extensional flow, but not under shear flow[37] because they tend not to deform.

2.3.1.2 Coalescence of two drops

When a droplet-matrix blend is sheared, a drop may collide with another drop. As two drops collide, the interfaces deform and there is only a film of the matrix fluid left between the two drops. For the droplets to coalesce, the fluid film must drain to a critical value where van der Waals forces between the droplets become significant to make the film rupture. The time duration needed for the fluid film to drain and rupture is called the drainage time. Also, because of the flow, there is only a limited time duration that the drops are in contact with each other, which is called the collision time. If the collision time is larger than the drainage time, the two drops coalesce. If the collision time is not long enough, the two drops separate again in the flow.

In general, when the drop phase viscosity is low ($p < 1$), the drop deforms easily. The interface is said to be fully mobile, and drop coalescence is more likely to occur for a given collision time. For a system with a high p, the interface is said to be immobile and does not deform. Coalescence is less likely for a given collision time. Particle adsorption is expected to

make the interface more rigid, especially when interfacial jamming occurs. They may also affect the drainage and rupture processes of the fluid film[38].

2.3.1.3 Balance between coalescence and breakup in a blend under flow

At steady state, the drop size of a droplet-matrix blend is determined by a balance between drop breakup and drop coalescence. At any given moment, if the drop size (radius of R) is such that $Ca > Ca_{crit.}$, those drops will break up. If the drop size is such that $Ca < Ca_{crit.}$, drop breakup does not occur. The drop in its deformed shape may collide with other deformed drops in the flow. The collision may produce a larger drop with $Ca > Ca_{crit.}$ that needs to undergo drop breakup. This balance between the coalescence and breakup continues until a steady state is reached and the mean drop size is constant. At steady state, for each drop, $Ca_{ss} \cong Ca_{crit.}$. However, the steady state may not be obtained if the kinetics of these processes (i.e. encounter, collision, coalescence and breakup) is slow compared to the length of the shear history.

2.3.2 Phase coarsening in a bicontinuous morphology under quiescent condition

2.3.2.1 Methods of generating a bicontinuous morphology

Before we discuss the phase coarsening of a bicontinuous morphology, we first introduce the different methods of generating a bicontinuous morphology in a binary polymer blend composed of two homopolymers (i.e. we exclude block copolymers). The methods can be categorized into two mechanisms: (1) by spinodal decomposition; (2) by complex flow in melt-blending process.

The fundamental difference between the two mechanisms is that the spinodal decomposition phase separation process begins with a "single phase" mixture, but during the melt-blending of an *immiscible* blend, a fully-mixed phase is never obtained. The bicontinuous

structure generated by melt-blending is a result of complex flow and its consequence on the components.

Spinodal decomposition is a mechanism by which a solution of two components can separate into two phases with distinctly different chemical composition and physical properties. The phase separation by spinodal decomposition is triggered by a sudden change of thermodynamic conditions such that an original stable state is no more thermodynamically stable. Therefore, the amplitude of concentration fluctuation in the spatial domain of samples keeps growing as driven by a decrease in free energy. Because the initial concentration fluctuation is in the form of sinusoidal function with a finite wavelength, the morphology resulted is generally a bicontinuous morphology which can retain equal length scale of each of the separated phases, and equal volume simultaneously. To the best of our knowledge, there are three methods to induce a spinodal decomposition phase separation process: (1) temperature quench; (2) solvent quench; (3) flow quench (i.e. the demixing that follows a flow-induced mixing).

The third method, however, should be considered as a special case of spinodal decomposition because the trigger (i.e. the stop of flow) is not a thermodynamic parameter but a dynamic parameter. As will be shown in chapter 5, we believe that the flow-induced mixing and the demixing upon flow quench have triggered a spinodal decomposition that results in the bicontinuous morphology of PI/PIB blends.

In the following, we briefly introduce the different quench methods.

As shown in Figure 10, in a temperature-composition phase diagram of a binary polymer blend, there is a binodal curve that separates the one-phase region and the two-phase region. The binodal curve can either curve up for a system of lower critical solution temperature (LCST system) or curve down for a system of upper critical solution temperature (UCST system). The

concave or convex, shape and location is a system specific property of blends. When the temperature of the system is changed to induce spinodal decomposition, the single-phase sample is forced to enter the two-phase region of the phase diagram. This is called a temperature-quench step.
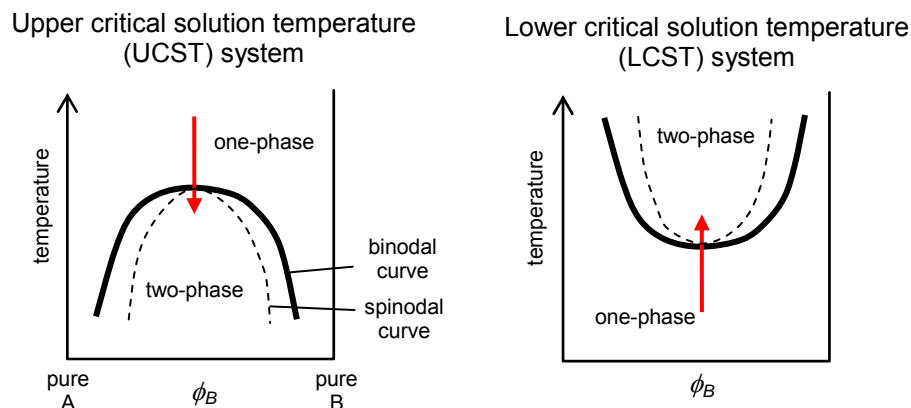
Figure 10. Schematic representation of phase diagrams for UCST and LCST polymer blend systems. The solid arrow is the temperature-quench line at the critical composition which results in bicontinuous morphology.

As showed in Figure 11, for a three-component system containing polymer A, polymer B and a common solvent which has favorable interaction with both A and B, as the solvent evaporates from the system and thus the system concentrates, the two polymer components "feel" the unfavorable interaction between the two different component polymer chains. This solvent evaporation process to induce spinodal decomposition is called a solvent-quench step.
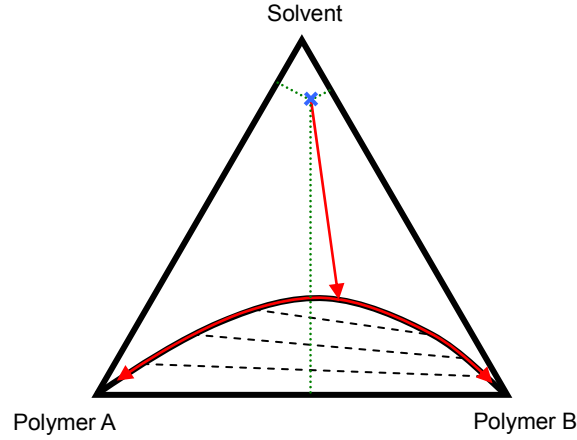
Figure 11. Ternary phase diagram for polymer A, B and solvent.

The cross represents the initial mixture composition, as indicated by the relative length of three dotted lines. The

arrowed line is the solvent evaporation line. After the solvent-quench line reaches the two phase envelope, the

mixture phase separates into A-rich phase and B-rich phase according to the tie line (dashed line).

The concept of flow-induced mixing is introduced below. In a shear flow, droplets in the

blend can be broken down to sizes comparable to the dimensions of the polymer molecules

themselves, thereby inducing molecular-scale mixing[39]. The size of droplets (radius, R) under

flow is a function of the interfacial tension, shear rate and viscosity of matrix (i.e. $R \sim \dfrac{\alpha_{AB}}{\eta_{matrix}\dot{\gamma}}$).

The characteristic length scale for macromolecules is radius of gyration (R_G) of the polymer

chain. Therefore, it is assumed that miscibility between two polymeric fluids is achieved when

$R_G \approx R \sim \dfrac{\alpha_{AB}}{\eta_{matrix}\dot{\gamma}}$.[40, 41] This is most readily achieved if the interfacial tension between the two

polymer phases is low[39]. After the flow stops ($\dot{\gamma}=0$), the concentration fluctuation can resume

via the spinodal decomposition process.

Spinodal decomposition has been divided into the "early", "intermediate" and "late"

stages based on different characteristics[42]. At the early stage, the sinusoidal concentration

26

fluctuation develops and grows in amplitude, while the wavelength of fluctuation in spatial domains is fixed. At the intermediate stage, both the wavelength and the amplitude of the fluctuation increase. At the late stage, the amplitude of concentration fluctuation reaches a maximum, and only the wavelength can change (i.e. domain size can increase)[42].

After the late stage of the spinodal decomposition process, the interfacial-tension-driven domain coarsening follows (described in Section 2.3.2.2).

The second mechanism of generating a bicontinuous morphology is by complex flow in melt-blending. We do not discuss it here because melt-blending in polymer processing is a complicated process and its processing equipment is not used in our work. However, a relevant example of "hand-blended" immiscible PI/PDMS blend will be discussed in chapter 6. We continue the discussion of domain coarsening of a bicontinuous polymer blend in Section 2.3.2.2.

2.3.2.2 Domain coarsening rate of a bicontinuous morphology under quiescent condition

The driving force of domain coarsening (viz. phase coarsening) in a bicontinuous morphology is interfacial tension, or equivalently the decrease in interfacial energy due to decrease of interfacial area. The larger the domain, the smaller is the interfacial area per unit volume.

The domain coarsening process is divided into three stages[42] based on different scaling laws for the domain growth rate: (1) Ostwald ripening ($d \propto t^{1/3}$), which is actually the late stage of spinodal decomposition; (2) interfacial tension controlled coarsening ($d \propto t$); (3) gravitational or divergent coalescence that lead to the formation of large-sized separate domains[42].

Chung, et al.[43] studied the temperature-quenched, spinodal-decomposition-generated bicontinuous thin films of the dPMMA/SAN polymer blend, as well as the effect of particles. In their plot of d verse $t^{1/3}$, they obtained a linear correlation for a particle-free film between the

first and tenth hour of the annealing step. The domain size (d) information was obtained from atomic force microscopy (AFM) scanning of the film surface in which one of the components has been removed by a selected solvent.

On the other side, Veenstra, et al.[44] demonstrated a linear relationship of d verse t for the coarsening of a variety of bicontinuous melt-blended systems (including LDPE/PMMA, LDPE/PS and PP/LDPE and copolymer-compatibilized blends) under quiescent annealing. The coarsening was shown to be dependent on the interfacial tension and the zero-shear viscosity of the blend materials (i.e. $\frac{dR}{dt} \propto \frac{\alpha_{AB}}{\eta_e}$, where η_e is the effective viscosity of blends based on weight ratio). The domain size ($2R$) information was obtained from scanning electron microscopy (SEM) image analysis of fractured surface of samples in which one of the components has been removed by selected solvents.

Yuan and Favis[45] studied the coarsening rate under quiescent annealing for PS/HDPE and PMMA/HDPE blends. They also found a linear relationship ($R \sim kt$). Using a conceptual geometry model based on connected thin and thick rods, they proposed that the driving force for the coarsening process is a capillary pressure effect. The differences in capillary pressure throughout the bicontinuous structure result in the continuous merging of thin parts toward the thick ones. An analysis for capillary instabilities[46] was adopted in the model. The coarsening rate was found to be controlled by interfacial tension, zero shear viscosity of the surrounding medium, and the Tomotika function[46] which depends on wavelength of instability and the viscosity ratio of the two phases. A good correlation between the model prediction and experimental results were found.

In short, the domain coarsening is mainly controlled by the interfacial tension, resulting in the decrease in interfacial area and energy. The coarsening process is achieved by the fluid

retraction of thin region (rod-like region or called necks). The fluid of thin region which retracts continuously feeds to thick region as driven by the capillary pressure difference ($\Delta P \propto \dfrac{2\alpha_{AB}}{R}$) between thin and thick regions. The coarsening process may span over a long timescales while maintaining the dual-continuity of the two phases.

2.4   INTRODUCTION TO BIJELS

Bicontinuous interfacially jammed emulsion gels (i.e bijels)[47] are relatively-new composite materials that have received attention both in simulations[12, 48] and experiments[49] in recent years. This composite material is composed of an immiscible fluid pair (fluid A and fluid B) and interfacially-active particles.   The fluid pair can be either small-molecule pair[49], or macromolecular pair[43].   Bijels have a unique structure consisting of interpenetrating, bicontinuous fluid domains with the position of the domain boundary (i.e. interface) pinned by 2D particle jamming. The whole structure is stable and behaves like soft solid, even though both of the continuous phases remain liquids.
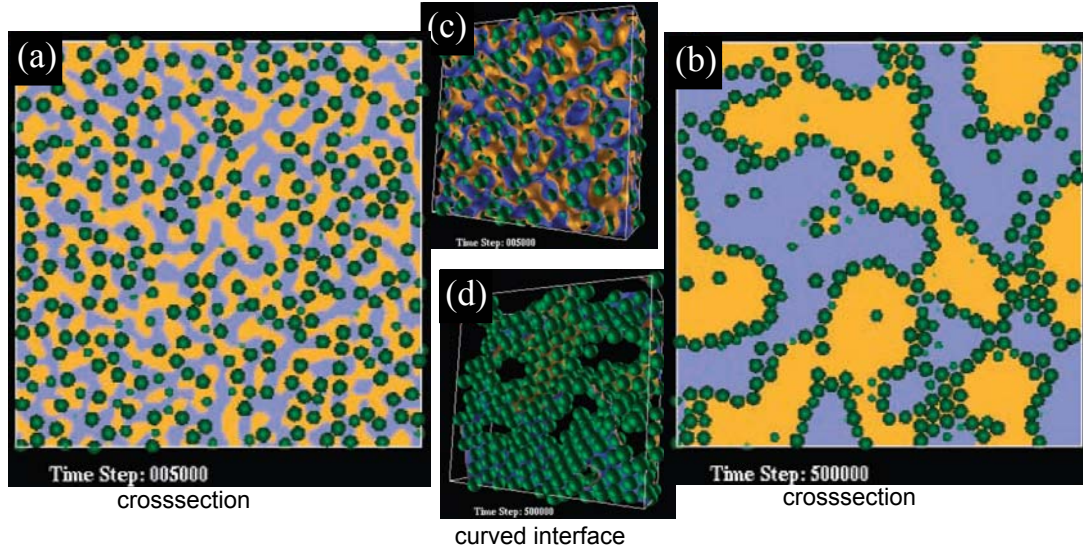
Figure 12. Time evolution simulation of the bijel formation by Stratford et al.[12]

(a) and (c) Time step=5000, showing the early stage of spinodal decomposition between phase A (yellow in a color print or light gray in a black-and-white print), phase B (blue or dark gray) and random distribution of particles (green or dark sphere). (b) and (d) Time step=500000, showing that most particles have been sequestered by interface and particles are densely packing at the interface. Reprinted with permission from (Ref. 12). Copyright (2005) The American Association for the Advancement of Science.

In Stratford original paper that coined the term "bijel", they suggested forming a bijel structure by first forming a particle suspension in a single-phase two-species fluid mixture at the temperature where the fluid pair is miscible, and then to quench the temperature to induce the spinodal decomposition (see Figure 12). During the phase separation process, the interfacial area keeps decreasing due to domain coarsening, which is driven by interfacial tension (described in Section 2.3.2). As the newly-formed interface sweeps across the materials, it sequesters any particle that it encounters. Since particle adsorption to the interface is nearly irreversible, the particle concentration at the interface increases during domain coarsening. Once the interface is densely packed and jammed by the particles, the phase evolution is stopped and the structure becomes "frozen".

Bijels have potential applications that require a large amount of fluid-fluid interfaces within a small volume. Researchers have suggested that bijels can be applied as a microreaction medium[12] or microfluidic channels[49], although these applications are yet to materialize. We will show an example of bijel-structured polymer blends (i.e. polymer bijels) in chapter 5.

2.5   RHEOLOGICAL MEASUREMENTS OF POLYMER BLENDS

Rheology, which is the study of material properties during flow and deformation, is often used to gain information about the viscoelastic properties of materials. By applying simple flow fields, the response of materials can provide clues on the microstructures and the properties of materials under flow. A mixture of two immiscible Newtonian fluids such as the polymer blends under study in chapter 5 and 6, can display viscoelastic behaviors because the fluid-fluid interface may store mechanical energy via the deformation of interface. The viscoelasticity of a material is a property to describe that the material is relatively elastic at short times (or high frequency) and relatively viscous at long times (or low frequency). Therefore, a viscoelastic material can display both the solid-like and the liquid-like behaviors depending on the time scale of the force applied. Two rheological techniques to probe the morphology will be used in this work. They are the strain recovery measurement and the dynamic oscillatory (viz. frequency sweep), as will be introduced in the following.

2.5.1 Strain recovery of blends

In Section 2.3.1, we discussed the drop behaviors including deformation, breakup and coalescence in a droplet-matrix blend under the influence of flow. We now discuss the drop retraction in a blend and the corresponding effect on the blend properties. After the cessation of flow, all the deformed drops are in the process of retracting back to a spherical shape as driven by interfacial tension. This coherent retraction of drops results in a deformation of the matrix, and thus affects the whole material. This post-stress deformation in the opposite direction of original stress and deformation is called the elastic recovery of the blend, and also called a "recoil" behavior of blend. Because the components of the blend are both Newtonian fluids, which show no recoil behavior, the elastic recovery (viz. strain recovery) can be fully attributed to the action of the interfaces.

The kinetics of strain recovery for a blend of monodisperse drops is given by Vinckier, et al.[50], as shown below:

$$\gamma_{recov.}(t) = \gamma_{\infty}\left[1 - \exp\left(-t/\tau_2\right)\right] \tag{2.1}$$

where τ_2 is the characteristic retardation time of drop retraction after the cessation of flow, and γ_{∞} is the ultimate strain recovery. Based on dimensional analysis, the retardation time (τ_2) and ultimate strain recovery (γ_{∞}) can be related as:

$$\tau_2 \propto \frac{R\eta_{matrix}}{\alpha_{AB}} \tag{2.2}$$

$$\gamma_{\infty} \propto \frac{R\sigma}{\alpha_{AB}} \tag{2.3}$$

where R is the drop radius, η_{matrix} is viscosity of matrix, α_{AB} is the interfacial tension between the two polymer components and σ is the shear stress applied.

Therefore, both τ_2 and γ_∞ can be correlated to the drop size. Furthermore, the strain recovery curves provide vital information on the kinetics of drop retraction process.

A typical semi-log plot of strain recovery[51] is shown in Figure 13. The solid line is the strain recovery curve for a blend with smaller droplets, and the dashed line is for a blend with larger droplets under a fixed stress. This curve sometimes would be expressed in a log-log plot (not shown).
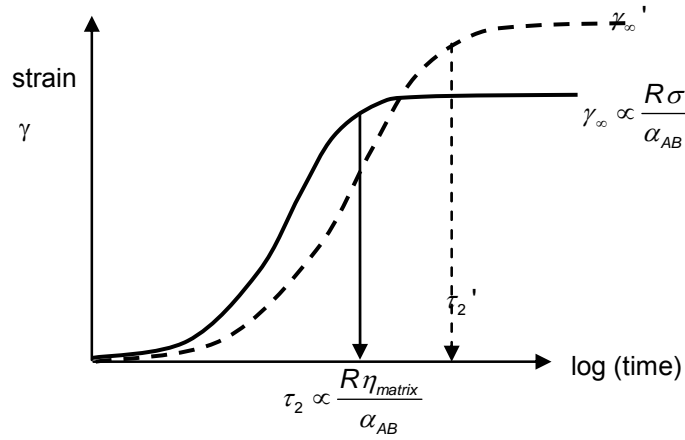
Figure 13. Typical plot of a strain recovery curve for particle-free blends with a droplet-matrix morphology.

2.5.2 Dynamic oscillatory behavior of blends

Small-amplitude oscillatory shear is often used to probe the morphology of a blend or other structured fluids without significantly affecting the microstructure. A blend sample is subjected to a sinusoidal strain (γ) at various frequencies (ω) to generate a frequency spectrum which shows the viscoelastic properties of the sample. The sinusoidal strain is expressed as:

$$\gamma = \gamma_0 \sin(\omega t) \tag{2.4}$$

where γ_0 is the amplitude of the sinusoidal strain.

The stress response of a viscoelastic sample is delayed, and thus it is out of phase by a phase angle δ to the strain. The stress response is expressed as:

$$\sigma = \sigma_0 \sin(\omega t + \delta) = (\sigma_0 \cos\delta)\sin(\omega t) + (\sigma_0 \sin\delta)\cos(\omega t)$$
$$= \gamma_0 G'\sin(\omega t) + \gamma_0 G''\cos(\omega t)$$

(2.5)

where G' and G'' are the storage and loss moduli, respectively. G' is in-phase with the strain and thus is indicative of solid-like or elastic behavior; G'' is out-of-phase with the strain and thus indicative of liquid-like or viscous behavior.

For blends, the variation of G' and G'' with the oscillatory frequency ω is directly related to drop behavior and thus the morphology. At high frequency of oscillation, the drops deform with the applied flow with no significant relaxation because relaxation (i.e. retraction) takes time longer than the time interval of frequency. At lower frequencies, the drops deform during the applied flow and relax back as driven by interfacial tension. As shown in Figure 14a, this relaxation of drops causes the appearance of a characteristic shoulder in the $\log(G')$ versus $\log(\omega)$ plot. The presence of the shoulder is an indication of interface relaxation, provided that the relaxation time of the component fluids is much smaller than the interface relaxation, which is indeed the case for Newtonian components.

The complex viscosity (η^*), which is also a function of frequency for viscoelastic materials, is defined as:

$$\eta^* \equiv \frac{G^*(\omega)}{i\omega}$$

(2.6)

where the complex modulus is defined as $G^*(\omega) \equiv G' + iG''$ with its magnitude being $\left|G^*(\omega)\right| = \sqrt{G'^2 + G''^2}$.

The magnitude of the terminal complex viscosity, given by:

$$\left|\eta_0^*\right| \equiv \lim_{\omega \to 0} \frac{\left|G^*(\omega)\right|}{\omega} \tag{2.7}$$

is used as an indication of the zero-shear viscosity of a material.

Researches on model immiscible blends have shown a strong correlation between drop relaxation and the frequency position of shoulders for both G' and $\left|\eta^*\right|$.[52-55] Both dimensional analysis and detailed theory[54] suggest that the characteristic frequency scales as $\frac{\alpha_{AB}}{R\eta_{matrix}}$, where R is the mean drop size, α_{AB} is interfacial tension and η_{matrix} is the viscosity of matrix phase. As shown in Figure 14a and b, the larger the drop size (dashed line in the figure), the more time it takes to relax, and thus the shoulder appear at lower frequency. The relation between the drop size and the relaxation time makes small-amplitude oscillatory a very useful microstructure probe.
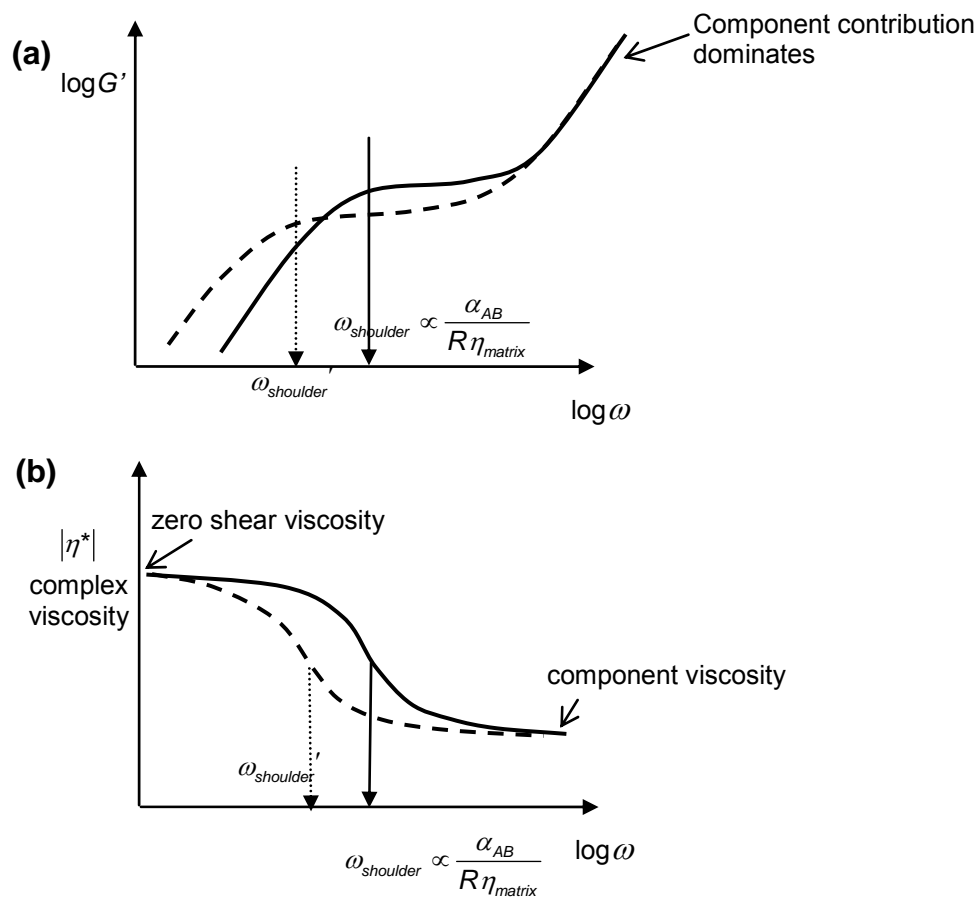
Figure 14. Typical plots[51] of storage modulus and complex viscosity curves in frequency sweep measurements for

particle-free blends with a droplet-matrix morphology.

(a) storage modulus curve (b) complex viscosity. The dashed lines are for a blend with a larger mean drop size.

3.0 FILM CLIMBING OF PARTICLE-LADEN INTERFACES

Recent experiments have shown that coalescence of an oil/water/nanoparticle Pickering emulsion contained in a vial induces a nanoparticle-film to climb up the walls of the vial. Here we show that this phenomenon is highly general and can be induced by a variety of particle types, particle sizes ranging from a few nm to a few micron and different emulsion types. Many of the features of film growth described previously with nm-sized particles are found to remain true even with the far larger particles studied here. Binks et al. [B.P. Binks, J.H. Clint, P.D.I. Fletcher, T.J.G. Lees, P. Taylor, Growth of gold nanoparticle films driven by the coalescence of particle-stabilized emulsion drops, Langmuir 22 (2006) 4100-4103] have postulated that the particle films that climb up the walls of a vial are actually comprised of one oil layer and one water layer, with particles adsorbed at the interface between them. We confirm this "sandwich" structure experimentally and also show that such interfacially adsorbed particles can easily exert the very modest surface pressure necessary to sustain the weight of the film. Our experiments highlight the importance of prewetting the walls of the vials; films do not climb unless the walls are prewetted. Finally, while some climbing films are tightly packed particle monolayers, tight packing is not essential; even sparsely populated monolayers can display film climbing.

3.1   MATERIALS

Light mineral oil (henceforth referred to as "oil") was obtained from Fisher and was used as the non-polar phase in all the experiments in this paper. The polar phase was either water (Milli-Q) or ethylene glycol, obtained from Fisher. Octadecyltrichloromethylsilane (OTS), of 97% purity was purchased from Gelest Inc. All chemicals were used as received. Milli-Q water was used in all experiments.

A majority of this study was conducted on iron oxyhydroxide (FeOOH) particles (Figure 15a) donated by Elementis Pigments Inc. The particles are polydisperse, elongated with an average length of about 0.6 μm, have a density of 4.03 g/cm^3, and appear yellow in color. Limited experiments were conducted with three other particle types: carbonyl iron (Fe, ISP Technology), iron oxide (Fe_2O_3, BASF), and spherical silica (Tokuyama Inc.) to show the generality of film climbing with respective to particle types. The carbonyl iron particles (Figure 15b), also known as iron pentacarbonyl, are spherical with 2 to 4 μm diameter, and appear black. The iron oxide particles, which are red in color, appear in SEM images (Figure 15c) to be micron-scale aggregates of elongated nanoparticles. Some of these aggregates may persist even after ultrasonication during our sample preparation. The spherical silicas are monodisperse, 2.7 μm in diameter, and were rendered hydrophobic by treating with dichlorodimethylsilane (DCDMS). Details of the procedure are provided elsewhere[56, 57], but briefly speaking, dried silica particles were reacted with DCDMS in anhydrous cyclohexane, centrifuged, washed with cyclohexane and chloroform, and then dried in air at 110°C.

No surfactants were used in any of this research; all of these particles were active at the oil/water interface without added surfactants.
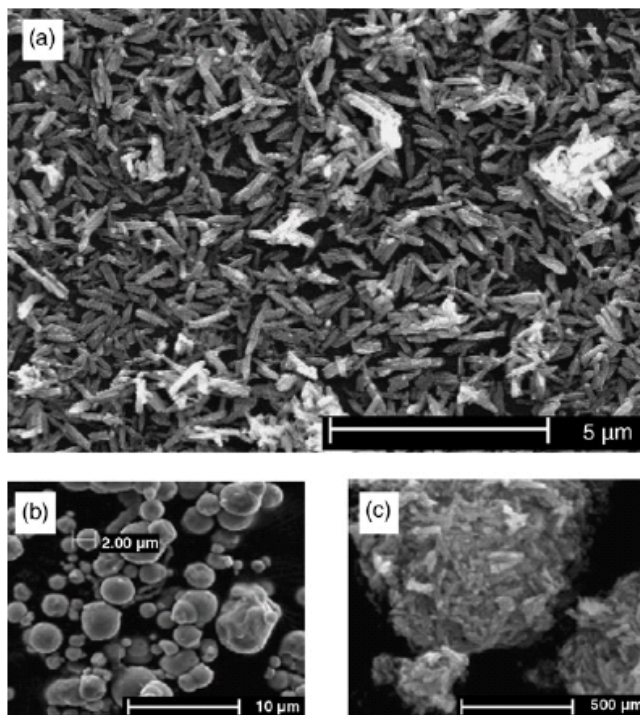
Figure 15. SEM images of three types of particles used in flim-climbing research.

Iron oxyhydroxide FeOOH, (b) a carbonyl iron (Fe), and (c) iron oxide (Fe_2O_3).

Most of the imaging was performed with a Canon Digital Rebel SLR camera equipped with a 55 mm focal length lens and a 12 mm extension tube. Higher magnification images of Section 3.2.2 were collected with Sony CCD video camera equipped with a video-zoom lens (Navitar 6000).

3.2   RESULTS AND DISCUSSION

3.2.1   The film climbing experiments, mechanism, and its generality

We will first note some qualitative features regarding film growth in the case of FeOOH particles, and specifically point out similarities with previous research on the much smaller gold

nanoparticles[58, 59]. The basic film growth procedure, denoted the "shake-and-stand" procedure, consisted of shaking together all the ingredients in a vial for a few seconds, and then allowing the vial to stand upright under quiescent conditions. A typical recipe was as follows: an aqueous suspension of 0.07 wt% particles was prepared and ultra-sonicated for 5 min. Two milliliter of this suspension, and 2 ml of oil was added to an 8 ml glass vial; this corresponds to a particle loading of 1.4 mg for the 4 ml of total liquid. The vial was shaken by hand for a few seconds. This shaking gave the particles an opportunity to adsorb at the oil/water interface, and particle-covered drops were evident after shaking (Figure 16a); the fact that the drops rise to the top indicates that the drops are oil and the emulsion is of the oil-in-water type. At this particle loading, these particle-covered oil drops were not stable and started coalescing, and a film of particles was found to climb upwards along the walls of the vial (Figure 16b). Henceforth in this chapter, we will use the term "film climbing" rather than "film growth" or "film formation" used previously. The particle film continued climbing (Figure 16c-d), generally reaching all the way up to the top of the vial (Figure 16e).

(a) 0 s   (b) 5 s   (c) 10 s   (d) 15 s   (e) 60 s
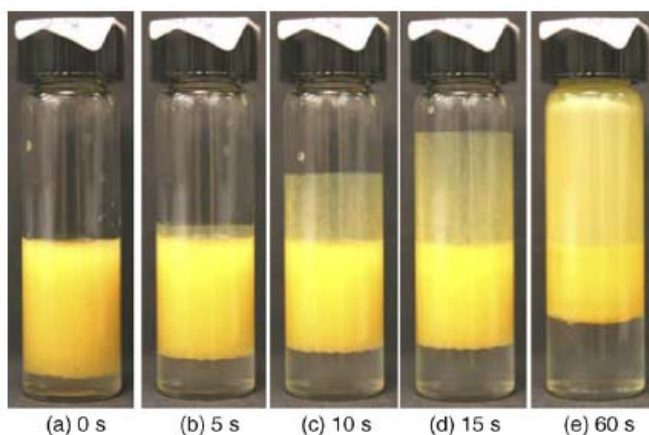
Figure 16. Sequence of file climbing for FeOOH particles.

The time after stopping the shaking of the vial is noted below each image. The change in color intensity from (d) to (e) is attributable to an increase in interfacial concentration of particles in the file with increasing coalescence.

40

As noted by Binks et al.[59] film climbing is directly associated with coalescence of the drops; once coalescence stops, film climbing stops as well. From visual observation of the top surface of the emulsion, we can describe the film growth procedure in greater detail than previously[58, 59]. In particular, unlike the nanoparticle emulsion system that Mayya and Sastry worked on[58], film climbing does not start immediately after the emulsion has "settled down after the shaking process"[58]. In the as-shaken vial, all of the oil is emulsified, and hence the top surface of the liquid is the air/water interface as shown in Figure 17a. Initial coalescence causes a lens of oil to form at the top surface of the emulsion (Figure 17b), but this initial coalescence is not accompanied by film climbing. With additional coalescence, the lens increases in extent until the entire crosssection of the vial is spanned by a continuous oil/water interface (Figure 17c). Subsequent coalescence of drops with the continuous oil/water interface induces film climbing. Indeed, the advancing front of the climbing film occasionally appears to "jump" upward due to the coalescence of an especially large drop. The mechanistic explanation suggested previously is that as coalescence deposits particles at the continuous oil/water interface, it raises the particle concentration locally. The corresponding spreading pressure (i.e. Marangoni stress) pushes the oil/water interface up the walls of the vial. Consistent with this physical picture, coalescence of drops with each other (rather than with the continuous oil/water interface) did not contribute to film climbing. In summary, while experimental observations of film climbing of the FeOOH particles are broadly in agreement with the physical picture proposed by Binks et al.[59], Figure 17 gives a more refined picture of the initial stages of film climbing, in particular stressing that film climbing does not start until a lens of oil completely covers the top surface of the vial. (Previous publications are not explicit on this point, but the schematic in Binks et al.[59] suggests that the top surface of their emulsion is the air/oil interface even at the earliest time of observation after shaking the vial.) Finally, we note that Goedel and

co-workers[60, 61] have described the phenomenon of "particle-assisted wetting" in which interfacially active particles induce the spreading of one liquid on the surface of another immiscible liquid. The film-climbing phenomenon may be regarded as a variation of particle-assisted wetting in which particles assist a liquid/liquid interface to spread on a solid substrate.
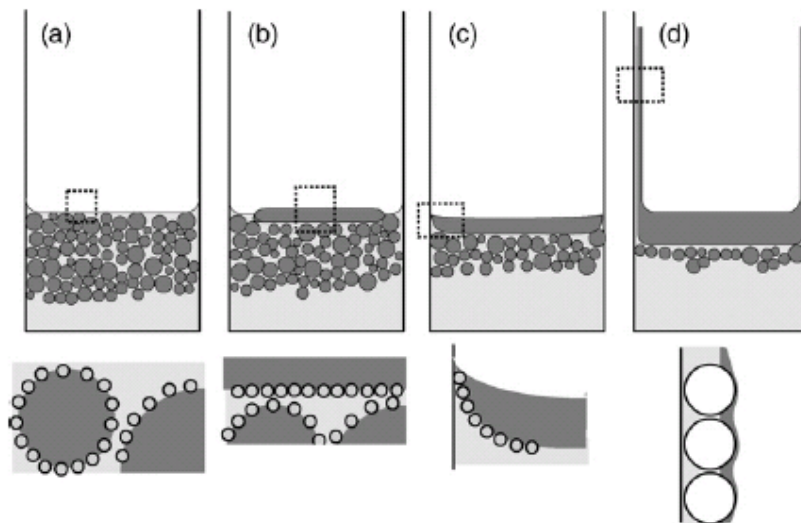
Figure 17. Schematic of film climbing process.

(a) Emulsion after shaking: particles are adsorbed at the interface, (b) drops coalesce and form an oil lens, (c) the lens grows to span the cross-section of the bottle, and (d) particle force the film to climb upwards. In (a)-(d), the region of each dotted rectangle is shown in magnified form below each figure.

The film-climbing phenomenon is robust, and occurs even if the above preparation procedure is not followed exactly. For example, while Figure 16a started with a good dispersion of particles in the aqueous phase, this was not essential. The same phenomenon could be seen if dry particles are added to a vial already containing oil and water, or if particles are first dispersed in oil and then shaken with water. Film climbing can be repeated numerous times in the same vial. However, if the vial (with a climbed film) is allowed to stand for several days, or if the vial

is left open (allowing water to evaporate), the particles adhere strongly to the walls of the vial and cannot be dislodged by shaking the vial.

All of the above observations are broadly true for several other particle types studied in our lab. Figure 18a shows a film of μm-sized carbonyl iron particles induced by coalescence of an oil-in-water emulsion; in this system, film climbing proceeded essentially identically to Figure 16. Figure 18b shows a film of iron oxide Fe_2O_3 particles formed from coalescence of an oil-in-water emulsion. A minor difference in this case is that the aqueous phase in the lower part of the vial appeared bright red even after film climbing, suggesting that most of the particles were still suspended in water. The film climbing was therefore driven by only the fraction of the particles that adsorbed at the oil/water interface. Figure 18c shows a FeOOH climbing film formed from coalescence of an oil-in-ethylene glycol emulsion—to our knowledge, the first example of film climbing in a non-aqueous system. The film climbed much more slowly in this case, typically taking a few minutes to reach the top of the vial. We believe that this is because the higher viscosity of ethylene glycol (vs. water) retards both coalescence as well as film climbing. Finally, we have also seen film climbing induced by coalescence of a water-in-oil emulsion containing 2.7 μm diameter silica particles. Since the particles were rendered hydrophobic (see Section 3.1), the initial emulsion was of the water-in-oil type as evidenced by the fact that the drops sank after the vial was shaken. Therefore the coalescing water drops were located far below the top surface (i.e. air/oil interface), and hence film growth began far below the top surface of the emulsion. This is different from all the previous cases in which the coalescing drops[58, 59] or bubbles[62], were present near the topmost air/fluid interface. These colloidal silica particles are not significantly colored, therefore the corresponding films (not shown) are more difficult to see than those shown in Figure 18. To summarize, combining the results of this research with those of previous publications, it appears that film climbing can

occur under a wide variety of circumstances. The possible particle types include gold nanoparticles[58, 59], fumed silica[62], Teflon fluoropolymer[62], and FeOOH, Fe_2O_3, Fe, and colloidal silica (present research). The particles include a variety of surface chemistries and sizes ranging from <20 nm for the gold nanoparticles, to well over a micron for the Fe particles and the spherical hydrophobic silica particles. Film climbing can be induced in a variety of fluid pairs: by coalescence of air bubbles in water[62], oil drops in water (this research and research of Au nanoparticles[58, 59]), water drops in oil (this research), or oil drops in ethylene glycol (this research). Thus we conclude that the film climbing behavior, and the corresponding qualitative features, are very general. We propose that any system in which (1) particles adsorb at a fluid/fluid interface but (2) do not stop coalescence, can grow films on the walls of the vessel. The remainder of this chapter describes more detailed experiments on one specific system, viz. the oil/water emulsions with FeOOH particles. These particles were chosen because the corresponding films are bright yellow, and hence are easy to image. Furthermore, the particles themselves are sufficiently large that they can be imaged adequately by environmental SEM. Section 3.2.2 considers the effect of varying the particle loading on the film climbing process. Sections 3.2.3 and 3.2.4 verify the two key hypotheses[59] underlying the physical picture of Figure 17, viz. (1) that film climbing occurs because of the spreading pressure of the interfacially adsorbed particles, and (2) that the final structure of the film consists of the particles sandwiched between layers of oil and water. Finally Section 3.2.5 examines the effect of the wettability of the walls on film climbing.
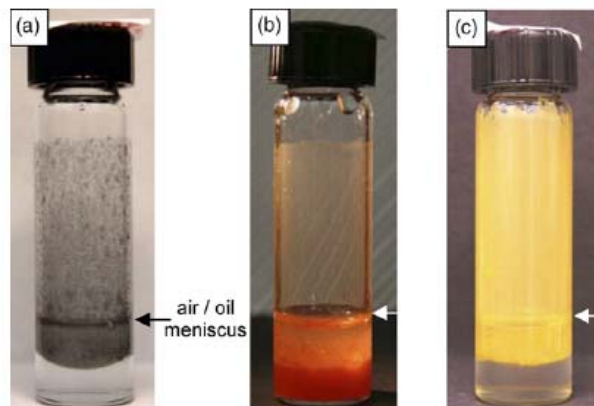
Figure 18. Climbed films with varied particle types and fluid pairs.
(a) carbonyl iron particles at oil/water interface, (b) Fe_2O_3 particles at oil/water interface, and (c) FeOOH particles at oil/ethylene glyool interface. Arrows show the position of each air/oil meniscus.

3.2.2 Effect of particle loading

The particle loading was found to affect the color and mobility of the films, and this will be discussed here. In the following, the particle loading is quoted as the mass of particles added to the vial, keeping the oil and water phase volumes fixed at 2 ml each. The particle loading, denoted by m, was varied from 1.4 mg to 0.014 mg. Films generated from the shake-and-stand procedure were imaged in at three different magnifications.

The images in the top row of Figure 19 were taken with a digital SLR camera. Figure 19a shows that at the highest loading of m= 1.4 mg (identical to Figure 16, but after full coalescence had occurred), the film is bright yellow. Interestingly, the bottom portion of the film (i.e. the oil/water meniscus) appears wrinkled and buckled. Such a buckled monolayer has been shown to occur when the particle monolayer is tightly crowded[32, 63]. With decreasing m, the color intensity of the films decreased (Figure 19a–d). At the lowest loading of m= 0.014 mg

(Figure 19d), the very faint color of the film made visualization of the fully climbed monolayer difficult, however, the climbing front could still be imaged while the film was still advancing up the walls of the vial. The decrease in color intensity with decreasing particle loading is likely attributable to a decrease in the interfacial concentration of particles in the film.
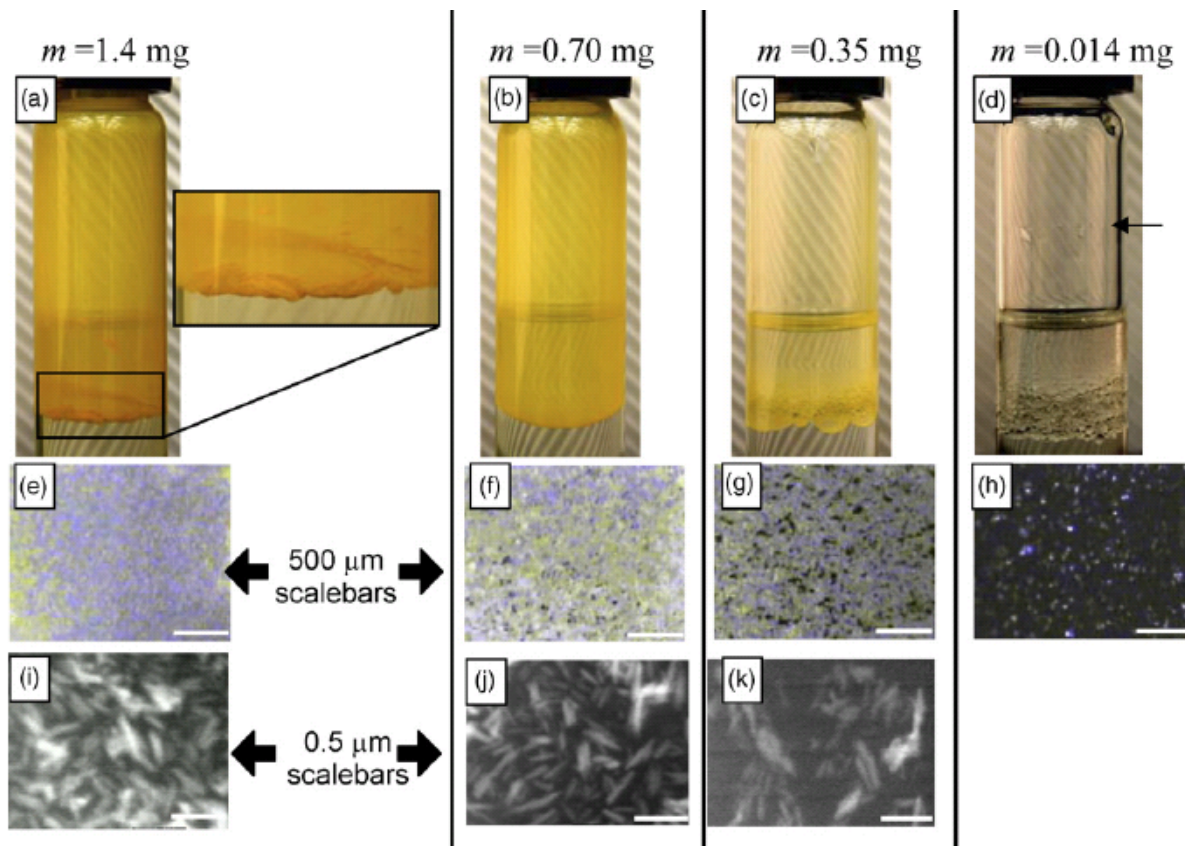
Figure 19. Film structures at the denoted particle loadings at three different maginifcations. (a)-(d) Macroscopic images with a SLR camera. Images (a)-(c) are fully climbed films, whereas (d) was captured during climbing (see text). The upper edge of the climbing film is indicated by the arrow in (d). The inset to (a) is a magnified view of the buckled/wrinkled file. (e)-(h) Optical images of the climbed film with a zoon-lens. Regions with particles appear white. (i)-(k) E-SEM images, with particles appearing white.

To verify this, the shake-and-stand experiments were repeated but imaging was conducted with a CCD-video camera equipped with a video-zoom lens. At this higher magnification, the decrease in interfacial concentration in the film with decreasing particle

loading is clearly apparent (Figure 19e–h). At the highest loading of m= 1.4 mg (Figure 19e), the film appears featureless, characteristic of a tightly packed layer of particles with little intensity contrast. With decreasing particle loading, some contrast in the form of dark spots appears, and at m= 0.35 mg (Figure 19g), the film has several holes in which no particles are visible. At the lowest loading of m= 0.014 mg loading (Figure 19h), the film is comprised of sparse white specks (presumed to be either individual particles or small particle clusters), with large areas of the film appearing to be particle free.

Finally, we sought to image the structure of the films at the resolution of individual particles. Standard SEM is not suitable for this purpose because while it is easy to evaporate all the water from the films, it is not possible to evaporate all the mineral oil. Even traces of oil are sufficient to compromise the high vacuum of a SEM chamber. Therefore we imaged films using environmental scanning electron microscopy (E-SEM), which permits imaging under modest vacuum levels at which the presence of mineral oil is not a concern.

The shake-and-stand procedure was repeated in vials scored on the outside with a diamond cutter, and the vials were allowed to stand for 2 days to allow the films to drain. The oil and water in the vials was then withdrawn with a pipette. We sought to characterize the structure of the as-climbed film, and hence it was important to verify that the structure was preserved prior to electron microscopy. Therefore, during the entire 2 days of standing and the subsequent pipette withdrawal, the films were imaged with the video-zoom lens. Such imaging showed that at m= 0.014 mg, the film structure was not preserved when withdrawing oil and water with a pipette, and hence this sample was not studied further. At the higher particle loadings however, the films were immobile (see below) and did not appear to undergo any changes during the standing or the withdrawal. Therefore these films were deemed suitable for subsequent imaging; these vials were broken along the scores, and fragments of the glass walls

were examined by E-SEM at a voltage of 28 kV, 8 mm working distance, and a vacuum of 3 Torr. E-SEM does not require samples to be coated with a conductive layer of metal, hence we believe that these images (Figure 19i–k) are truly representative of the structure of the as-climbed films. These images confirm that m= 1.4 mg corresponds to a tightly packed film, and that films grown from lower particle loadings do have particle free regions. Indeed, Figure 19k indicates that at m= 0.35 mg, the film is far from close packed.

Much insight can be gained by comparing the area required to accommodate all the particles at the interface, $A_{particle}$, with the nominal area of the climbed films, A_{film}. To make this comparison, we assume that each particle is a cuboid of dimensions $L \times w \times w = 0.6$ μm ×0.12 μm ×0.12 μm as estimated from Figure 15a. Then assuming that particles lie flat on the interface, and that all particles are adsorbed on the interface, a simple geometric calculation yields the area required for the interfacially adsorbed particles. These numbers are listed as a function of particle loading in Table 3. The vial diameter (13.5 mm) and the typical height of the climbed films (about 35 mm) yields the total interfacial area, A_{film}, after film climbing is complete; this number is noted in the third column of Table 3. A wall coverage percentage was defined as $A_{particle}/A_{film}*100\%$ to allow easy interpretation of the images in Figure 19.

Table 3. The wall coverage% calucation.

Loading, m (mg)	Interfacial area of particles, $m/(w\rho)^a$ (mm^2)	Nominal area of climbed film, $\pi R^2 + 2\pi Rh^b$ (mm^2)	Wall coverage%^{c}	Remarks
0.014	29		2%	Sparse particles in film
0.35	725	143+1484 = 1627	45%	Some particle-free regions
0.7	1450		89%	Little particle-free regions
1.4	2900		178%	Close packed with buckling

a. This assumes that the particles have dimensions of $L \times w \times w$ (see text), that all particles are at the interface, and that they are tightly packed. ρ is the particle density, 4.03 g/cm^3.
b. Here the vial diameter is $2R$=13.5 mm, and the film height is assumed to be h=35 mm.
c. The wall coverage is defined as interfacial area of particles/ nominal area of climbed film*100%.

Under this definition of wall coverage, an over-100% wall coverage simply means that the film area is not sufficient to accommodate all the particles even if they are tightly packed (Figure 19e and i), thus causing the film to buckle (Figure 19a). The wall coverage% for the samples of particle loading m =0.35 mg and m =0.7 mg are 45% and 89%, respectively. The calculation seemed to be very consistent to the film microstructures in Figure 19f, g, j and k. It can also be used to explain the sparse distribution of particle in Figure 19h.

Particle loading was also found to dramatically affect the mobility of particles within the film. This was clearly visible in observations of climbing films at the high magnification of the video-zoom lens. At m= 1.4 mg, the film climbed like a rigid "sheet", the advancing edge of the climbing film was straight and horizontal, and different parts of the film climbed at exactly the same speed with no relative motion within the film. At lower loadings, individual particles or particle clusters had substantial mobility, the advancing edge was jagged, and at any instant, different regions of the film had different upward climbing velocities. Finally, at the lowest loading of m= 0.014 mg, the film remained highly mobile even after climbing: even after 2 days of standing the vial, the white specks evident in Figure 19e could be set in motion by disturbing the vial even slightly. These changes in film mobility with particle loading will become evident in another context in Section 3.2.3 in this chapter.

Finally, Binks et al.[59] have speculated that in some cases, their gold nanoparticles films may consist of multiple layers. We have seen no evidence of multilayer formation in our experiments, and our E-SEM images seem to suggest that the films are monolayers. Yet, the FeOOH films at high concentration can readily fold, wrinkle and buckle as seen in the inset to Figure 19a. These wrinkles and folds relax and reform upon tilting the vial to disturb the monolayer; it is therefore conceivable that such an ability to form folds may permit multilayer formation in some cases.

3.2.3 Direct verification of the film structure

As mentioned at the end of Section 3.2.1, one essential feature of the physical model of film climbing[59] is that the final film structure is comprised of a layer of particles between films of water and oil. To verify this directly, we contacted the surface of the film, first with a drop of oil and then with a drop of water using the experimental assembly illustrated in Figure 20a. A Hamilton microsyringe with a 28 gauge needle (0.36 mm, also the dimension of the scale bars in images of Figure 20), was attached to a micrometer-translation stage. It was then placed with its tip close to the inner wall of a freshly shaken vial. After film climbing was complete and the particles in the monolayer had stopped moving, the microsyringe was translated towards the film until the drop of liquid (oil or water) at the tip of the syringe contacted the monolayer. This experiment was conducted at two different particle loadings: m= 0.35 mg (same as Figure 19c), and m= 1.4 mg (same as Figure 19a). The drop contact experiments were recorded as movies and can be found in the supplementary materials online[16]. Some frames extracted from movies are shown in Figure 20. At both particle loadings, upon contacting the monolayer with the oil drop (Figure 20b and d), the oil drained away without disrupting the monolayer. Immediately after oil coalescence, the oil spread radially outwards with no sharp meniscus visible. These observations strongly indicate that the top surface of the monolayer is a film of oil.
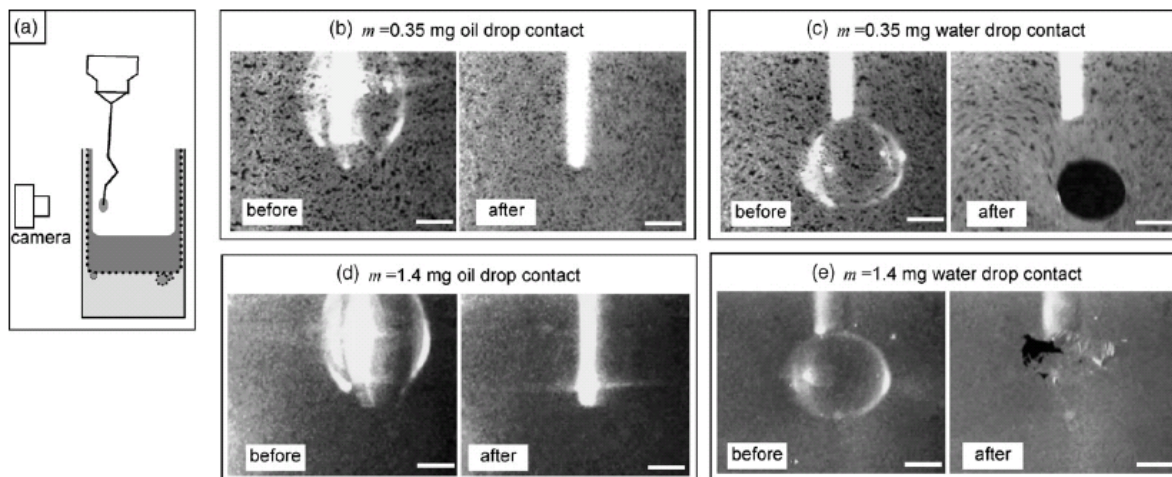
Figure 20. Drop contact experiments to verify the structure of climbed films.

(a) Schematic of contacting climbed films with drops of oil or water. The film is contacted with an oil drop in (b) and (d) and with a water drop in (c) and (e). In each pair of images, the left image is before drop contact, and the right image is after drop contact. The scale bar in each image is 0.36 mm, and the needle would appear to be the same diameter if it were in sharp focus. The oil wets the outer surface of stainless steel needle, whereas a water drop remains pendant. Hence oil and water drops appear to be of different shapes.

In contrast, upon contacting the films with a water drop, the water did not spread evenly on the surface of the film confirming that the top surface of the film is not water. Instead Figure 20c and e show that the water drop coalesced with the film, but left a hole in the monolayer. This indicates that the water drop coalesced not with the top surface of the film, but with an underlying layer of water. Certainly, such coalescence with an underlying water layer cannot occur without disrupting the particles in the monolayer. In summary, these experiments provide strong support for Figure 17d, viz. that the final film is comprised of a particle monolayer sandwiched between layers of oil and water[59].

The drop contact experiments also illustrated the dramatic difference in the mobility of the monolayers with changing particle loading mentioned at the end of Section 3.2.2. At *m*= 0.35 mg, upon contacting an oil or water drop, a large area of the monolayer becomes mobile and

different parts of the monolayer move readily with respect to each other. In contrast, at m= 1.4 mg, coalescence affected the monolayer only locally. Moreover, the hole created in the m= 1.4 mg film (**Figure 20**e) is jagged with some wrinkles in the surrounding area, indicative of a jammed and completely immobile monolayer.

3.2.4   Spreading pressure due to particle adsorption

As mentioned in Section 3.2.1, the postulated mechanism for film climbing is that as coalescence deposits particles at the continuous oil/water interface, the local increase in particle concentration causes a surface pressure (or spreading pressure), which in turn drives film growth. It is therefore crucial to establish that these particles can exert a surface pressure *at all*, and if so, verify that the pressure is sufficient to explain film climbing. Surface pressure can be measured using a pendant drop apparatus, but for these experiments, the shake-and-stand procedure of adsorbing particles at the interface is not suitable. Hence we devised an alternative procedure. A 0.07 wt% particle/water suspension was charged into the syringe of the pendant drop apparatus (Krüss DSA100) and a drop of this suspension was injected into the oil phase held in a glass cuvette. The drop shape of a pendant drop is balance by the weight of the drop ($V_{drop}\Delta\rho$) and the interfacial tension ($\sim\frac{\alpha_{AB}}{R}$).   This axisymmetric drop shape (i.e. *r(z)*, radius as a function of hanging direction) was analyzed by fitting the drop shape to Young-Laplace equation in order to obtain the interfacial tension. At short times, the interfacial tension was found to be close to that of oil/water (~62 mN/m). With time, as the particles adsorbed at the oil/water interface by sedimentation or by Brownian motion, the interfacial tension reduced to about 25% of its original value (Figure 20).
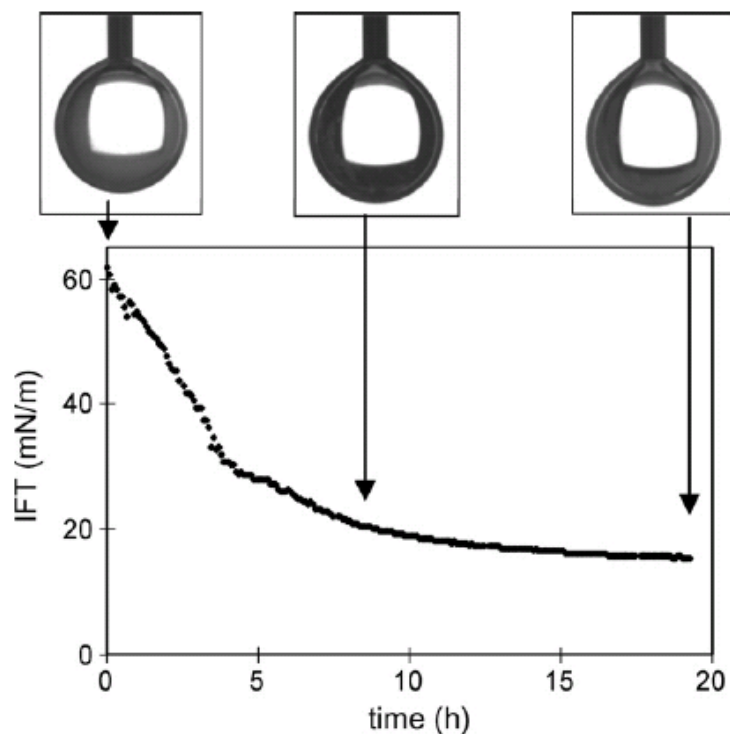
Figure 21. Interfacial tension (IFT) vs. time, and corresponding pendant drop shapes.

(At t=0, t=8.33h, and t=18.6h.)

The final value of 15.5 mN/m at 19 h is not an equilibrium value and the interfacial tensionwas still reducing gradually. It is noteworthy that the Young-Laplace equation fits the shape of pendant drop throughout the experiment, suggesting that the interfacial tension remained uniform over the surface of the drop as particles adsorbed. The results of Figure 21 demonstrate that that adsorbed particles can exert substantial surface pressures. Non-interacting "hard" particles at modest interfacial concentrations can only exert relatively small surface pressures (roughly RT×interfacial concentration), thus the substantial surface pressures of Figure 21 are likely attributable to repulsion between interfacially adsorbed particles[3, 29, 64].

It is of immediate interest to test if the magnitude of surface pressure found here (about 40 mN/m) is sufficient to support a film with the structure of Figure 17d. We write a simple force balance at equilibrium for the situation of Figure 17d:

53

$$\frac{d\pi}{dz} = \left(t_o \rho_o + t_w \rho_w + m_p \right) g = t_{total} \rho_{ave} g \qquad (3.1)$$

where t_o and t_w are the thicknesses of the oil and water layer respectively, ρ_o and ρ_w are their densities, m_p is the mass of particles per unit area of the film, π is the surface pressure, and z is the distance coordinate along the vertical direction. The quantity in the parenthesis has been defined as $t_{total} \rho_{ave}$, which is the mass per unit area of the film. The above equation essentially states that at equilibrium, the weight of the film must be balanced by a gradient in the surface pressure (i.e. the Marangoni stress) exerted by the particles. Integrating the above equation over the height of the film (or equivalently, performing a force balance over the entire height, h, of the film) obtains:

$$\pi(h) - \pi(0) = \int_0^h t_{total} \rho_{ave} g \; dz \qquad (3.2)$$

i.e. the weight of the entire film is balanced by a difference in spreading pressure at the bottom vs. at the top. We first note that *at equilibrium*, the film cannot be significantly thicker than the particle size; any excess oil or water would drain down with time. Accordingly, an order of magnitude estimate of the weight of the film may be obtained by simply assuming that the total thickness of the film (water layer, particles, and oil) is equal to the size of the particles (about 0.6 μm in their largest dimension), the mean density of the film is 2000 kg/m^3, and the film height is typically at least 20 mm in our experiments. Substituting these numbers obtains $\pi(h) - \pi(0) = 0.2$ mN/m. Thus, only a small difference in surface pressure (and presumably a small difference in particle concentration) is sufficient to support the weight of the film at equilibrium.

Since the pendant drop experiment measured surface pressures of over 40 mN/m, we conclude that the particles can easily develop the surface pressure necessary to support the

weight of the film at equilibrium. In fact, the above analysis suggests that the measured surface pressure may be able to sustain an equilibrium film height of at least two meters! Indeed, Binks et al.[59] were able to demonstrate films of the order of 1 m in height with gold nanoparticles, although the procedure was more complex than the simple shake-and-stand procedure followed here.

3.2.5   Effect of wettability of walls

For gold nanoparticles, the wettability of the walls was shown to play a significant role in the film climbing process. Binks et al.[59] showed that if the glass/water/oil contact angle (as measured through the water) was less than 90°, i.e. the glass was relatively hydrophilic, the film climbed upwards. For hydrophobic glass surfaces with contact angle exceeding 90°, the film growth was directed downwards. We sought to verify that the same is true for the much larger FeOOH particles considered here.

A glass vial was laid on its side and 0.5 ml of a 0.005 M solution of OTS in hexane was added using a pipet. After two minutes, the solution was withdrawn with a pipet, the vial rinsed with pure hexane, and finally with water. The vial was kept in the same horizontal position throughout this procedure. The net result of this procedure was to cause a vertical strip of the vial to become hydrophobic. The shake-and-stand procedure was then repeated in this vial. As shown in Figure 22, whereas the film climbed upwards over most of the vial surface, in the hydrophobic portion, the particle film climbed downwards, consistent with Binks et al.[59] Besides, the downward film grew more readily (its growth appears complete at 1 s), presumably because downward film growth is aided by gravity.
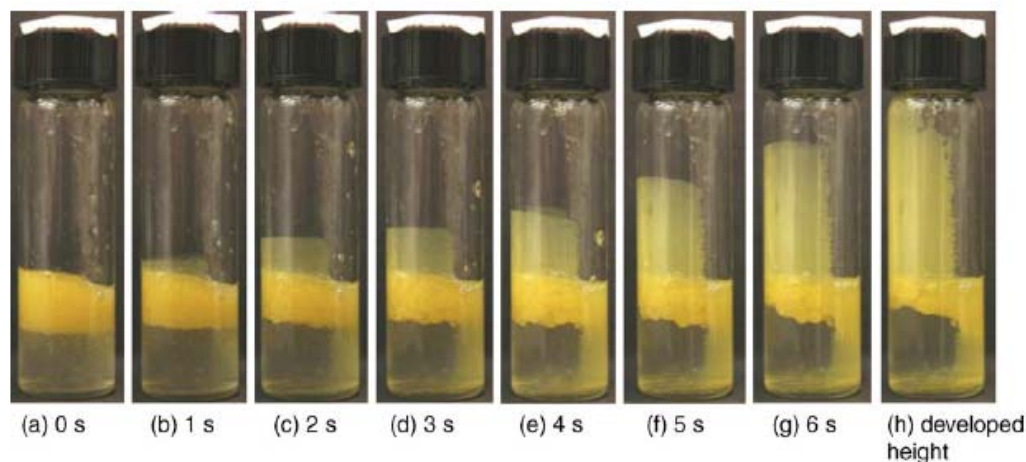
Figure 22. Effect of hydrophobicity of the walls of the bottle.

The time after stopping the shaking of the vial is noted below each image.

Mayya and Sastry[58] have also noted that gold nanoparticle film formation was considerably faster if the glass surface was prewetted, and once again it is of interest to compare the behavior of the larger FeOOH particles. In the standard procedure of Section 3.2.1, the glass surfaces are, of course, already wetted during the shaking. To test the effect of prewetting, the oil/water/particle mixture was shaken in one vial, and then carefully transferred into another vial with a pipet. Two cases were contrasted. If the emulsion was transferred into a vial which had been previously rinsed with pure water, coalescence and film climbing occurred unimpeded, similar to Figure 16. In contrast, if the emulsion was transferred into a dry vial, the oil drops were found to coalesce, but only incomplete film growth was evident. The final state corresponded to Figure 23a and b: a film of particles reached a few mm above the oil/water meniscus, but never climbed above the oil/air meniscus. In summary, unlike for gold nanoparticles[58], for the FeOOH particles considered here, prewetting does not merely accelerate film formation, but is an *essential* condition for film formation: without prewetting, films do not climb at all.

56
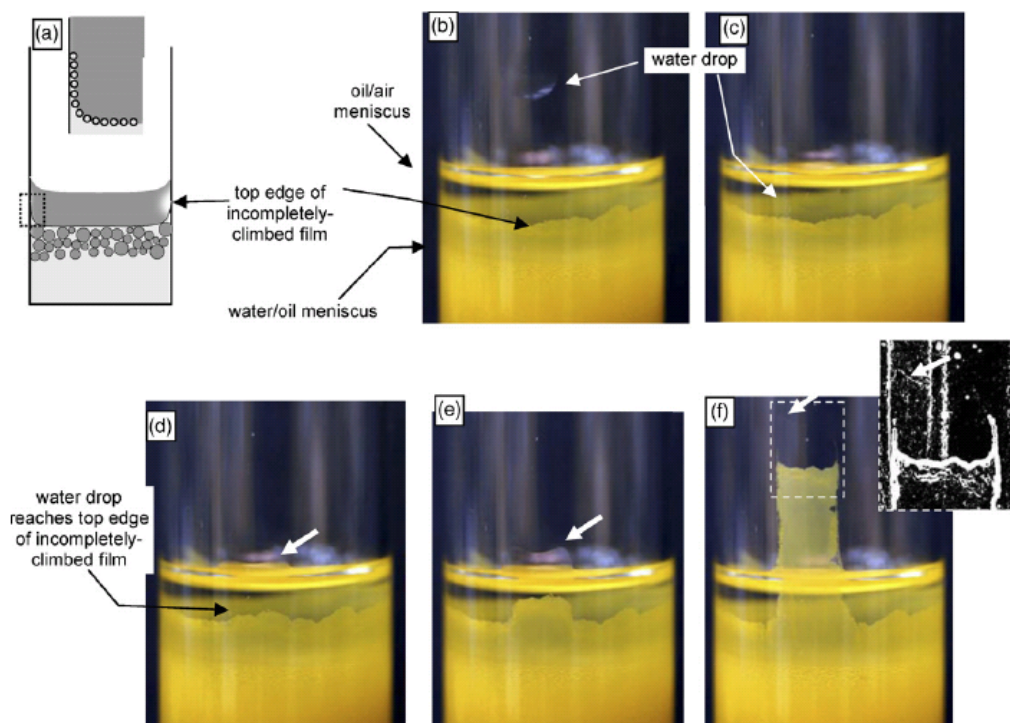
Figure 23. Effect of prewetting of the walls.

(a) Schematic picture and (b) experimental image of a shaken emulsion transferred to a dry vial. The inset to (a), which is a magnified view of the dotted rectangle, shows that a film of particles does form on the wall, but does not climb very high: the top edge of this "incompletely climbed film" is marked in (a) and (b). A water drop was rolled down the wall of the vial as seen in (b); (c) the water drop has entered oil phase, but not yet reached the top edge of the existing particle film; (d)-(f) the water drop reaches the existing particle film, which then climbs up the track left by the water drop. An oil front climbs ahead of the particles; the upper edge of this oil front is identified by the white arrows in (d)-(f). In (f), the oil front is faint, but clearer in the insert which shows a portion of the image subjected to an edge detection algorithm.

What is the reason for incomplete film climbing on dry glass? We speculate that film climbing is frustrated by the contact angle hysteresis at the glass/water/oil contact line, i.e. the particles at the oil/water interface in Figure 23a and b still exert a significant surface pressure, but this pressure is insufficient to advance the oil/water contact line on the dry glass surface. To

57

verify that such a "frustrated" particle monolayer is still capable of film climbing, a water drop was rolled down the inner wall of the glass vial (this drop is visible on the wall of the vial in Figure 23b). As soon as the drop reached the top edge of the incompletely-climbed film (Figure 23c), a particle film climbed up the track left by the water drop (Figure 23c-e). This confirms that the incompletely-climbed monolayer is capable of film-climbing, provided a prewetted wall is made available.

The most remarkable aspect of Figure 23 is that as soon as the water drop rolling down the wall reached the top edge of the incompletely-climbed film, a colorless *second* climbing front (pointed by the arrows in Figure 23d, e and f) was visible far above the advancing yellow-colored particle film. A movie capturing this process can be found online in the supplementary materials[16]. This upper climbing front appears to be initiated at the oil/air interface, i.e. the climbing particles are preceded by a film of oil alone. At longer times, it becomes increasingly difficult to image the upper front, yet, Figure 23f suggests that it remains a few mm ahead of the climbing particles for much of the climbing process. We are uncertain about the origin of this oil front but present the following hypothesis: as soon as the water drop reaches the top edge of the particle-laden oil/water interface, the particle monolayer starts climbing at a high velocity. The corresponding bulk flow in the film of water induces an upward motion over the entire oil/water interface – even in parts of the interface not yet covered with particles.

3.3   SUMMARY AND CONCLUSIONS

We have studied an unusual film-climbing phenomenon in which coalescence of an unstable Pickering emulsion contained in a vial induces a particle-film to grow on the walls of the vial.

While this phenomenon has been described previously with nanoparticles at the oil/water or air/water interface, we show that it is very general: film growth can be induced by particles of a variety of types, and sizes ranging from a few nm to a few μm, can be induced in non-aqueous systems, and can be induced by coalescence of either oil-in-water or water-in-oil emulsions. Furthermore, many of the features of film growth documented previously for nm-sized particles are found remain valid even when particles are far larger. Accordingly, we postulate that any emulsion in which (1) particles adsorb irreversibly at the interface, but (2) do not stop coalescence, will show film growth on the walls of the vessel containing the emulsion.

The mechanism proposed by Binks et al.[59] is that since particles cannot desorb from the interface, coalescence raises the interfacial concentration of the particles. The corresponding rise in surface pressure induces a monolayer of particles to push the oil/water interface up the walls of the vial. We have verified some key aspects of this postulated mechanism in one specific emulsion system composed of oil, water, and FeOOH particles. In particular, by contacting the films with drops of oil or water, we confirm that the films do indeed have a three-layer structure of particles sandwiched between layers of oil and water. A simple force-balance suggests that at equilibrium, a very modest surface pressure is sufficient to sustain the weight of the film. Pendant drop experiments show that particle adsorption at the oil/water interface can easily induce the surface pressures necessary to explain film climbing. Images of the films across a large range of magnifications show that tight packing is not a necessary condition for film growth; some films are very sparsely populated with particles. Finally, our experiments show that films do not grow on "dry" walls; prewetting is a necessary condition for film-growth.

4.0 CONTROLLED JAMMING OF PARTICLE-LADEN INTERFACES USING A SPINNING DROP TENSIOMETER

When particles adsorb at a fluid-fluid interface at a sufficiently high concentration, the interface loses mobility and displays solid-like characteristics. This is a phenomenon called "interfacial jamming". The jammed particle-laden interface (i.e. the jammed monolayer) can be solid-like with significant mechanical robustness, and one of its remarkable consequences is the existence of stable non-spherical drops or bubbles[5]. On a non-spherical jammed drop or bubble, the non-uniform capillary stresses associated with a non-spherical shape are supported by localized stresses in the solid-like monolayer. Furthermore, jamming can be used to arrest interfacial-tension-driven phase coarsening, and thus it is the key to determine the arrested structure and the arrested length scale in bijels (introduced in Section 2.4).

In this chapter, we develop a new jamming study method which emphasizes interfacial-tension-driven jamming instead of applying externally-imposed compression. A systematic study of jamming at particle-laden fluid interfaces is conducted using a spinning drop tensiometer (SDT). A drop of mineral oil surrounded by ethylene glycol is spun into a cylindrical shape in a SDT. With decreasing rotational rate, the cylindrical drop retracts due to interfacial tension, thus reducing the interfacial area. In the case of particle-covered drops, drop retraction causes an increase in interfacial particle concentration. Accordingly, when the specific interfacial area becomes comparable to that of a close packing of particles, interfacial jamming

occurs and drop retraction is arrested. From drop shape analysis, we can calculate the interfacial area for each drop. By various plots, we gain insight on the behaviors of 2D jamming on drop surfaces. We study both monolayer compression and expansion by monitoring the change of drop shapes during the stepwise decreasing-rpm and increasing-rpm procedure. Because the rpm of the spinning apparatus can be promptly varied, the jamming method that we developed provides a means to study the dynamic effect of jamming. The different behaviors of particle layer at the polar/nonpolar and nonpolar/nonpolar fluid interfaces are also contrasted.

4.1   CONVENTIONAL APPROACHES AND OUR APPROACH

The key to study jamming systematically is to decrease the interfacial area in a controlled fashion. Past experiments have principally used two methods to reduce the interfacial area systematically. The first is a Langmuir trough (Figure 24a), in which a physical barrier (or two barriers for symmetric compression) is moved to compress the particle monolayer[4, 21, 29, 65]. In this case, the compression is driven from the edges of the monolayer and the nominal interfacial area is directly controlled. In such experiments, jamming can occur if the monolayer is compressed sufficiently. Further decrease in the nominal interfacial area can cause interfacial buckling (an out-of-plane distortion or wrinkling of the monolayer), i.e. the nominal interfacial area becomes smaller than the actual area. The second method is a shrinking drop (or bubble) method, in which the monolayer is placed on the surface of a pendant or sessile drop, and fluid is withdrawn from the drop (Figure 24b)[32, 33, 63]. In this case the volume of the drop (rather than the area) is directly controlled. The drop shape follows Young-Laplace equation, and hence the interfacial area reduces in a predictable fashion, at least as long as the interface remains

unjammed. In these experiments as well, sufficient withdrawal of the drop phase fluid can induce interfacial jamming, and further withdrawal can be accompanied by interfacial buckling[32, 33, 63].
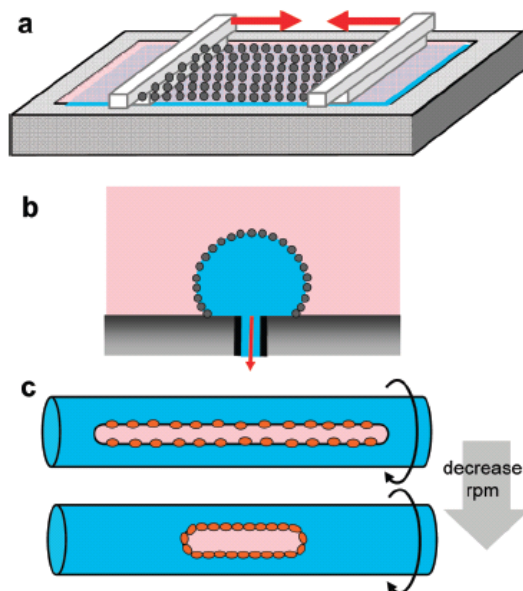
Figure 24. Methods to study properties of particle monolayers and interfacial jamming.

(a) Langmuir trough; (b) sessile drop; (c) spinning drop tensiometer

There are however several differences between interfacial jamming during bijel formation and interfacial jamming in a Langmuir trough or on a shrinking drop. Unlike in the two methods of Figure 24a and b, the bicontinuous interface in a bijel does not have physical barriers, nor does the volume of the fluid change. The driving force for the decrease in interfacial area in a bijel is interfacial tension, or more precisely, gradients in capillary pressure due to difference in curvature along the interface. This mechanism is quite different from a shrinking drop or especially from compression in a Langmuir trough. Furthermore, during bijel formation the interfacial driving force remains nearly constant (or decreases) during the

coarsening process, whereas properties such as interfacial viscosity or modulus increase as the particles pack more closely. Therefore, the rate of decrease in interfacial area is expected to reduce as jamming is approached. In contrast, in a Langmuir trough or a shrinking drop, the area is decreased at a prescribed rate. Finally, we hypothesize that buckled states, which result from trying to decrease the area below that required for jamming, are unlikely to occur in bijels since interfacial coarsening is expected to stop once the interfacial yield stress approaches the interfacial tension driving force.

Here we propose an alternate method of reducing the interfacial area that is more representative of the jamming process in bijels. Specifically, as in bijels, in the proposed method, the decrease in interfacial area is induced by interfacial tension. The method uses the Spinning Drop Tensiometer (SDT, Figure 24c and Figure 25). When two fluids are spun in a tube along a horizontal axis, the lower density fluid "centrifuges" to the center and stretches into a cylindrical drop. The drop shape at equilibrium results from a balance between interfacial stress ($\sim \frac{\alpha_{AB}}{R}$) and centrifugal stress ($\sim \Delta\rho R^2 \Omega^2$). It has been shown that at equilibrium[66]:

$$\alpha_{AB} = \frac{\Delta\rho R^3 \Omega^2}{4} \quad \text{provided} \ (\frac{L}{2R} > 4) \tag{4.1}$$

where $\Delta\rho$ is the density difference of the two fluids, $2R$ is the diameter of the cylindrical drop, L is its length area, α_{AB} is the interfacial tension between the two fluids, and Ω is the rotational rate. The above equation is called Vonnegut's formula and is the basis for using the SDT to measure the interfacial tension between immiscible fluids. The SDT has also been used less frequently to examine the dynamics of interfacial tension driven shape changes in fluids. Specifically, by first preparing a long drop at high rotational speed, and then abruptly reducing the rotational speed, the retraction[67, 68] or capillary breakup[69] of a drop can be studied.
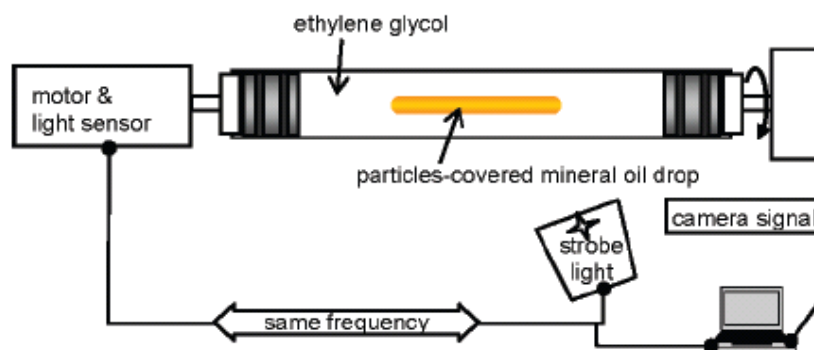
Figure 25. SDT experimental setup.

The strobe light and the rotor are operated under the same frequency by synchronizing the signal through a light

sensor. A camera (not shown) takes real-time images from above.

Such shape changes with rotational speed can also be used to change the interfacial area systematically. Specifically, as the rotational speed is reduced, the drop retracts and the interfacial area of the drop reduces in a predictable fashion. By covering the surface of the drop with a particle monolayer, the decrease in interfacial area may be used to induce interfacial jamming. Most importantly, as in bijels, the decrease in interfacial area and the eventual jamming is driven by interfacial tension/ capillary pressure. Other similarities with bijel jamming include the absence of physical barriers, the absence of spreading solvent, and the geometric analogy between an elongated drop and the fluid channels (the necks) in a bijel. In summary, the SDT method of Figure 24c is more representative of the eventual jamming of a bijel than Figure 24a and b.

In this chapter we study interfacial particle jamming experimentally in a well-controlled manner using a spinning drop tensiometer. Our previous research[16] on particle monolayers suggests that the adsorption of iron oxyhydroxide particles (FeOOH) onto the interface of mineral oil and ethylene glycol is fast, stable and convenient for visual observation because of

the intense yellow color of the particles[16]. In this chapter, a FeOOH particle-covered drop of mineral oil suspended in ethylene glycol was spun in the SDT, and jamming was induced by decreasing the rotational rate, and hence the interfacial area. Since the particle loading is known for a given sample, we can relate the interfacial particle concentration with rotational rate and deduce the conditions under which jamming occurs for different samples. We study the gradual jamming (slow decrease in area) and also the "dynamic" jamming (rapid decrease in area), and the effect of rotational rate history. We also show that the same particle monolayer at a nonpolar-nonpolar interface behaves completely differently from that at the glycol/oil interface. This study about the physics of jamming is intended to serve as the foundation for structure control through interfacial particle jamming in bijels.

4.2   MATERIALS AND EXPERIMENTS

4.2.1   Materials

Light mineral oil was obtained from Fisher Scientific Inc. Its density was determined to be 0.854 g/mL by weighing in a pycnometer vial. Ethylene glycol was also obtained from Fisher. Silicone oil (polydimethylsiloxane, Rhodorsil fluid 47 V10,000), obtained from Rhodia Inc., has viscosity and density of 10 Pa.s and ca. 0.96 g/mL.

Iron oxyhydroxide (FeOOH) particles were donated by Elementis Pigments Inc. The particles are polydisperse, elongated with an average length of about 0.6 μm (manufacturer specified), have a density of 4.03 g/cm^3 (manufacturer specified), and appear yellow in color. A

SEM picture of the particles is shown in Figure 29c. These same particles were used in the film-climbing research (chapter 3).

4.2.2 Sample preparation and experimental procedure

FeOOH particles of carefully weighed amount were first dispersed in mineral oil using ultrasonication for 10 min and followed by short vortex mixing. Three suspensions with the concentrations listed in Table 4 were prepared. In each case, the suspension was transferred to a syringe, and roughly 0.073 ml was injected into the precision-bore sample tube filled with degassed ethylene glycol. The exact volumes of the drops (calculated numerically from drop images; see below), and the corresponding particle loadings, are also listed in Table 4.

Table 4. Drop volumes and particle loadings for SDT samples.

Designation	FeOOH wt % in suspension	Drop volume (mL)	Particle loading (mg)
particle free	0	0.0755	0
F51	0.08	0.0735	51.5
F63	0.1	0.0728	62.2
F71	0.12	0.0714	71.4

The tube (12.7 mm diameter, 165 mm long) was closed with an endplug, mounted in the SDT, and spun in the tensiometer at a high rotational rate. Since the particles are denser than the oil, they migrate to the interface and get adsorbed. To prevent a multilayer of particles from forming at the interface, the tube was taken out from the tensiometer, held horizontally, and shaken gently so that particles not adsorbed at the interface would be dispersed back to the drop phase. The tube was then spun in the SDT again. This rotation and shaking was repeated several

66

times until the bulk drop phase appeared clear and there was no further change in drop dimensions at a fixed rpm. Throughout this procedure, the matrix phase (ethylene glycol), as well as the inner surface of the glass tube appeared to be clear, suggesting that no particle penetrates through the interface without being adsorbed.

After particles had been adsorbed at the interface, each sample was first brought to high rotational rate (e.g. 7000 rpm), and then the rotational speed was decreased in roughly 250 rpm decrements. After each change in rotational rate, images were taken after no less than two minutes to ensure that the drop shapes had reached steady state. To confirm that the drop shape images taken at the two-minute waiting time are indeed the steady drop shapes, we monitored one sample for 24 hr, and confirmed that the drop dimensions did not change after the first two minutes. This procedure of sequentially decreasing the rotational speed is dubbed the "ratedown" experiment.

Some samples were also subjected to a subsequent "rateup" experiment in which the rotational speed was increased in roughly 250 rpm increments.

An "abrupt stepdown" experiment was also conducted on the F71 sample, in which the rotational rate was decreased abruptly from roughly 6500 to 1500 rpm within a few seconds. Dynamics of the drop retraction during this experiment was recorded as a sequence of still images.

Similar experiments were conducted with FeOOH particles adsorbed at the mineral oil/silicone oil interface. In this case as well, the mineral oil has a lower density and hence forms the drop phase, thus once again, the particles were dispersed into the mineral oil and then allowed to centrifuge to the interface. Because mineral oil has slight solubility in silicone oil, the matrix phase silicone oil was pre-saturated with mineral oil: mineral oil drops were gently blended into silicone oil, and then allowed to float to the surface over several hours. The bottom

layer silicone oil, now saturated with mineral oil, was used as matrix phase. The interfacial

tension between the equilibrated phases was measured by the pendant drop experiment. The

value calculated using the densities of the pure oils was 1.05 mN/m; the equilibrated phases

likely have a somewhat lower density difference, and hence the above number is likely an

overestimate. In any case, this interfacial tension is far lower than the value of ~17.6 mN/m

measured for the glycol/oil system (see below), and reflects the low polarity of both species.

4.2.3   Imaging and image analysis

The experimental setup is shown in Figure 25 schematically. Images were taken with a video

zoom lens and a digital camera (EO-1312M), with the exposure time set to 0.1 s. The tube was

illuminated by a strobe light, which was triggered by a reflective sensor detecting the rotating

shaft of the SDT. The signal from the reflective sensor was also used to record the rotational rate

using a Labview interface. The cylindrical tube of the SDT causes optical lensing, making

spherical objects appear stretched along the tube diameter. This "diameter magnification" was

calibrated using an image of a spherical polyethylene bead of known dimensions suspended in

ethylene glycol in the SDT tube. All the images presented in this chapter have been corrected to

account for diameter magnification. The optical system has a resolution of slightly less than 50

μm.

Surface area and volume of the drop were calculated by numerical integration of the drop

shape profile. The edge of the drop was drawn manually since automatic edge detection was

found to be unreliable, especially when a striped background was used to enhance image quality.

The coordinates of the edge were exported and used to calculate surface area and volume with

the assumption of axisymmetric drop shape. The numerical calculations were validated by two

methods: (1) the interfacial area and volume of the spherical polyethylene bead was compared against numerical calculations, and (2) for all drops, the calculated volume was verified to be independent of rpm.

4.3 RESULTS AND DISCUSSION

4.3.1 Drop shapes and apparent interfacial Tension

At the initially-high rotational rate of the ratedown protocol, drop shapes of all samples are approximately spherocylindrical (cylinder with hemispherical end-caps), and their shapes result from a balance between interfacial and centrifugal forces as implicit in Vonnegut's formula (Eq. 4.1).

For the particle-free sample, as rotational rate is reduced, the drop retracts and its radius increases as illustrated in Figure 26a. The corresponding interfacial tension, calculated using Vonnegut's formula, Eq. 4.1, is shown in Figure 26b. At sufficiently low rpm, the drop radius approaches that of a sphere of the same volume as the original spherocylindrical drop. At very low rotational rate, the shape may also be affected by buoyancy effects. As long as the drop is long (L/2R>4), Vonnegut's formula suggests $R \propto \Omega^{-2/3}$. The observed exponent of -0.64 is close to, but not exactly identical, to the -0.667 expected, and accordingly, the interfacial tension appears to decrease slightly with decreasing rpm. It is not clear why this is so; it may be an artifact of the imaging procedure: any blurring of the image causes a larger error at small drop

diameter (i.e. at high rpm)[†]. In any case, the average interfacial tension between mineral oil and ethylene glycol by SDT method is 17.5 mN/m, which agrees well with the value 17.6 mN/m obtained from the pendant drop method (Krüss DSA100).
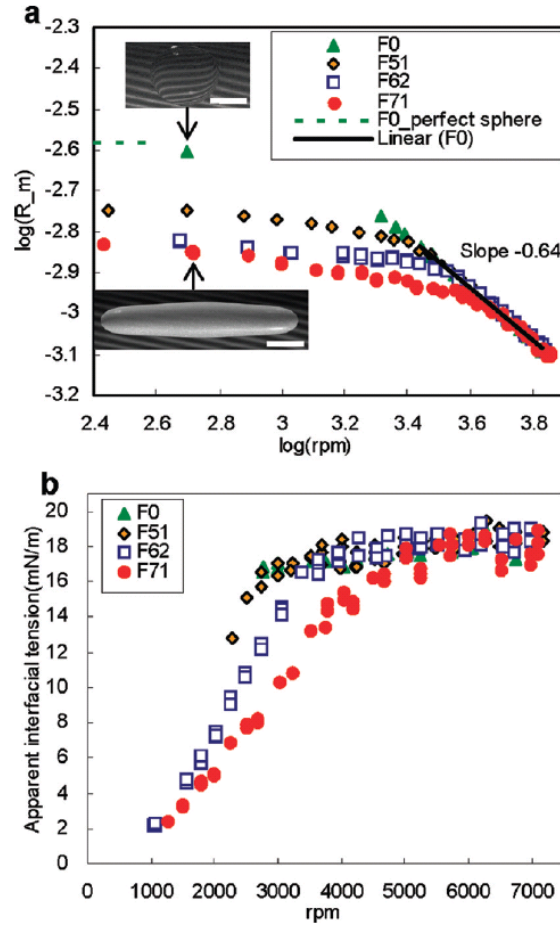
Figure 26. Plots of rpm versus drop radius and apparent interfacial tension.
(a) Log-log plot of drop radius in meters with rotational rate (rpm). Dashed line shows the radius for a spherical drop of the same volume as the particle-free drop. The scale bar in the insets is 3 mm. (b) Plot of variation of apparent interfacial tension with rpm, calculated from eq 4.1. Calculation was performed only for drops with aspect ratio > 4.

[†] There are two principal reasons for blurring: (1) uncertainty inherent in the finite spatial resolution of the digital camera, and (2) at high rpm, several strobe flashes occur during a single camera exposure of 0.1 s, and hence any image is a superposition of several images.

Figure 26a also shows the dependence of R on rpm for the particle-loaded drops. At high rpm, the radius of the three particle-laden drops is nearly equal to that of the particle-free drop. Upon reducing rotational speed, at some value of rpm, the radii of the particle-laden drops start deviating downwards from that of the particle-free drop. The rpm at which the deviation occurs increases with increasing particle loading. As rpm is reduced further, the radii of the particle-laden drops become increasingly insensitive to the rpm, i.e. the drop shapes no longer respond significantly to a decreasing rotational speed. This is due to interfacial jamming: the increasingly crowded particle monolayer hinders the drop from reducing its area, thus causing its shape (discussed below), and hence radius, to become insensitive to rotational rate. The drop shape is no longer determined by an equilibrium balance between centrifugal and interfacial forces, but instead depends on the mechanical history that led to the jammed interface. This will be explored further in Section 4.3.3.

We may apply Vonnegut's equation to find the interfacial tension of the particle-laden drops. At high rotational speed, the interfacial tension of the particle-laden interface is very close to that of the bare interface (Figure 26b) thus indicating that particles do not affect the interfacial tension significantly. At low rotational rates when interfacial jamming occurs, Vonnegut's equation, which assumes a balance between centrifugal forces and interfacial tension, is not strictly valid. Nevertheless, as long as the drop has a cylindrical mid-section with an aspect ratio exceeding 4, we may apply Vonnegut's equation to calculate an apparent interfacial tension, which is shown in Figure 26b. The apparent interfacial tension reduces to very low values at low rpm. We emphasize however that this low apparent interfacial tension calculated from Eq. 4.1 is not thermodynamically meaningful (hence the "apparent"): the radius of the drop is not small because the interfacial tension is low, but because the interface is jammed.

71

We will now consider the drop shapes in greater detail. Figure 27 shows the evolution of drop shapes with decreasing rpm for the drops with the lowest (F51) and the highest (F71) particle loading. The rotational speeds in Figure 27 were chosen to highlight the differences between the two samples. As mentioned above, all the drop shape images have been corrected to account for the refractive index magnification. At a relatively high rpm of about 5500 (Figure 27a and g), the drop shapes are nearly identical. Upon reducing the rotational rate stepwise to roughly 3500 rpm (b and h), both drops retract significantly. The intermediate shapes are not shown. Upon further decrease in rpm, a qualitative difference is evident: the F51 drop continues to retract (b-d), whereas the F71 drop shows no obvious change in length (h-j) as the rpm is reduced from 3500 to ~3000 rpm. The F51 drop continues retracting, and a much lower rotational speed (less than 1000 rpm) is required for its shape to become insensitive to rpm. In this chapter, such unchanging drop shape (and hence area) as the rpm reduces is regarded as the signature feature of interfacial jamming. The previous statement needs further qualification. Whether a system jams or not depends on the stress applied[70]. In the present case, drop retraction is driven by the difference between capillary pressure $\sim\alpha_{AB}/R$ (which tends to decrease the interfacial area) and centrifugal stress $\sim\Delta\rho\omega^2 R^2/4$ (which tend to increase the interfacial area). Thus, the quantity ($\alpha_{AB}/R - \Delta\rho\omega^2 R^2/4$) may be regarded as the interfacial stress driving the drop retraction. As the drop retracts and the interfacial concentration increases, the yield stress of the particle monolayer exceeds the difference between the capillary and the centrifugal stress, and hence the drop jams.
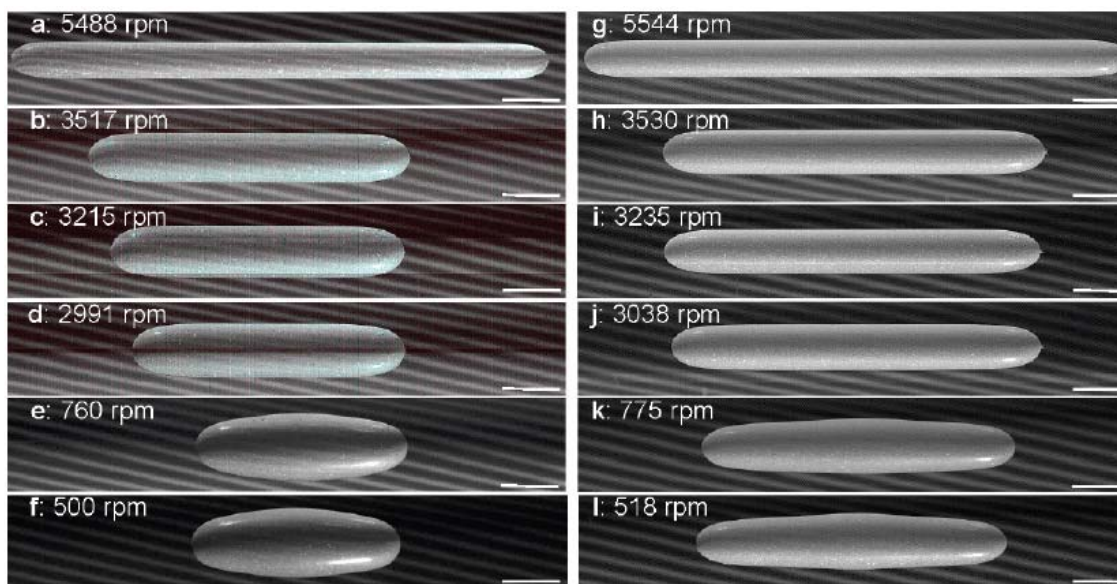
Figure 27. Drop images of F51 (a)-(f) and F71 (g)-(l) in the SDT jamming study.

Scale bars are 3 mm.

Upon further and more significant decrease in rotational rate (Figure 27k), the F71 drop does retract further, however, at such low rates, buoyancy effects may contribute to the shape changes. In this case (as well as in the F51 case), at the lowest rotational rates, the drop profile shows a distinct "bump" in its mid-section. In Section 4.3.3, we will show there is significant hysteresis in drop shape in this range of rotational rates, and hence such unusual bulging shapes cannot be regarded as equilibrium shapes (with the force balance including buoyancy, in addition to interfacial and centrifugal forces). Instead we believe that such unusual shapes are realized by plastic deformation of the jammed monolayer which is induced by buoyancy forces.

In the Introduction we hypothesized that in interfacial tension driven jamming, the interfacial area will stop decreasing once the interfacial yield stress approaches the interfacial tension, accordingly, we hypothesized that interfacial buckling will not occur. Indeed, interfacial buckling is not evident in any of the images of Figure 27. Calculations[34] suggest that under our jamming conditions with centrifugal accelerations of about $1 - 16$ m/s^2 (corresponding to the

73

surface our jammed drops), wavelengths of 100 – 400 μm are expected. These dimensions can be readily resolved by our apparatus, and indeed during fast changes in rpm when viscous stresses are significant, we have noted 100 μm scale ripples on the surface of drops. Yet, under equilibrium conditions, no ripples were evident. This lends tentative support to our hypothesis that monolayers jammed by interfacial tension do not buckle, although buckling at small amplitudes or at wavelengths smaller than 100 μm cannot be ruled out (the imaging resolution is slightly less than 50 μm).

Finally we note that the jammed drops are stable not only against retraction, but also against capillary instabilities. In elongated particle-free drops under quiescent conditions, long-wavelength capillary instabilities that can reduce the interfacial area can grow and eventually lead to drop breakup. However, since jamming prevents a decrease in interfacial area, capillary instabilities are suppressed as well.

4.3.2   Interfacial area, surface pressure isotherm, and jamming concentration

As mentioned in the Introduction, jamming is induced by a decrease in the interfacial area, and the consequent increase in particle concentration. The data of Figure 26 have be replotted in Figure 28a in the form of interfacial area of the drop for all four drops. As with the drop radius, all four drops show similar area at high rpm. This is not surprising: the four drops have a similar volume, and hence an equal radius implies equal area as well. At low rpm, the area of the particle-free drop approaches that of a sphere of the same volume. The area vs. rpm data for all three particle-laden drops deviates upwards from the particle-free drops at low rpm, with two trends evident: First, the rpm (and hence the area) at which the deviation occurs increases with particle loading. Second, the plateau value of the area at low rpm increases with particle loading.
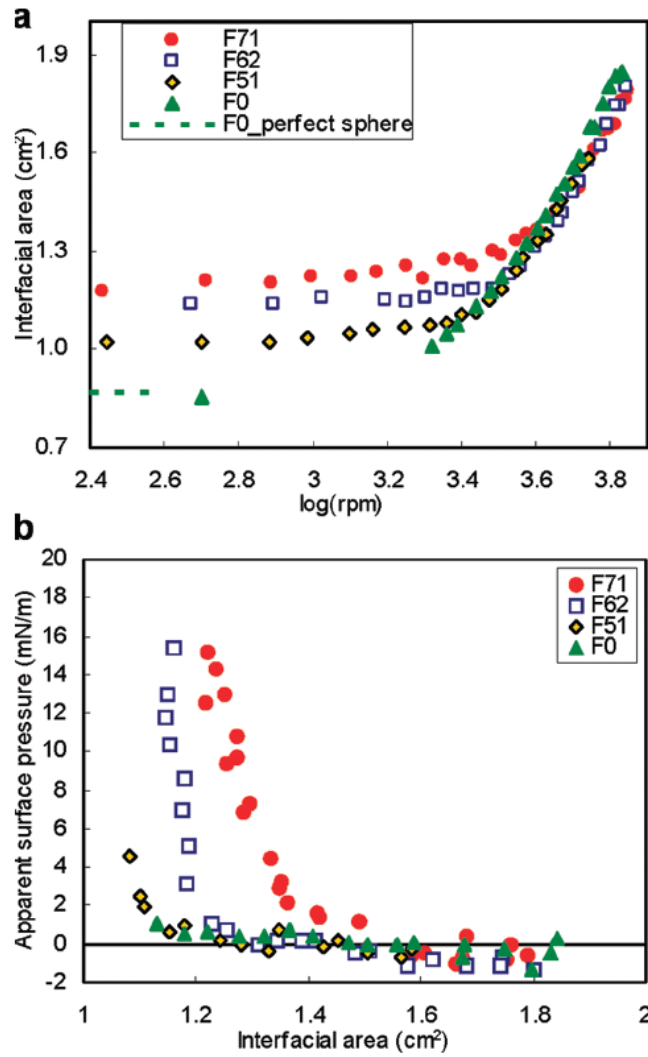
Figure 28. Plots of area versus rpm, and apparent surface pressure versus area.

(a) Variation of interfacial area with log(rpm) for a ratedown experiment. (b) Plot of apparent surface pressure versus interfacial area. See text for explanation for negative apparent surface pressures.

In experiments conducted in a Langmuir trough, it is traditional to represent the data in the form of surface pressure vs. area isotherms, and it is of interest to represent our data in the same form. The apparent interfacial tension, $\sigma_{apparent}$, can be calculated from Eq. 4.1 (as was done in Figure 26b); we can convert this into an apparent surface pressure

$\Pi_{\text{apparent}} = \sigma_0 - \sigma_{\text{apparent}}$, where σ_0 is the interfacial tension of the bare interface. In our case, we use the value of σ_0 obtained from the pendant drop experiment. Combining these surface pressures with the areas of Figure 28a yields the isotherms of Figure 28b. Once again, we stress that the apparent surface pressures do not have thermodynamic significance in the jammed state; they only reflect the values calculated from the Vonnegut equation. At the highest surface area values, the apparent surface pressures are slightly negative; this is an artifact caused by fact that the σ_0 from the pendant drop method (17.6 mN/m) was slightly lower than the highest apparent interfacial tension measured (19.0 mN/m). With decreasing surface area, the surface pressure increases until it is equal to the interfacial tension itself. These features are qualitatively similar to the surface pressure isotherms documented for oil/water systems[4]. Quantitatively however, our data show two significant differences. The first is that our isotherms stop at an area that corresponds to a jammed monolayer; unlike Langmuir trough experiments[4, 21, 29, 65], the monolayer does not further compress into a buckled state. As mentioned at the end of the previous section, when monolayer compression is driven by interfacial tension, buckling is not expected. The second significant difference is that the change from a low surface pressure to a high pressure is relatively abrupt. For the F71 drop, the apparent surface pressure rises from only 10% of its maximum value to its maximum value with a change in interfacial area of less than 20%. For the F62 drop, the transition appears even sharper; in effect in Figure 28a, the surface area of F62 is virtually constant after jamming. It is not clear why the transition appears more abrupt for the F62 drop. Yet, it is clear that these transitions are sharper than observed previously[4, 29]. This suggests that in the present system, the particles do not have a strong, long range repulsion for each other, and have a relatively "hard" interaction. Accordingly, a significant apparent surface pressure exists only when the particles are nearly in contact.

Ultimately, the phenomenon of 2D particle jamming is linked with interfacial particle concentration, rather than the interfacial area. For example, drops with a higher number of particle at the interface are expected to jam at a higher interfacial area (i.e. higher rpm) which is indeed apparent in Figure 26, Figure 27 and Figure 28. Accordingly, Figure 29a plots the data of Figure 28a in the form of specific interfacial area (i.e. area per gram of particles), on the assumption that all the particles are at the interface. This assumption is based on two observations: (1) as mentioned in Section 4.2.2, no particles are evident on the inner walls of the SDT tube indicating that particles do not cross the interface; (2) upon conducting the shake-and-spin procedure described in Section 4.2.2, there was no further change in drop dimensions at a fixed rpm.
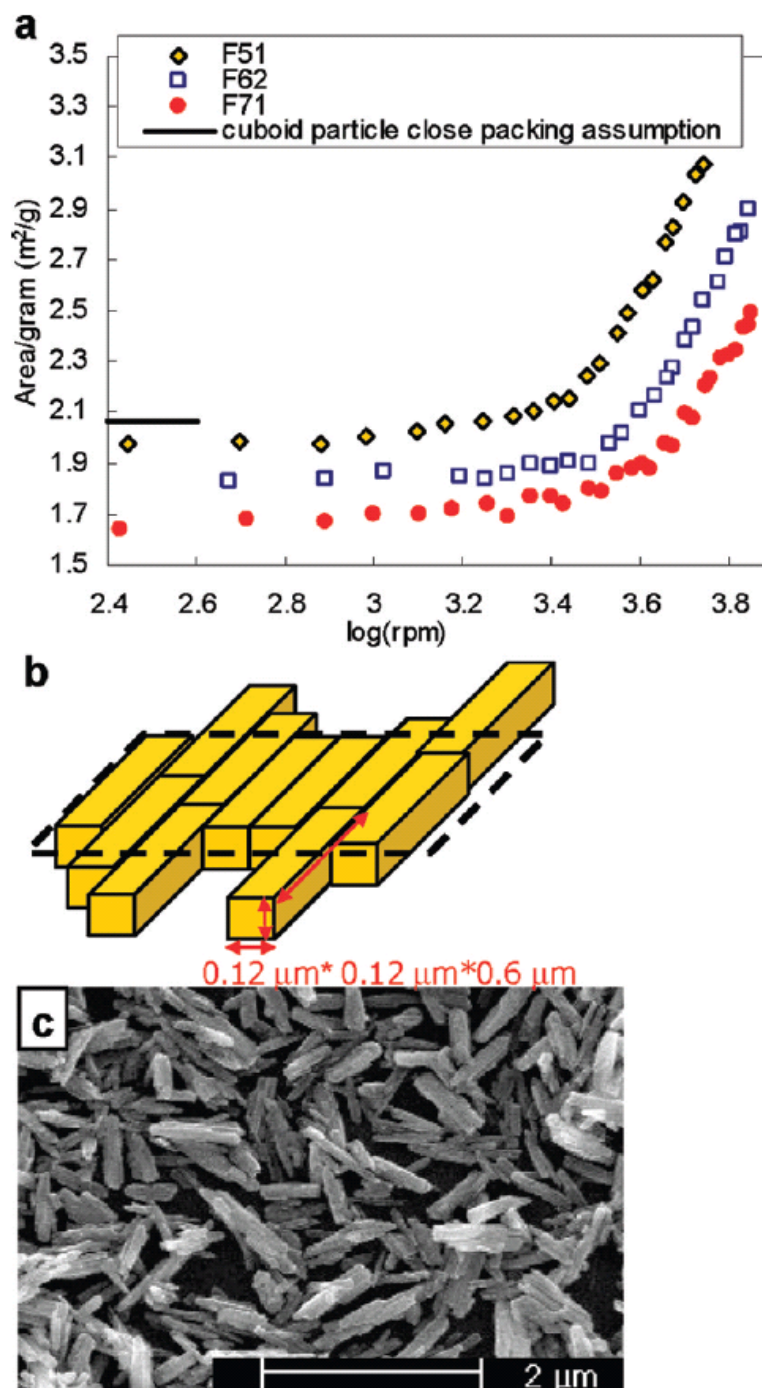
Figure 29. Specific interfacial area versus log(rpm) plot, particle packing assumption and SEM picture of particles. (a) variation of specific interfacial area of particles versus log(rpm). Solid horizontal line corresponds to 2D close paking of cuboid particles lying along the flat on interface as shown in figure b. (c) SEM picture of FeOOH particles.

The specific interfacial area in the jammed state may be crudely estimated by assuming that the particles lie parallel to the interface in a close-packed fashion (Figure 29b). In chapter 3[16], based on a SEM images such as Figure 29c, we had assumed that these FeOOH particles were cuboids of dimensions L × w × w = 0.6 μm×0.12 μm× 0.12 μm. These dimensions yield a close-packed specific interfacial area of 2.07 m^2/g, a value illustrated by the horizontal line in Figure 29a. Figure 29a shows that the experimentally-observed specific interfacial area (the plateau at low rpm) for all three drops is close to this horizontal line suggesting that in the jammed state, the particles are nearly tightly packed. Yet there are significant differences between the three samples: the specific interfacial area in the jammed state decreases with increasing loading. Quantitatively, the highest loading drop F71 had a 20% lower specific interfacial area (i.e. is 20% more tightly packed) than the lowest loading drop F51. It is not clear what microstructural differences may cause a more compact monolayer; considering the non-spherical shape of the particles, out-of-plane particle orientation ("flipped" particles[65]) may be responsible for more compact monolayers. Certainly it is also possible that the observed differences in specific interfacial area in the jammed state are in fact a failure of the above assumption that all particles are adsorbed at the interface.

4.3.3 Effect of rotational rate history: shape hysteresis and sudden stepdown

Previously it has been noted that expansion of a monolayer can display significantly different behavior than compaction. In general, the capillary pressure during an expansion was observed to be lower than during an preceding compression[30, 31, 33, 65, 71]. In order to examine the behavior of the present monolayers, at the end of the ratedown experiment, the F71 drop was subjected to rotation at successively higher rates to induce re-expansion of the interface.   Figure 30a

compares the area of the drop during the rateup sequence with the ratedown sequence, whereas

Figure 30b, c and d show drop shapes at selected rpms in the trajectory.
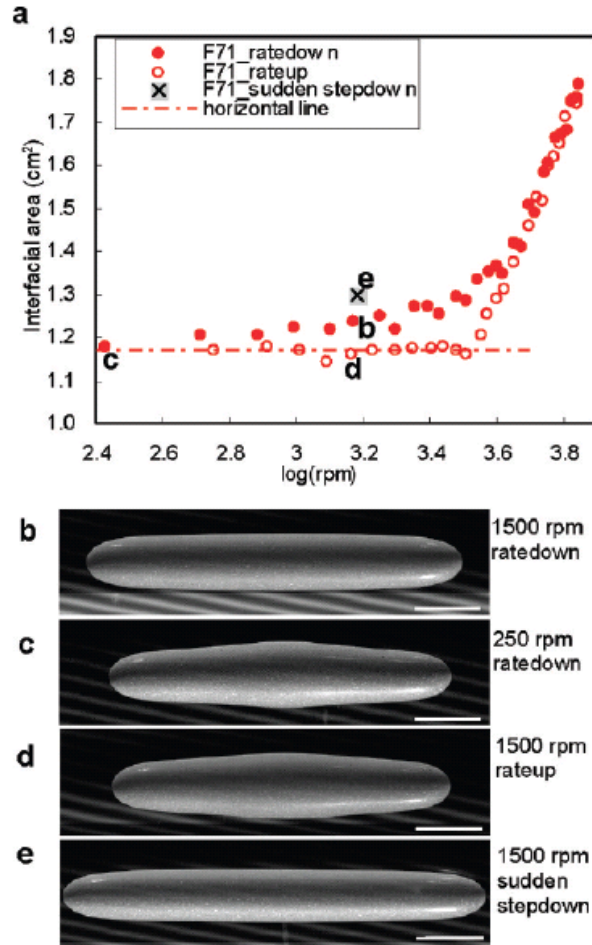
Figure 30. Shape hysteresis and sudden stepdown step in SDT jamming study.

(a) Comparison of ratedown experiment, rateup experiment, and sudden stepdown experiment for F71. The images corresponding to points labeled (b), (c), (d), and (e) are below the graph. Scale bars are 3mm.

Significant shape hysteresis is evident in these observations. In particular, it is clear that there is essentially no change in shape when increasing the rotational speed from ~250 rpm (Figure 30c), to 1500 rpm (Figure 30d). This is also reflected in the interfacial area, which remains virtually constant up to 3200 rpm; only above 3200 rpm does the drop shape become

responsive to rotational speed, upon which the area vs. rpm data of the rateup experiment rapidly approaches those of the ratedown experiment. The hysteresis, i.e. the difference in drop shapes and in the drop area between Figure 30b and 7d, is due to the history of the sample, a situation commonly encountered in other jammed systems such as molecular glasses. The chief conclusion from this observation is that the jammed state requires a finite stress (in this case induced by centrifugal forces) to unjam and remobilize it. As in previous research, such hysteresis is likely attributable to interparticle attractions, either capillary in nature (considering the elongated shape of particles), or van der Waals. Some previous researchers[33, 65, 71] have reported that upon expansion, the monolayer cracked, and in the expanded monolayer 2D patches coexisted with particle-free bare interfaces. We have not noted cracking of the monolayers, at least at the ~50 μm scale resolution of our imaging.

Furthermore, we have also noted that the shape and the area of the jammed drop depends on the rate at which the interfacial area is reduced. This can be observed in a sudden stepdown experiment in which the F71 sample initially maintained at 6500 rpm was abruptly brought to 1500 rpm in about 5 s. A sequence of pictures captured during the decrease in rotational rate can be found in the supplementary materials online. Initially, the drop starts to retract from its ends as may be expected for a particle-free drop, but the retraction is interrupted by interfacial jamming. The jammed drop resulting from this sudden stepdown (Figure 30e) is significantly more elongated than the jammed drop realized from the gradual ratedown protocol (Figure 30b) at the same rpm. More quantitatively, the interfacial area from the sudden stepdown is about 5% higher than from a gradual ratedown experiment. The chief conclusion is that the specific interfacial area for jamming depends on the rate at which jamming is induced. Past experiments on 2D particle monolayers have sometimes noted a rate dependence of the surface pressure vs. surface area isotherms[30]; although some experiments have noted no rate dependence[33].

However, we believe this is the first report in which the specific interfacial area in the final jammed state itself depends on the rate at which jamming is induced. Nevertheless, this idea is well-established in the 3D jamming (i.e. glass formation) literature in which the specific volume of a glass depends on cooling rate.

4.3.4 Nonpolar/nonpolar system

There is significant interest in realizing bijels in polymeric systems, in which both phases are generally relatively non-polar[43, 72]. Accordingly, we have also conducted limited experiments on the same particles adsorbed at the interface between silicone oil and mineral oil – a situation representative of adsorption between non-polar phases. As mentioned in Section 4.2.2, the interfacial tension between the equilibrated phases is on the order of 1 mN/m, which is comparable to that for many polymer pairs. In preliminary experiments, we verified partial wettability of the particles between the silicone oil and mineral oil: the particles and the two oils were blended together in a Petri dish, and interfacial adsorption was clearly evident in optical images of the resulting emulsions.

Samples for SDT experiments were prepared identically to the glycol/oil case: particles were pre-dispersed in the mineral oil, and a drop of this dispersion suspended in silicone oil was spun in the SDT to induce interfacial adsorption. A difference was immediately evident; the particles showed significant aggregation at the interface and gentle shaking of the sample tube was not able to break these aggregates. Figure 31a shows an example of the results. A patch of high particle concentration is found to coexist with a particle-free "bare" region on the interface. The fact that the particles do not exert spreading pressure at the interface suggests that interparticle repulsions are weak. This is not surprising: since both phases have low polarity, the

82

particles are not expected to have significant charge, and hence electrostatic repulsion is likely to be absent. Accordingly, the interparticle attractions (likely capillary in nature given the non-spherical particle shape[20]) dominate, causing interfacial aggregation. It is also noteworthy that the particle loading in Figure 31a was adequate to cover the surface area of this drop (assuming the same specific interfacial area of 2.07 m^2/g estimated in the previous section). This clearly indicates either that some particles are adsorbed in an out-of-plane configuration, or are not adsorbed at the interface, but remain in the bulk. If the latter is true, the particles in the bulk are likely associated with those at the interface since gentle shaking of the tube did not increase the particle adsorption.
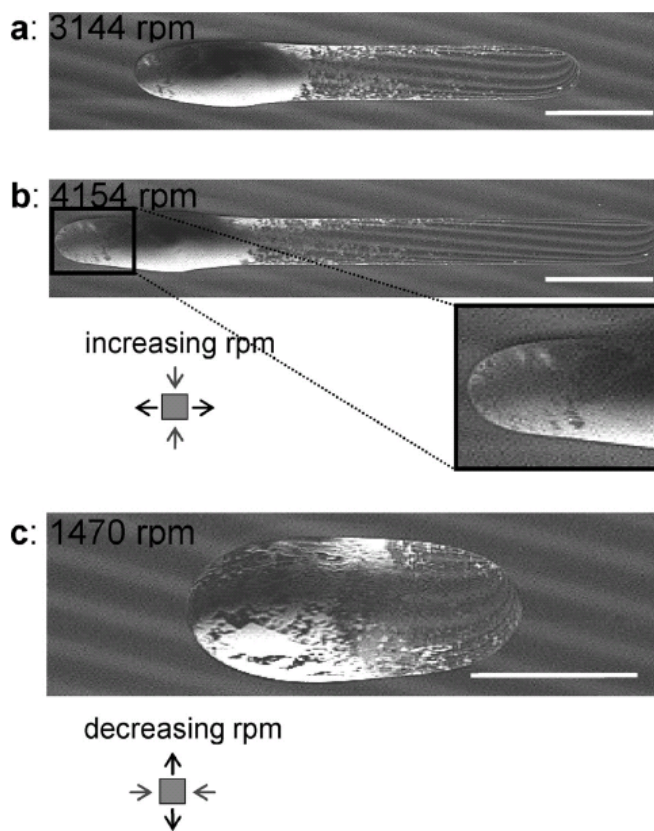
Figure 31. FeOOH particles at the mineral oil/silicone oil interface.

(a) particles adsorbed at the interface between mineral oil and silicone oil. (b) Same drop upon increasing rotational speed. (c) Same drop upon decreasing torational speed. Scale bars are 3 mm.

83

Upon changing the rotational rate, the attraction-dominated monolayer behaves significantly differently from the previous glycol/oil case. Increasing the rpm (Figure 31b) causes the bare portion of the interface to elongate unhindered, but the particle-covered patch extends only slightly with cracks developing perpendicular to the axial (stretching) direction. Correspondingly, decreasing the rpm causes drop retraction, with cracks appearing azimuthally, again perpendicular to the stretching direction. It is noteworthy that as the rpm is increased or decreased, the particle-free portion of the drop stretches and contracts as expected quite independently of the particle-covered patch.

4.4   CONCLUSIONS

We have examined interfacial particle jamming using a spinning drop tensiometer (SDT) for the first time. By reducing the rotational speed of the spinning drop, its interfacial area can be reduced in a controlled fashion. Since this decrease in interfacial area occurs due to capillary pressure, it is representative of the jamming process in bijels.

For FeOOH particle monolayers adsorbed at the oil/glycol interface, our experiments show that drops maintain a non-spherical shape when the particle coverage becomes sufficiently high; furthermore, elongaged drops are also stable against capillary instabilities. In contrast to past experiments using Langmuir troughs or a shrinking drop, interfacial buckling was not observed, and we believe that lack of buckling is a general feature of interfacial tension-driven jamming. Calculations indicate that the specific interfacial area for jamming is close to that expected for a tightly packed monolayer of particles. However, the specific interfacial area

varies by as much as 20% with changes in particle loading. Furthermore, there was significant hysteresis between compressing vs. expanding the jammed monolayer, which suggests that a certain minimum force is required for unjamming. Finally, rapid interfacial contraction led to a less tightly-packed monolayer in the jammed state, behavior similar to glass formation.

Finally, limited experiments on the same particles adsorbed at the interface between two non-polar liquids (mineral oil and silicone oil) show altogether different behavior. The particles do not spread at this interface, but instead form a high concentration jammed patch that coexists with a particle-free region of the interface. This suggests that interparticle repulsion is weak in this non-polar system and hence monolayer behavior is dominated by interparticle attraction.

5.0   BIJEL-STRUCTURED POLYMER BLEND

In this chapter, we demonstrate the application of interfacial particle jamming on controlling the morphology of a bicontinuous polymer blend. In Section 2.4, we have introduced bijels. They are composite materials with a bicontinuous structure, consisting of two fluid phases with the interface being jammed by particles. The goal of this chapter is to demonstrate an example of polymer bijels. A polymer melt system (low molecular weight PI and PIB) was chosen to highlight the effectiveness of interfacial jamming on arresting and stabilizing a bicontinuous morphology that would otherwise coarsen and phase separate with time. The formation of a bicontinuous polymer blend and the mixing sequence of particles with the two polymer components will be discussed. The detailed particle adsorption and transfer mechanism based on a thermodynamic argument will also be covered.

5.1   MATERIALS

FeOOH particles were used in this study (see details of the particles in Section 3.1). Polyisoprene (PI) and polyisobutylene (PIB) were the components of the polymer blend. Low molecular weight polymers were chosen as they were molten (i.e. viscous fluids) at room temperature, thus allowing flow experiments to be conducted at room temperature. The polymer components are nearly Newtonian liquids under experimental conditions and their viscosities

were measured at 25˚C by an AR2000 rheometer (TA Instruments, Inc.). The properties of all three components are listed in Table 5.

<p align="center">Table 5. Properties of components in the PI/PIB system.</p>

	Supplier	Cat.#	MW (g/mol)	Density [a] (g/cm^3)	Viscosity (Pa.s)
Polyisoprene (PI)	Kuraray Co, Ltd	LIR-30	29,000	0.910	131
Polyisobutylene (PIB)	Soltex Inc.	PB32	1,300	0.905	68.9
Iron oxyhydroxide (FeOOH)	Elementis Pigments Inc.	4088D	/	4.03	/

[a]. Quoted by manufacturer

5.2   METHODOLOGY AND CHARACTERIZATION

5.2.1   Generating bicontinuous morphologies

This molten PI/PIB polymer blend system is unique in that we found that mixing for a few minutes at a suitable composition range is sufficient to generate a bicontinuous morphology. Because hand blending can rarely generate a bicontinuous morphology, we speculate that a flow-induced mixing occurs during blending due to the partially miscibility and low molecular weights of the components, resulting in this unique behavior (see Section 2.3.2.1 for introduction to flow-induced mixing). In contrast, a particle-free PI/PDMS polymer blend gives a droplet-matrix morphology at all compositions (discussed in Section 6.4.1). Mixing was performed by hand-blending with a plastic spatula in a Petri dish typically for 5 min. The particle-free sample notations, the weight and volume compositions and the corresponding morphology are summarized in Table 6.

Table 6. Summarization of compositions and morphologies for particle-free samples

Sample designation	PI wt%	PI vol%	Morphology
PI20_blank	20	19.9	Droplet-matrix/bicontinuous coexist
PI30_blank	30	29.9	bicontinuous
PI40_blank	40	39.9	Droplet-matrix/bicontinuous coexist
PI50_blank	50	49.9	Droplet-matrix
PI70_blank	70	69.9	Droplet-matrix

PI30_blank gives a reliable bicontinuous morphology and therefore is chosen to be the composition of interest. The bicontinuous morphology generated by hand blending continuously evolves, and the domains coarsen with time while the bicontinuity is retained at the early stage. The morphology will completely turn into a droplet-matrix morphology after 9 hr in a Petri dish (see Figure 32d). Re-blending an evolved sample PI30_0 can restart the morphology evolution of the bicontinuous morphology for enormous times.
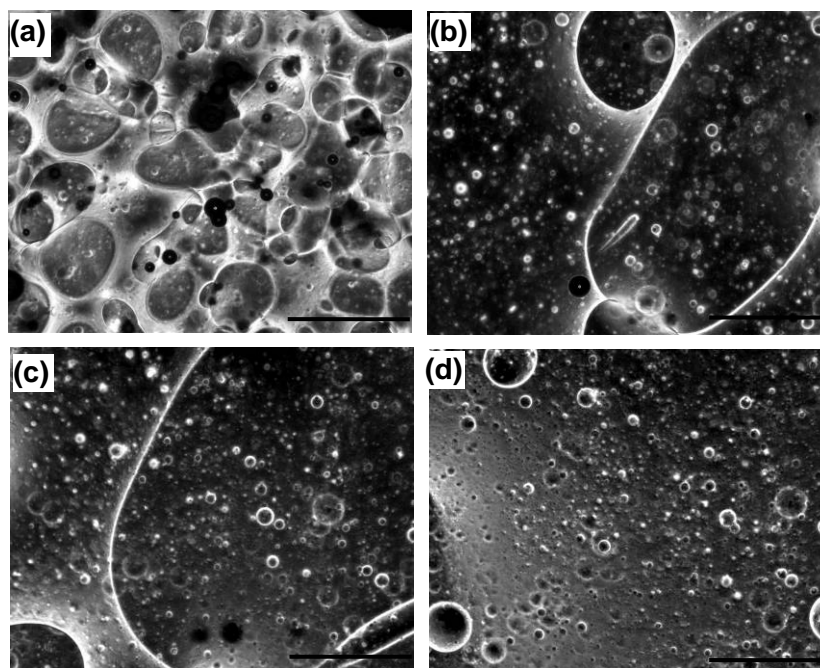
Figure 32. Morphology evolution for particle-free blend PI30_blank in a Petri dish.

(a)1hr (b) 3hr (c) 5hr (d) 9hr after hand-blending. Pictures were taken in a phase contrast mode to enhance contrast.

The scale bars are 500 μm.

Particle-containing samples were studied at the same polymer composition as PI30_blank. FeOOH particles were first mixed with one of the polymer components before adding the other polymer. The notation "PI30_Y1wtPI" designates one weight percent of FeOOH particle (Y for the yellow color) based on total polymer weight was added in PI component first, and the PI composition of the polymer portion is 30 wt%. For the reason of experimental convenience, samples are prepared based on weight. However, volume percentages are more relevant to the morphology formed. Therefore, the weight percentages are converted to volume percentages in Table 7.

Table 7. Weight percentage to volume percentage conversion of components

Sample designation	FeOOH wt%	FeOOH vol%	PI vol%	PIB vol%
PI30_blank	0	0	29.9	70.1
PI30_Y1wtPI	1	0.2	29.8	70.0
PI30_Y3wtPI	3	0.7	29.7	69.6
PI30_Y6wtPI	6	1.3	29.5	69.2
PI30_Y1wtPIB	1	0.2	29.8	70.0

5.2.2 Optical visualization for samples in a Petri dish

Samples were observed under an inverted optical microscope (Olympus Inc., CKX41) in the bright field mode. For particle-free samples, the refractive index difference of the two polymer phases is small, so phase contrast mode was sometimes used to improve image contrast. The typical sample thickness in a Petri dish is 1~2 mm. There are three drawbacks for this observation method: (a) it is not able to capture the initial status after blending (i.e. time= 0 sec)

as putting samples on microscope stage and adjusting focus takes tens of seconds; (b) hand blending makes sample uneven in thickness and flow of sample would slowly drift observation spot for tens of minutes and might affect the microstructure; (c) confinement effect would be different from that in a rheometer since one surface of sample is open to air. However, the image quality of sample in Petri Dishes is better than that in a shear cell (described below). The particle location can be resolved well to determine if the particles are at interface. Therefore, the interfacial activity of particles and particle distribution are primarily obtained by the Petri dish experiments. Long time observation such as 10 hr is possible with an automatic picturing program in Matlab program.

5.2.3   Optical visualization for blends in a shear cell

A strain controlled ARES rheometer (TA Instruments, Inc) was modified to create a home-built shear cell that can shear samples in a controlled way between two parallel glass plates at a desired gap to facilitate optical visualization. The purpose of shear cell visualization is to simulate the shear history of samples in a rheometer and therefore we can correlate the rheological data with visualization data to study the morphological development. We can also make sure that the simple shearing between plates can regenerate the bicontinuous morphology that we get from hand blending in a Petri dish. In addition, the three drawbacks of the Petri dish observation method do not exist. However, the image quality is not as good as that of inverted microscope mainly due to the thick glass plate and imperfect light source. The information we get mainly is the length scale of the morphology development in a confined geometry. The procedure of shear cell visualization is as following. Following two-minute hand blending in a Petri dish, a blend was degassed for 30 min under vacuum to remove air bubbles, and then a

portion of the blend was loaded between the parallel plates in the shear cell and squeezed to 150 μm in thickness. Three minute shearing at shear rate of 12 s^{-1} was performed, which corresponds to roughly 1000 Pa shear stress at the radius of 8 mm for PI30 composition.

5.2.4 Rheology of blends

Samples were prepared by hand blending FeOOH particle dispersion in PI component with PIB component for 2 min. The blend was degassed for 30 min under vacuum and loaded in the rheometer. The rheological measurements were carried out in a stress controlled rheometer (AR2000, TA Instruments Inc.) with a cone and plate geometry. The rotating part is a stainless steel cone with a cone angle of 1˚ and a diameter of 40 mm. Sample temperature was maintained at 25˚C with a Peltier plate. The blends were presheared at stress of 1000 Pa for 3 min, and then a series of dynamic frequency sweep at 10% strain were performed. The purpose of preshearing is to regenerate the bicontinuous morphology, if applicable. Dynamic frequency sweeps are conducted to probe the morphology and its development with time for a total duration of 9 hr. The first five sweeps take 6 min each for frequency 100~0.1 rad/s. The next ten sweeps take 21 min each for frequency 100~0.0398 rad/s. The last five sweeps take 1 hr each for frequency 100~0.01 rad/s.

5.3   RESULTS

5.3.1   Morphology and particle distribution

To recognize the 3D bicontinuous morphology from 2D microscopic images, we can change the focus planes to trace each of the two phases.   There are three helpful judgments for a bicontinuous morphology.   Firstly, fluid channel in the form of connecting "necks" and "junctions" of uneven curvature are typical for a bicontinuous morphology.   Secondly, as a reverse judgment, in a droplet-matrix morphology, every object has a closed shape, typically spherical or ellipsoid. If we observe many open outline of object on a single focus plane, it is likely to be a bicontinuous morphology.   Thirdly, as a relative judgment, the domain size growth of a bicontinuous morphology is much faster than that of a droplet-matrix morphology due to different growth mechanisms.   Figure 33 shows the morphology of two particle-free samples, PI50_blank and PI30_blank at 10 min after mixing in a Petri dish. The former is of droplet-matrix morphology and the later is of bicontinuous morphology.   In Figure 33a, most of the drops remain small since only the occasion drop coalescence can make drops grow in size. In Figure 33b, while the initial domain size was comparable to that in Figure 33a, the domain size at 10 min later has increased dramatically.
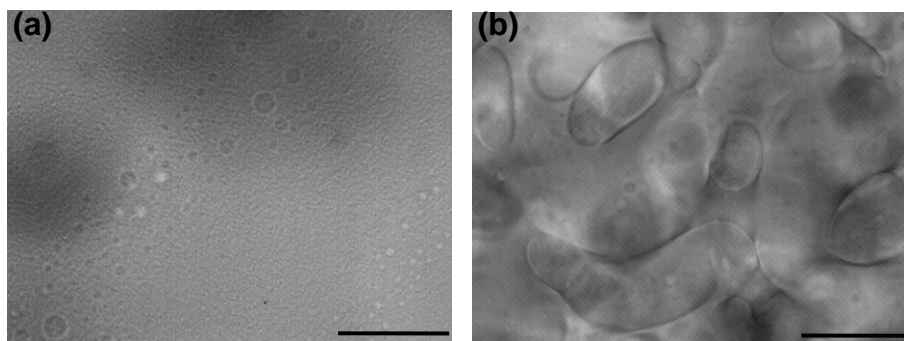
Figure 33. A comparison of PI50_blank (droplet-matrix) and PI30_blank (bicontinuous) at 10 min after the hand-

blending.

(a) Particle-free sample PI50_blank shows a droplet-matrix morphology whose drops barely grow in 10 min.

(b)Particle-free sample PI30_blank shows a bicontinuous morphology whose domain size increased dramatically

within 10 min. The Scale bar is 50 μm

For particle-containing samples, particle distribution is not homogenous. Immediately after mixing, one of the phases appears darker in color which implies either the surface is coated with particles and/or it contains more particles inside the darker phase. Figure 34 shows micrographs at several focus planes of sample PI30_Y3wtPI to reveal the bicontinuous morphology.
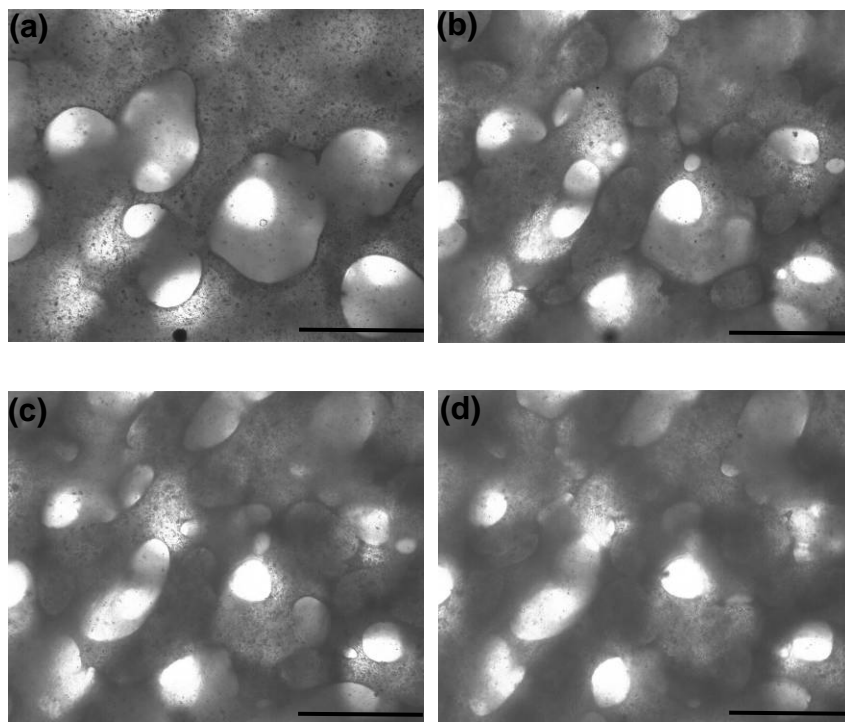
Figure 34. Micrographs at different focal planes to show the bicontinuous structure. As the height of four different focal planes increases from (a) to (d), different portions of sample PI30_Y3wtPI at 26 min after mixing come into focus, showing the bicontinuous morphology. The Scale bar is 100 μm.

For samples in which particles are initially dispersed in the PI component, in a few minutes, the boundary of the two phases is decorated with particles, forming a distinct dark line (see both Figure 34 and 35a). This is evident that some particles are adsorbed at the interface. However, for samples in which particles are initially dispersed in the PIB component, at the early stage of phase separation (a few minutes), no particle or little particles are at the boundary of phases. The initial location of particles (i.e. mixing procedure) seems to be crucial. Figure 35 contrasts the difference between PI30_Y1wtPI and PI30_Y1wtPIB.

94
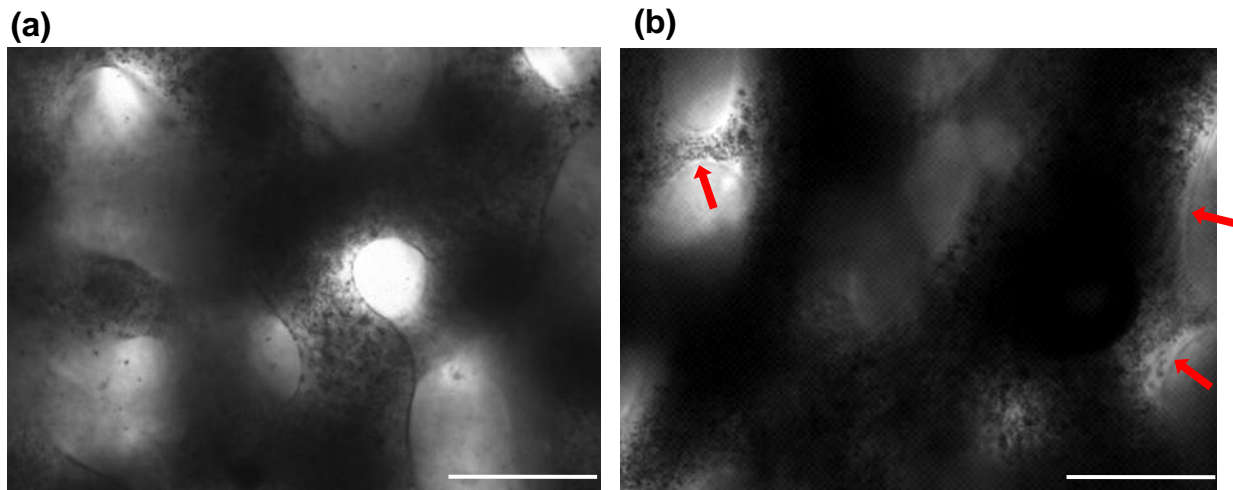
Figure 35. Different appearance of phase boundary lines for particle-containing PI/PIB blends of different mixing procedures.

(a) PI30_Y1wtPI. Phase boundary lines appear darker due to the adsorbed particles. (b) PI30_Y1wtPIB. Phase boundary lines appear clear in color, which suggests little or no particles are adsorbed at interface. The arrows point at examples of the colorless polymer-polymer interface. The Scale bar is 50 μm.

It is suspected that particles interact with the bulk phase differently which may results in the observation above. We therefore investigated the particle dispersion in PI or PIB component. As shown in Figure 36, particles form homogeneous dispersion in PIB component (Figure 36a), but they associate with each other in PI component to form chain-like structure (Figure 36b) under influence of flow, or dendritic structure under quiescent condition (Figure 36d). The particle-particle interaction is preferred over particle-PI polymer chain, and particle-PIB polymer chain interaction is preferred or equal to particle-particle interaction. Therefore, particle-PIB interaction is more favorable as compared to particle-PI interaction.
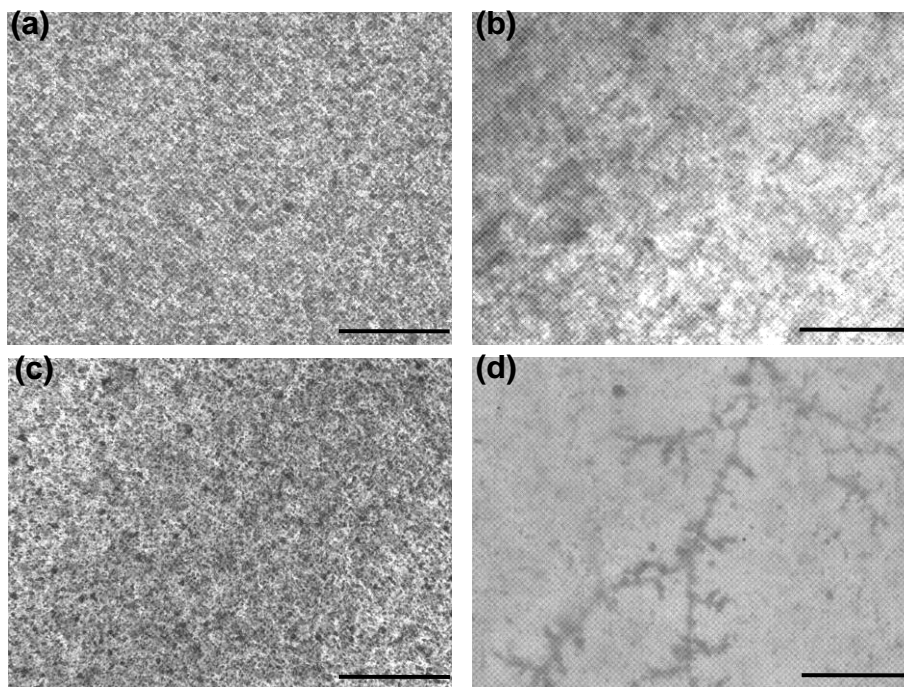
Figure 36. The homogenous particle-PIB dispersion and the aggregated structures in particle-PI dispersions. (a) Particle-PIB dispersion of 6 wt% is homogeneous and structureless. (b) Particles in PI associate into chain-like structure under the influence of flow in the particle-PI dispersion of 6 wt%. (c) As mixed, the particle-PI dispersion of 3.2 wt% is homogeneous. (d) Under quiescent conditions for three day, the particle-PI dispersion of 3.2 wt% contains dendritic structures. The scale bars are 50 μm.

If particles have preferred interaction with PIB component, as we put particle initially in PI component, we expect that particles would transfer into the other phase during a mixing process, if not sequestered by interface. In fact, even without blending, particles can leak out from PI phase into PIB phase at the moderate flow as samples level under gravity in a Petri dish (see Figure 37). We attributed this leaking mainly to the mutual solubility near the interface. During this process, particles appear to be at the interface either temporarily or kinetically trapped at the interface. We will discuss more in Section 5.4.1 on the particle transfer mechanism.

96
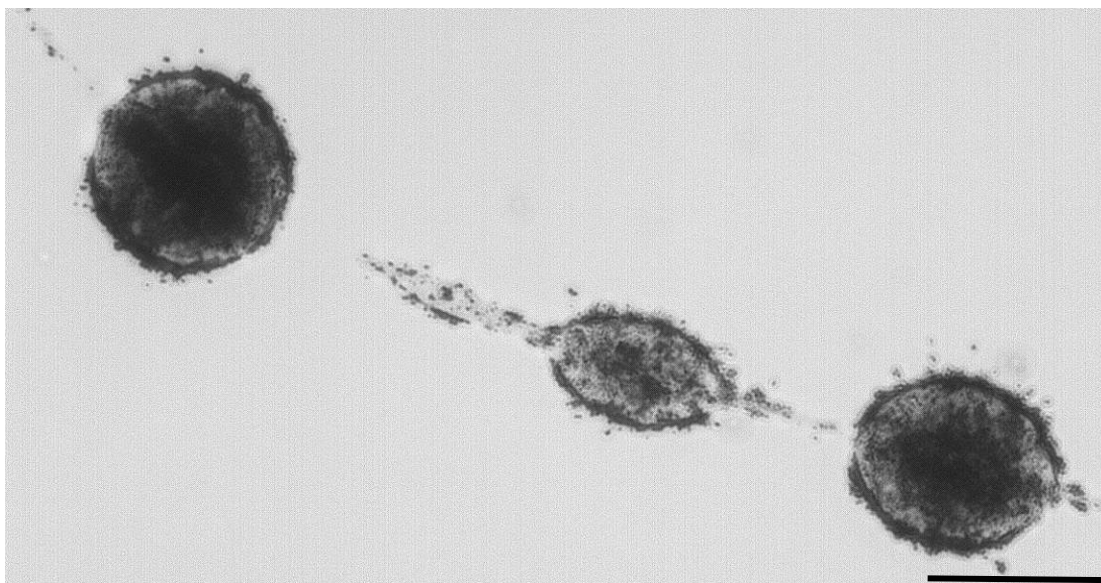
Figure 37. FeOOH particles leak out from PI drops into PIB phase before blending.

The Scale bar is 50 μm.

Since particles prefer PIB phase, we presumed the darker phase in Figure 34 and Figure 35 was PIB phase, knowing that not all of the particles reside at the interface. To experimentally determine the dark phase, we put a small lump of pure PIB or PI, and lay the blend sample PI30_Y1wtPI on top of the pure component. As shown in Figure 38a, a sharp interface formed between the pure PI lump and the dark phase, indicating they were chemically different. In Figure 38b, there is no obvious interface between pure PIB and the dark phase, and particles diffused from the dark phase into pure PIB. We therefore concluded the darker phase is PIB and the lighter or transparent phase is PI.
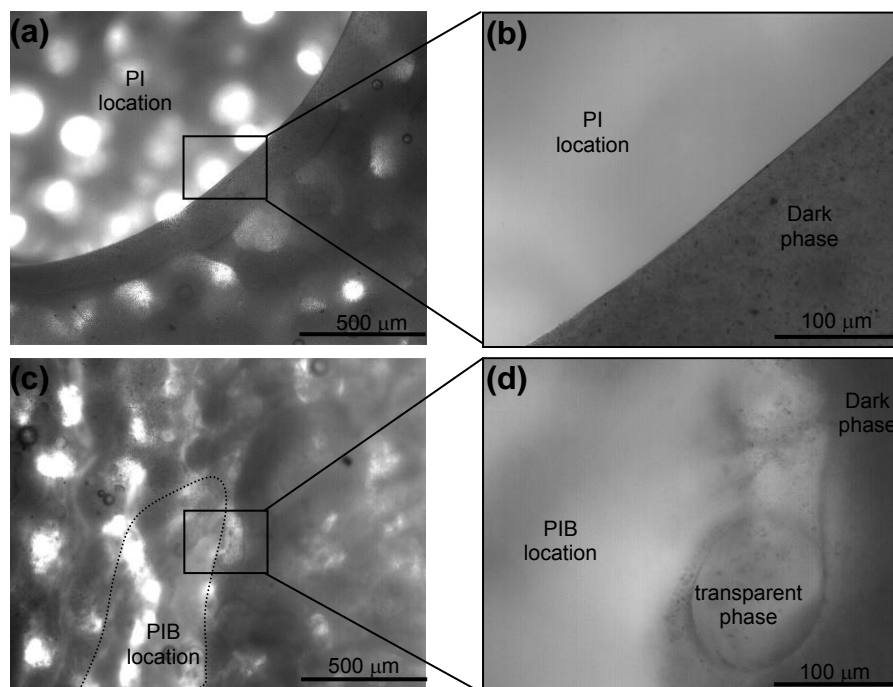
Figure 38. Experiments to test the phase of the dark region by contacting with pure PI or PIB components. (a) A circular lump of pure PI is in contact with the blend PI30_Y1wtPI. The interface formed indicates that dark phase is chemically different from PI. (b) Magnified micrograph of the denoted area. (c) An irregular-shaped lump of pure PIB is in contact with the blend PI30_Y1wtPI. Dotted line shows the location of PIB. (d) Magnified micrograph of the denoted area. Particles from dark phase diffuse into pure PIB.

5.3.2   Effect of particle jamming on morphology development

The morphology development of samples with different particle loadings is compared in this section. As we increase particle loading, both the bulk effect and interfacial effect may affect the morphology development. On the bulk effect, the particles inside the phases can increase viscosity and moduli of polymer and therefore slow down the phase evolution. On the interfacial effect, as the interfacial area decreases with morphological coarsening, interfacially adsorbed particles can jam the interface and thus retard the morphology development. We are primarily

interested in the later effect, so we keep the particle loading low as the bulk effect is only expected to be important when the particles occupy several percents by volume. This issue will be discussed further in later this section after we show the comparison of morphology development. In Figure 39, the morphology development of PI30_blank, PI30_Y1wtPI, PI30_Y3wtPI and PI30_Y6wtPI is compared together in two successive pages.

In Figure 39a, e, i and m, the initial morphology in a Petri dish immediately after mixing has a length scale of about 3 μm. The actual domain size is unknown as visualization is limited by the resolution of optical microscopy. The domain size should be determined by shear stress applied during hand blending. Figure 39b, f, j and n show the morphologies for different samples at 10 min after mixing. The domain sizes are comparable to each other. The dark particle lines in Figure 39f, j and n suggest particle adsorption at interface, as there was no lineup of particles along the polymer-polymer interface if particles were initially dispersed in PIB phase (see Figure 35). Particle jamming has not yet been effective to slow down the morphology development at t=10 min. Figure 39c, g, k and o show the morphologies at 30 min after mixing. Note the scale bar of 5-7k is different from others, so an inset of 5-7k with 250 μm width is provided for easy comparison. At t=30 min, the domain sizes of PI30_Y3wtPI and PI30_Y6wtPI are obviously smaller than that of PI30_blank and PI30_Y1wtPI. Increasing particle loading does slow down the morphology development and therefore yields a smaller phase size at later stages during coarsening.

Figure 39d, h, l and p show the morphologies at 60 min after mixing. Again, the inset of Figure 39l is 250 μm in width. From time=30 min to time=60 min, the domain sizes for PI30_Y3wtPI and PI30_Y6wtPI did not grow much, while the growth for PI30_blank and PI30_Y1wtPI were apparent.
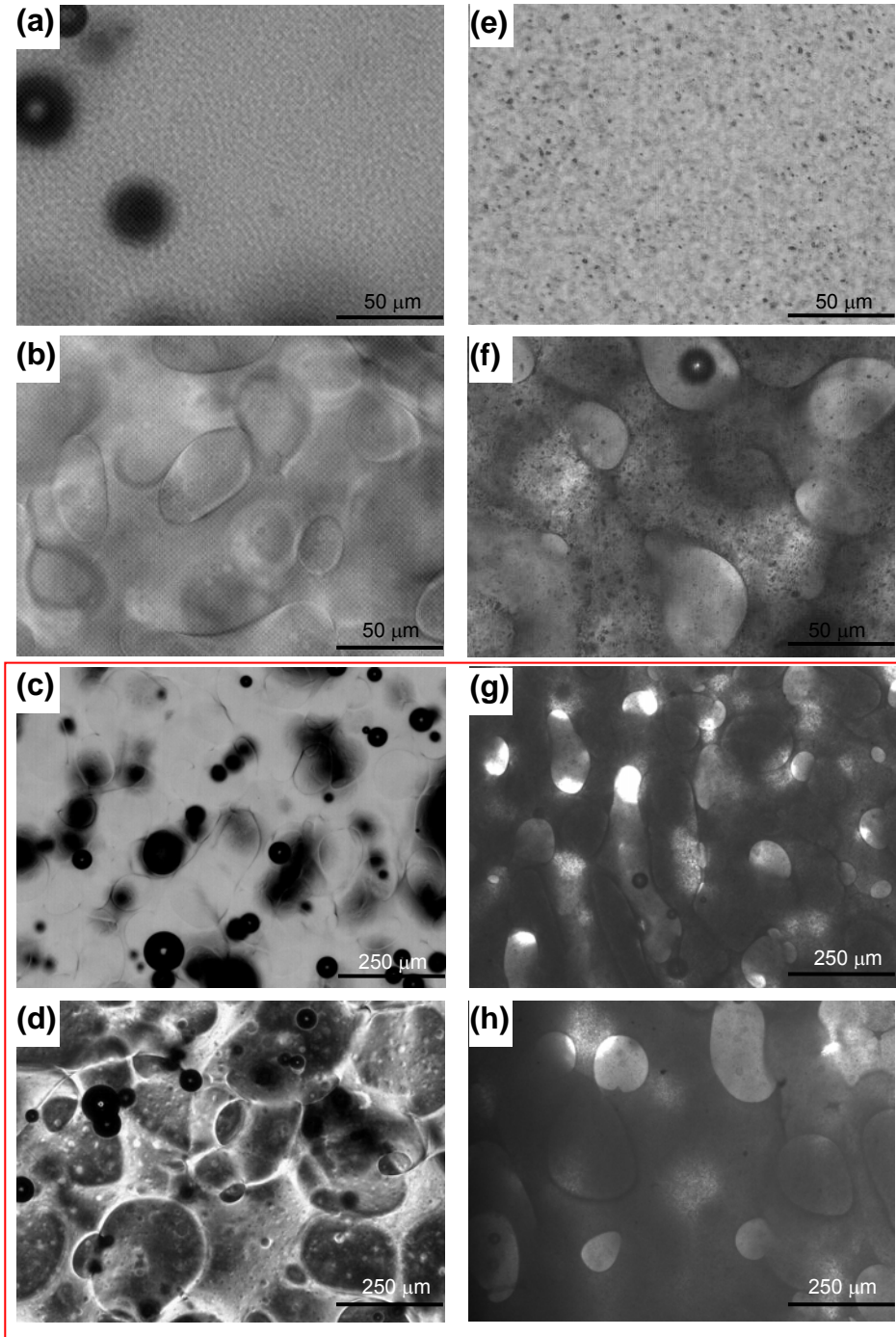
Figure 39. Morphology development for PI30_blank and PI30_Y1wtPI. (page 1st of a two-page comparison)

(a-d) PI30_blank and (e-h) PI30_Y1wtPI at four different observation times, which are t=0 min, t=10 min, t=30 min

and t=60 min after mixing in a Petri dish. Figure d is a micrograph in phase-contrast mode. The scale bar for figures

a, b, e and f is 50 μm. The scale bar for figures c, d, g and h is 250 μm. The red rectangle circles the micrographs

with the same scale bar.

100
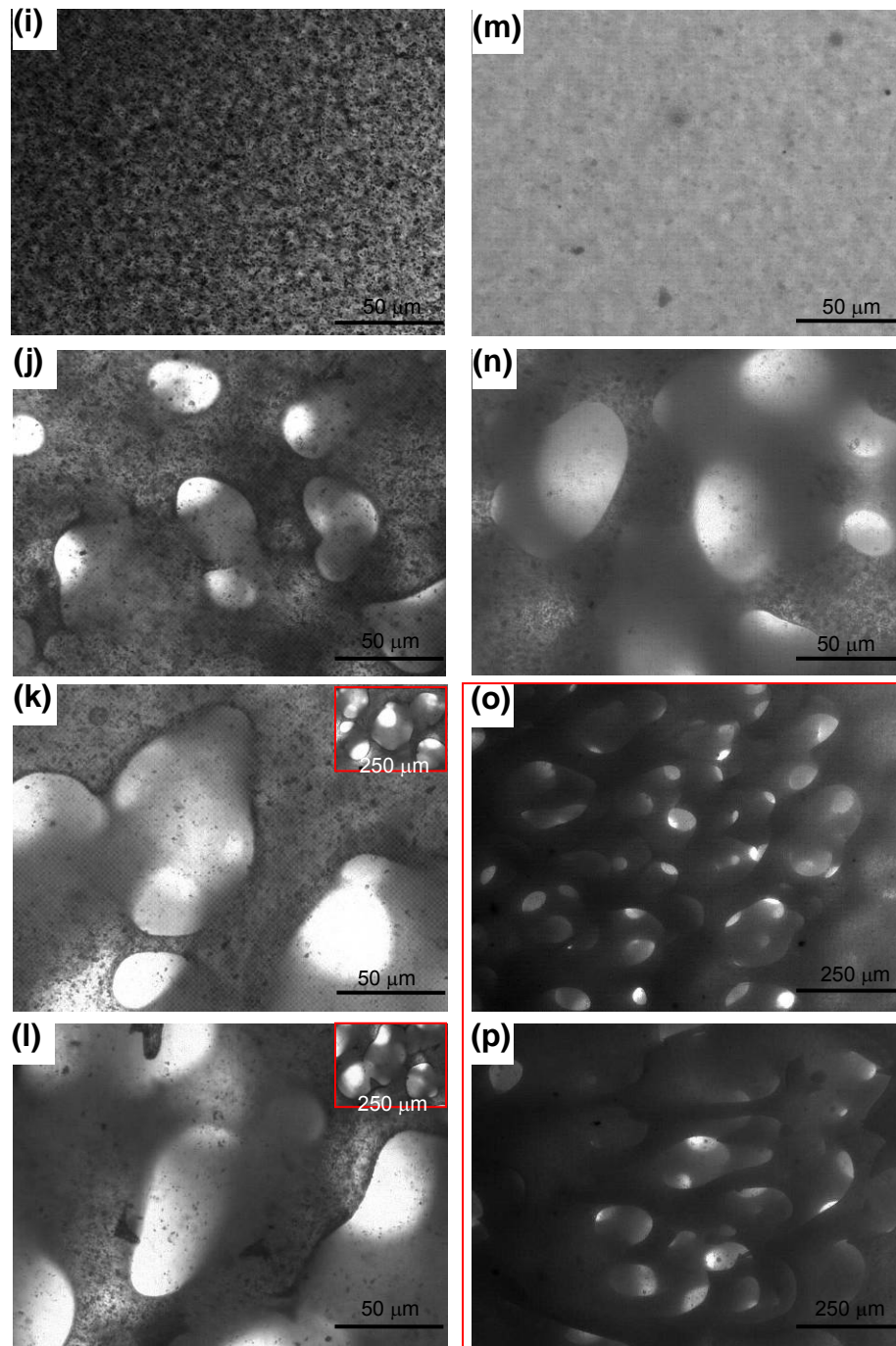
Figure 39. Morphology development for PI30_Y3wtPI and PI30_Y6wtPI. (page 2ⁿᵈ of a two-page comparison)

(i-l) PI30_Y3wtPI and (m-p) PI30_Y6wtPI at four different observation times, which are t=0 min, t=10 min, t=30 min and t=60 min after mixing in a Petri dish. The scale bar for figures i, j, k, l, m and n is 50 μm. The scale bar for figures o and p is 250 μm. The inset of k and inset of l is 250 μm in width.

101

The morphology stabilization was most convincing as we compare the appearance in a Petri dish directly at a time of over 20 hr after mixing. The particle-free sample PI30_blank is transparent. Its picture contains no information of morphology, therefore not shown here. Instead, in Figure 40, we compare PI30_Y1wtPIB (i.e. particles initially dispersed in PIB component) with PI30_Y1wtPI, PI30_Y3wtPI and PI30_Y6wtPIB to highlight how effective the morphology stabilization is by putting FeOOH particles into the PI/PIB blend. In all pictures in Figure 40, the width of pictures roughly matches the Petri dish diameter, 35 mm.

From the topview of the Petri dish, PI30_Y1wtPIB at time=21 hr has lost its bicontinuous morphology. The mutually distributed yellow region and transparent region (darker in color in Figure 40) reveal slightly that it has even been bicontinuous. The sideview of PI30_Y1wtPIB is nearly a two-layer structure. Note that there is a curved line as pointed by the (red) arrow, which is the interface between the top and bottom layer. The top layer appears yellow in color and presumably contains a significant amount of particles and it was confirmed to be PIB. The top layer occasionally has pillars connecting to the Petri dish surface (see Figure 40i). The bottom phase is transparent (still yellow in picture due to the background) but contains some particle-containing yellow drops. Some of the drops are suspended in bottom layer fluid and some sticks to the dish. Putting particles in the PIB component before mixing with the other component is not helpful in stabilizing the bicontinuous structure at the current particle loading (1 wt%).

In contrast, the topviews of PI30_Y1wtPI at time=20.5 hr, PI30_Y3wtPI at time=23.5 hr, and PI30_Y6wtPI at time=21 hr show a bicontinuous structure of mm-sized or sub-mm sized domains. The sideviews (insets of Figure 40f, g and h) show the sponge-like structure. The PIB phase appears yellow because it contains particles and is coated with particles at the surface. The PI phase contains little particles and is transparent; it appears as holes (darker in color) in the sideviews (Figure 40f, g and h). As the particle loading increases, the stabilized morphology at

~20 hr has smaller domain size. This is consistent with our expectation: particle loading determines the characteristic length scale of the arrested structures for bijels.

All of the topview, sideview and bottomview pictures for PI30_Y1wtPI, PI30_Y3wtPI and PI30_Y6wtPI show small domain sizes and bicontinuous structure, we therefore presume that the bicontinuous structure dominates throughout the whole sample for PI30_Y1wtPI, PI30_Y3wtPI and PI30_Y6wtPI. Dispersing particles first in PI component efficiently slows down and stabilizes the morphology development of the bicontinuous morphology for the current system. At the later stage of phase separation (~21 hr), the stabilizing effect is obvious even at a low particle loading of 1 wt% based on the total weight of polymer.
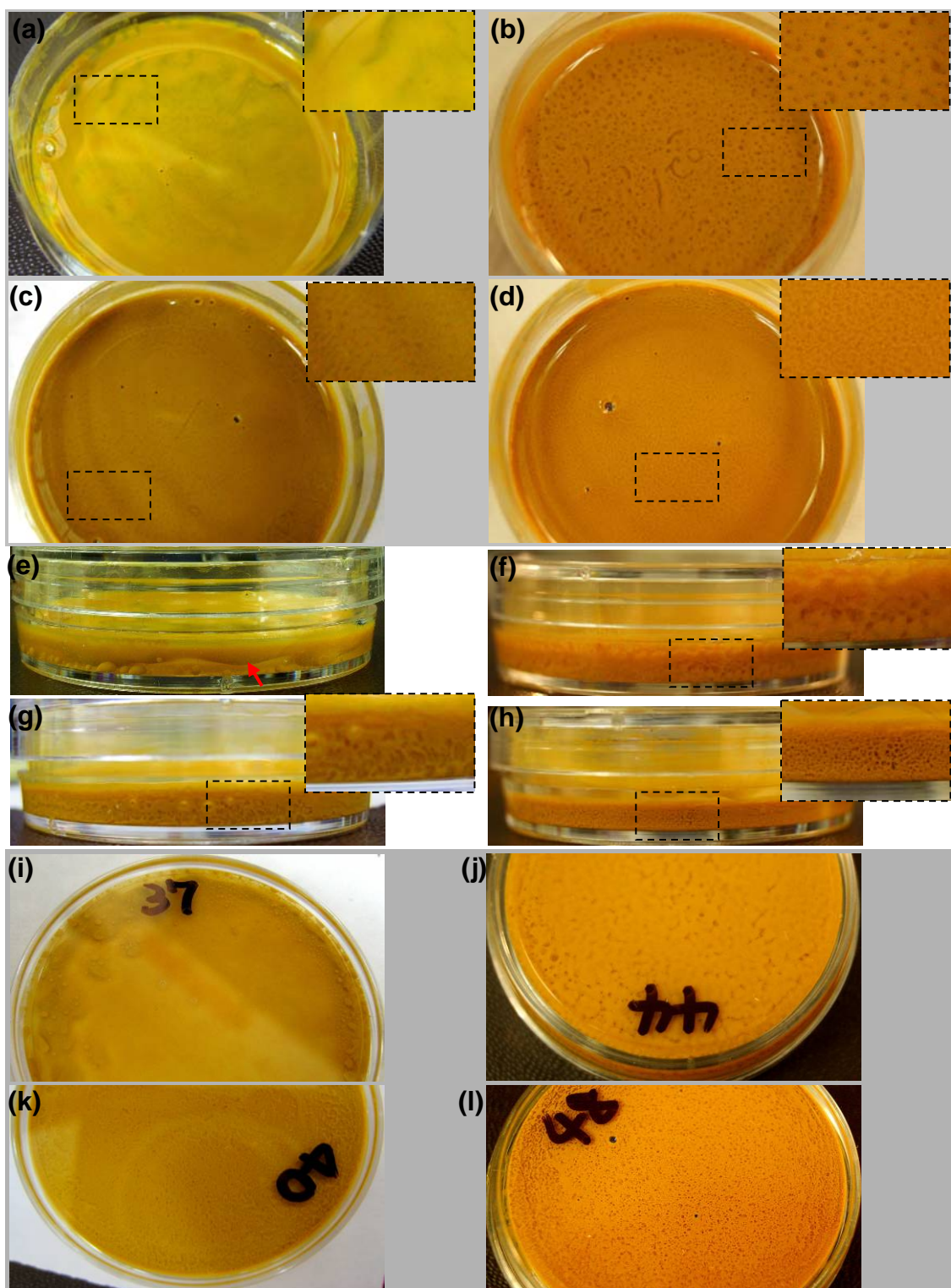
Figure 40. Pictures of particle-containing PI/PIB blends in Petri dishes.

Topview (a-d), sideview (e-h) and bottomview (i-l) for four particle-containing blends in Petri dishes are shown.

(a)(e)(i)PI30_Y1wtPIB; (b)(f)(j)PI30_Y1wtPI ; (c)(g)(k)PI30_Y3wtPI; (d)(h)(i)PI30_Y6wtPI

So far, we established that particles do have effect on the morphology stabilization, i.e. they dramatically slow down the phase separation of a bicontinuous polymer blend. Also, we have mentioned above that there are two possible effects that can slow down the morphology development, which are the bulk effect and interfacial effect. To exclude the contribution of bulk effect, we investigate the bulk rheology of the particle dispersions and compare it to the corresponding polymer components.

Table 8 lists the steady-state viscosity for pure components and particle dispersions. For the 6 wt% particle-PIB dispersion, the viscosities (measured at 200 Pa and 1000 Pa stress) is higher than that of pure PIB by 10%, but the particle dispersion do not show shear thinning behavior. In contrast, the 6 wt% particle-PI dispersion does show shear thinning behavior.

Table 8. Steady-state viscosity for pure components and their 6wt% particle dispersions.

	Steady-state viscosity@ 200 Pa	Steady-state viscosity@ 1000 Pa
PIB	69	69
6wt% particle-PIB dispersion	76	76
PI	131	131
6wt% particle-PI dispersion	178	158

Dynamic oscillatory behaviors were also measured and were shown in Figure 41. Figure 41a shows that the loss modulus curve (G") for particle-PIB dispersion overlaps with that of pure PIB. The storage modulus curve (G') for particle-PIB dispersion overlaps with that of pure PIB at the high frequency region (10-100 rad/s), and then deviates at low frequency. This deviation at low frequency should be ignored because the ratio G"/G' is over 100, which implies the measurement is less reliable. The complex viscosity curve for particle dispersion is only higher

in values, but do not change the trend. The increased viscosity is expected as we also see in the steady-state viscosity measurement. In short, these measurements show that the particle-PIB dispersion is Newtonian and does not display viscoelasticity.

In contrast, the 6 wt% particle-PI dispersion behaves differently under oscillatory as shown in Figure 41b. The dispersion has higher G' modulus, and the complex viscosity has a decreasing trend and is not flat at low frequencies. All of these suggest that the dispersion is not Newtonian and the 6 wt% particle-PI dispersion has a shear thinning behavior. This shear thinning behavior is supported by the observation that FeOOH particles can associate with each other in bulk PI phase (see Figure 36). Continuous shearing at a higher stress may break more particle-associated agglomeration and thus result in lower viscosity.
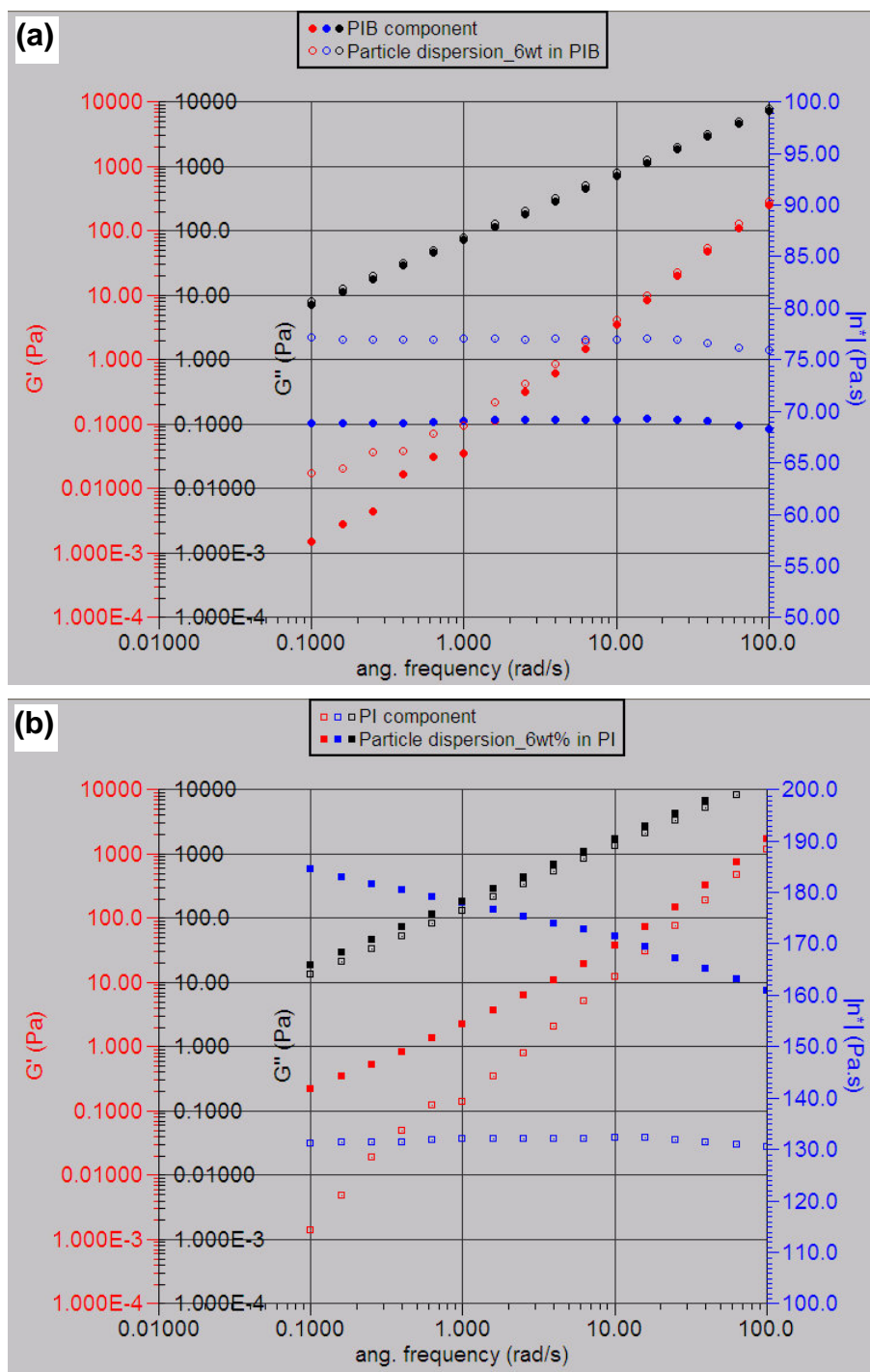
Figure 41. Dynamic oscillatory measurements for pure components, 6 wt% particle-PIB dispersion and 6 wt%

particle-PI dispersion.

(a) PIB and its 6 wt% particle dispersion. (b) PI and its 6 wt% particle dispersion.

The non-Newtonian behavior of a bulk phase is expected to retard the morphology development. However, from Section 5.3.1, we know that FeOOH particles have preferred interaction with PIB component. The particle-containing and thus darker phase is PIB-rich phase. Therefore, among the two particle dispersions (in PIB or in PI), the particle dispersion in PIB is actually more relevant to the bulk effect of the current system. The microscopic observation show that the PI phase is almost clear in color, and thus we presume that the particles left in PI phase should be much less than 1 wt%. At 1 wt% of concentration, the particle-PI dispersion will remain to be Newtonian (more detail shown in chapter 6, Section 6.4.2, Figure 79). Based on the two experimental findings: (1) particle-PIB dispersion is Newtonian at least up to 6wt%; (2) microscopy suggests little particles are left in the PI phase, we therefore believe that the stabilization effect of particles cannot be cause by the bulk effect alone and the bulk effect should be small. Thus, we believe that the interfacial effect is dominantly responsible for the morphology stabilization by adding FeOOH particles. The phase coarsening rate of the bicontinuous structure did not seem to be affected at the early stage of morphology development (see Figure 39b, f, j and n), but at the later stage, the morphology is almost fully arrested. This is also supportive for our hypothesis (i.e. stabilization is due to interfacial jamming) because the interfacial particle concentration may be low at the beginning of morphology evolution and jamming is unlikely to occur. We therefore conclude that interfacial particle jamming should be the main cause of the dramatic slowdown of morphology development and the ultimate stabilization at a relatively long time (over 20 hr). In addition, for the current system, FeOOH particles in PI/PIB blend, particle adsorption to the interface is only effective if particles initiate from the PI component (i.e. mix particles with PI first). Mixing procedure is not trivial for particle adsorption purpose. We will discuss the possible particle transfer and adsorption mechanism in Section 5.4.1.

5.3.3   Correlation between rheology and morphology development in a confined space between plates

Hand blending provides effective mixing for polymer melts. By hand blending, the current system gives a reliable but evolving bicontinuous structure that can be reset upon remixing. The mixing unavoidably incorporates air bubbles into the samples. Rheological measurements have to be performed on bubble-free samples. During the 30-minute vacuum degas time, the domains keep coarsening. The stress applied and the squeezing during sample loading may also affect the bicontinuous morphology. In the experiments, we used shearing between two surfaces (cone and flat plate) in a creep step to reset the bicontinuous structure. Therefore, one necessary task is to make sure that if the simple shearing can indeed provide proper mixing as the hand blending does, and result in bicontinuous morphologies. For that, we need optical visualization in the shear cell. We will also use information from the optical visualization and try to explain the newly-obtained rheological data for the current system.

To study the morphology development for a bicontinuous system, our first task is to get baseline knowledge for the well-studied droplet-matrix morphology. Droplet-matrix morphology is well-known to have a shoulder in the storage modulus vs. frequency curve. The position of the shoulder with respect to frequency is an indication of drop relaxation time. Figure 42 shows the oscillatory measurement for PI70_blank, which has been confirmed to have droplet-matrix morphology.

The (red) open circles are for the storage modulus (G') measurement immediately after a creep step of 1000 Pa for 3 min. The (black) open squares are for the G' at 8 hours after the creep step under sequential dynamic oscillations of 10% strain in the time between. The small-amplitude dynamic oscillation theoretically does not affect the morphology but is the tool to

probe the morphology. The shoulder of storage modulus at 8 hr very slightly moved to the left of the initial shoulder (from roughly 2.1 rad/s to 1.3 rad/s), indicating a negligible degree of drop size growth.   This is expected because under this quasi-quiescent condition (with small-amplitude oscillatory), drop coalescence event is only caused by gravity-induced drop motion, which is negligible. Thus, the drop can only grow by the Ostwald ripening, which should be limited by the mutual solubility of this partially miscible polymer blend system. The complex viscosity curve shifts to the left, which also indicates some degree of drop growth.
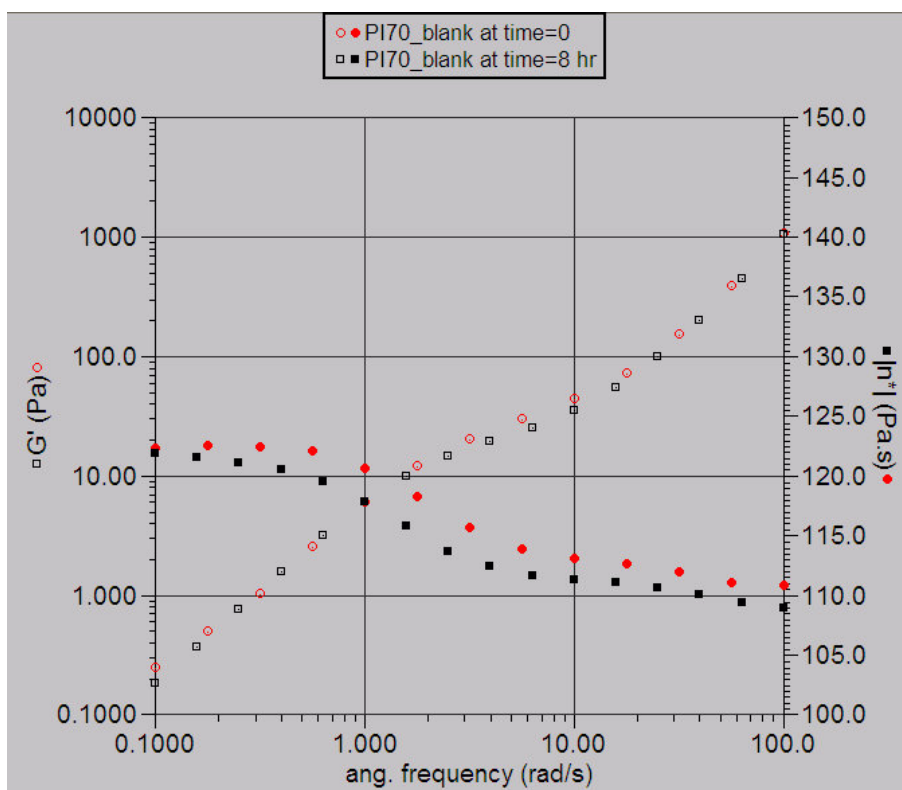
Figure 42. Dynamic oscillatory measurement for PI70_blank at time=0 min and 8 hr under quasi-quiescent conditions.

Below, we will discuss the main content of this section, which is the correlation between rheological data and morphology development for a bicontinuous morphology. We study both

110

the particle-free and several particle-containing samples. The time evolution of the storage modulus curve for the particle-free blend will firstly be presented. We then compare the difference between samples of different particle loadings and mixing procedure, if any. Further, we provide the visualization evidence that simple shearing between plates can indeed reset the bicontinuous morphology. We then try to explain the rheological data based on the information from visualization. The surface wetting effect in the confined space between plates will be discussed.

In contrast to the droplet-matrix sample PI70_blank, Figure 43 shows a different trend of the storage modulus (G') curve for PI30_blank. As mentioned in the methodology, a preshearing step was used to reset the morphology evolution.   The moment when the preshearing step finishes is taken as time=0 in the following. The G' curve immediately after the preshearing (measured by the first oscillatory step that begins at time=0) shows no shoulder but a single elbow point around 15 rad/s where G' at lower frequency starts to deviate from the component contribution. We presumed that the straight line at middle to low frequency after the elbow point is the characteristic of the bicontinuous morphology for the current system. A straight line in the log-log plot indicates a power scaling relationship. Vinckier and Laun[73] also showed a similar power law behavior at low frequencies (G'~ω^{α} with α<1) on a different polymer blend system (PαMSAN/PMMA). The direct evidence has to come from visualization (described below). As time proceeds to one hour after the preshearing (time=1 hr), a shoulder of G' curve develops in an incomplete way, i.e. the low frequency part of G' curve does not change its curvature. The G' curve of time=8 hr shows a similar trend with a bigger concave that moves slightly to the left. All other oscillatory G' measurements (not shown) lie in between the first oscillatory (t=0) and the last one (t=8 hr) with a continuous trend.
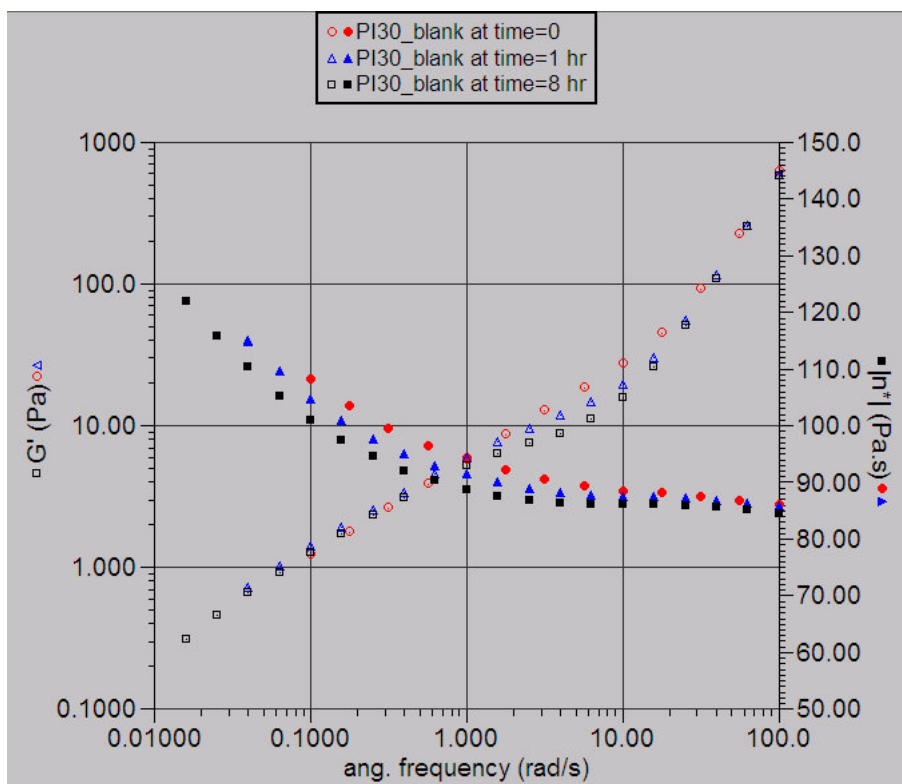
Figure 43. Dynamic oscillatory measurement for PI30_blank at time=0 min, 1 hr and 8 hr under quasi-quiescent conditions.

Figure 44a shows the storage modulus and complex viscosity curves at time=0 for five different samples, including PI30_blank, PI30_Y1wtPIB, PI30_Y1wtPI, PI30_Y3wtPI, and PI30_Y6wtPIB. All of the particle-containing G' curves are straight at middle to low frequencies, just like the particle-free sample PI30_blank. This suggests that the initial morphologies after preshearing for different samples were the same. PI30_Y6wtPI and PI30_Y3wtPI have higher complex viscosity over the entire frequency range, maybe due to the bulk effect. In Figure 44b, 45a and 45b, we show the G' curves for time $\cong$ 0.5 hr, 1 hr and 8hr. Although the curves evolve from time=30 min to time=8 hr, the curves between different samples lay close to each other. Because we know that the morphology development was highly affected by the added particles as shown in Section 5.3.2, this was unexpected that there is no

dramatic difference in rheology. The possible reasons will be discussed after we show the visualization data. The G' value of PI30_Y6wtPI is slightly higher in the middle frequency at all time, but lower at the low frequency region. A bulk contribution due to the higher particle loading should make the G' value higher throughout the frequency range. Therefore, we believe that the slight difference in G' value reflects the morphology development difference for PI30_Y6wtPI. However, this difference is much smaller than what we expect based on the Petri dish observation (Figure 40).
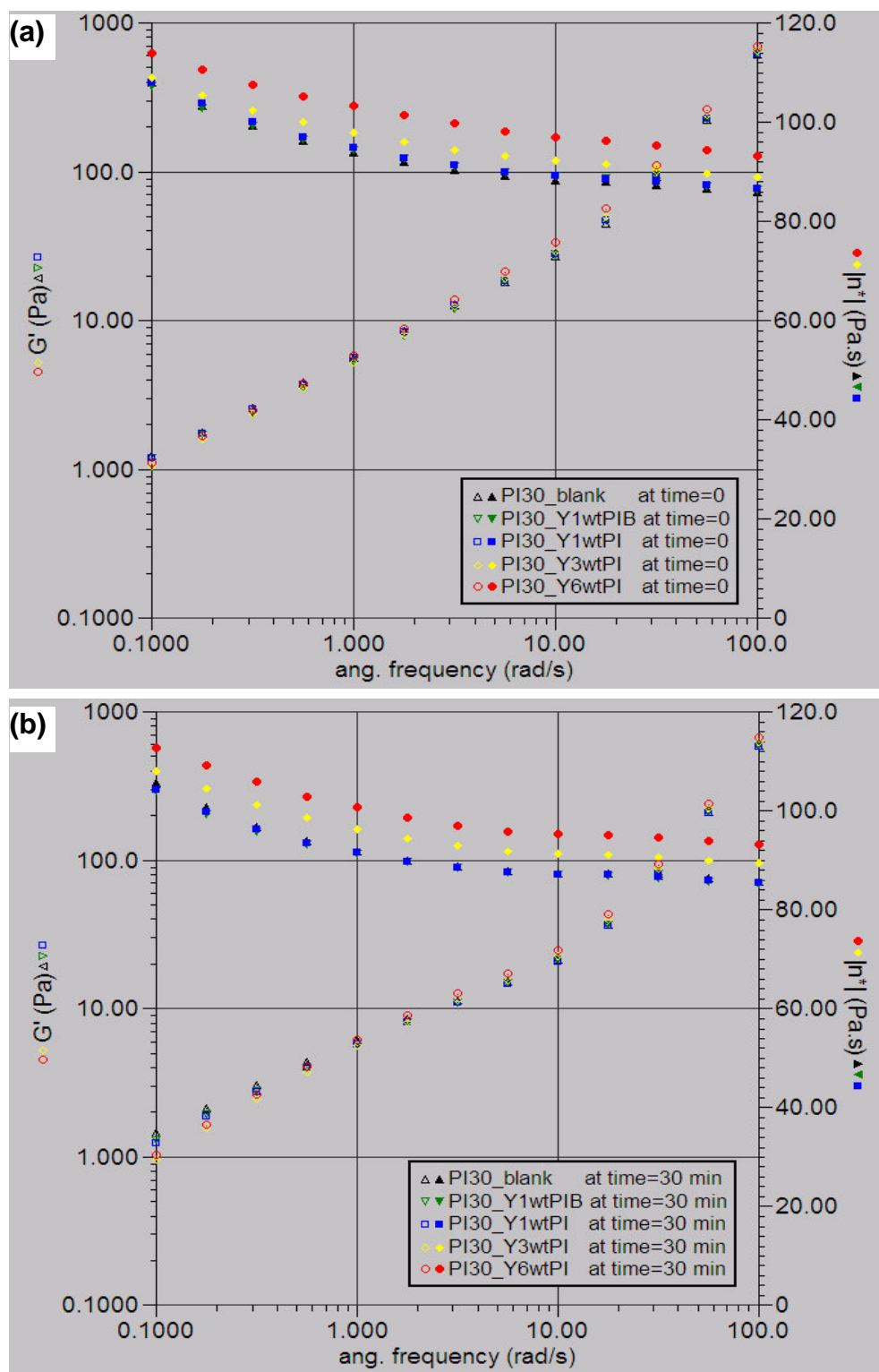
Figure 44. Dynamic oscillatory behaviors for particle-free and particle-containing PI/PIB blends at t=0 and 30 min.

(a) time=0 (b) time=0.5 hr

114
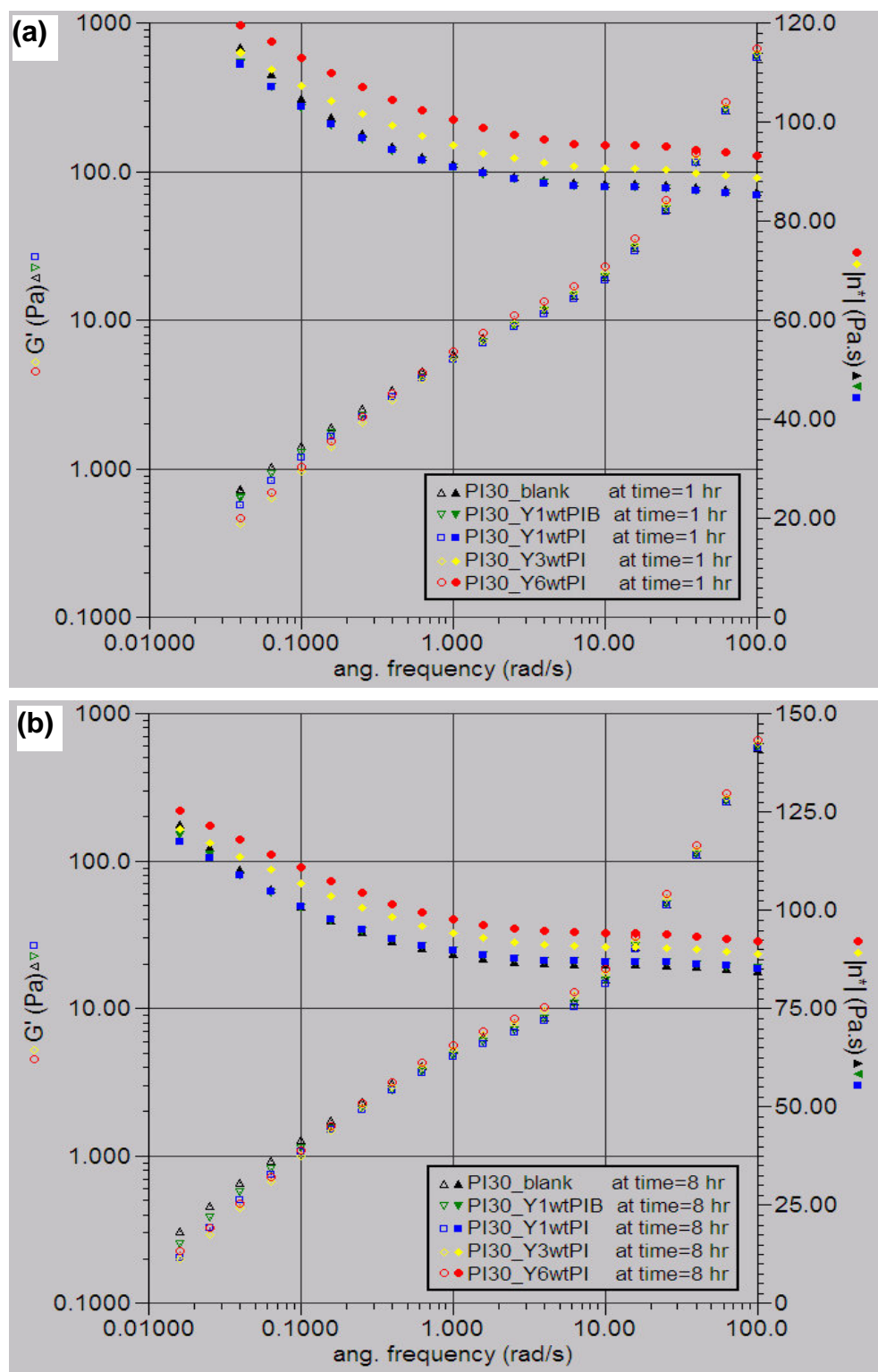
Figure 45. Dynamic oscillatory behaviors for particle-free and particle-containing PI/PIB blends at t=1 hr and 8 hr.

(a) time=1 hr (b) time=8 hr.

The samples for morphology visualization in a shear cell follow the same sample preparation procedure for rheological measurements, i.e. hand blending in a Petri dish for 2 min, degassing for 30 min and then preshearing at 1000 Pa shear stress corresponding to the observation spot that is 8 mm from the center of rotation. The shear stress is a linear function of radius in the parallel plate geometry of the shear cell. We can also observe the local morphology development under different preshearing stress levels in one single experiment. The gap between plates was set to be 150 μm in order to take pictures of acceptable quality.

In Figure 46, we show the local morphology development at radius of 8mm in the confined space between two parallel plates for particle-free sample PI30_blank at t=0, 10, 35, 60 min after the preshearing. We were able to capture the micrograph as soon as the preshearing stops. Figure 46a has the lines or elongated structures along the diagonal direction of the figure. That is actually the velocity direction of the rotational preshearing. The domain size grows with time from Figure 46a-d. At t~35 min, the domain size has increased to about 150 μm, which is same as the gap between the plates. We note that the morphology at this stage appears to be a two dimensional network structure instead of three dimensional bicontinuous structure. The connection "junctions" of the 2D bicontinuous structure do not have pillars perpendicular to the surface of the picture.
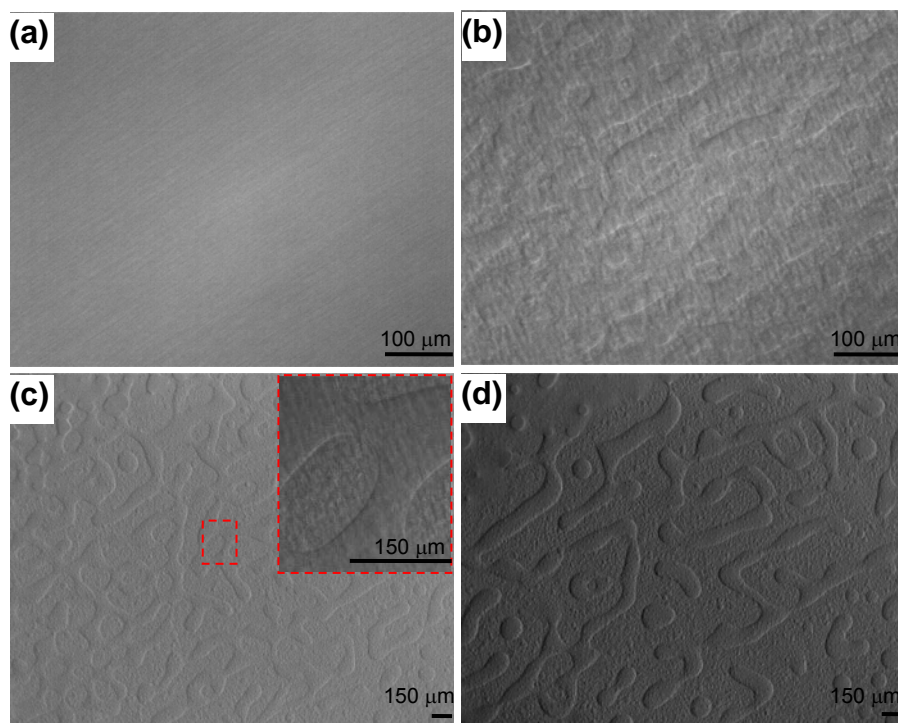
Figure 46. Micrographs of PI30_blank in a shear cell for the amount of time denoted after the preshearing. (a) t=0 min (b) t=10 min (c) t=35 min, its inset is for t=32 min. (d) t=60 min. The inset of figure c is a magnified micrograph for the denoted area. (Please refer to a PDF file if the printout is not clear.)

We presumed that the confined space may affect the morphology development because the filament retraction in a bicontinuous structure is limited to two dimensions at this stage. Therefore, our first thought believed that the confined space would slow down the morphology development as compared to open space. Samples in a Petri dish can be considered as samples in the open space due to the thickness (1~2 mm).

However, as shown in Figure 47, when we compared side by side the micrographs taken at t~30 min and t~60 min of sample in a confined spaced to micrographs taken at t~30 min and t~60 min of sample in a Petri dish, we found that the domain sizes of confined space samples seem to be larger. This is contradicting to our first thought. To understand the effect of confinement, in the following, we will show morphology development of particle-containing

117

samples in the confined space and then rescale the pictures to perform a side-by-side comparison

for samples in confined space and in open space.
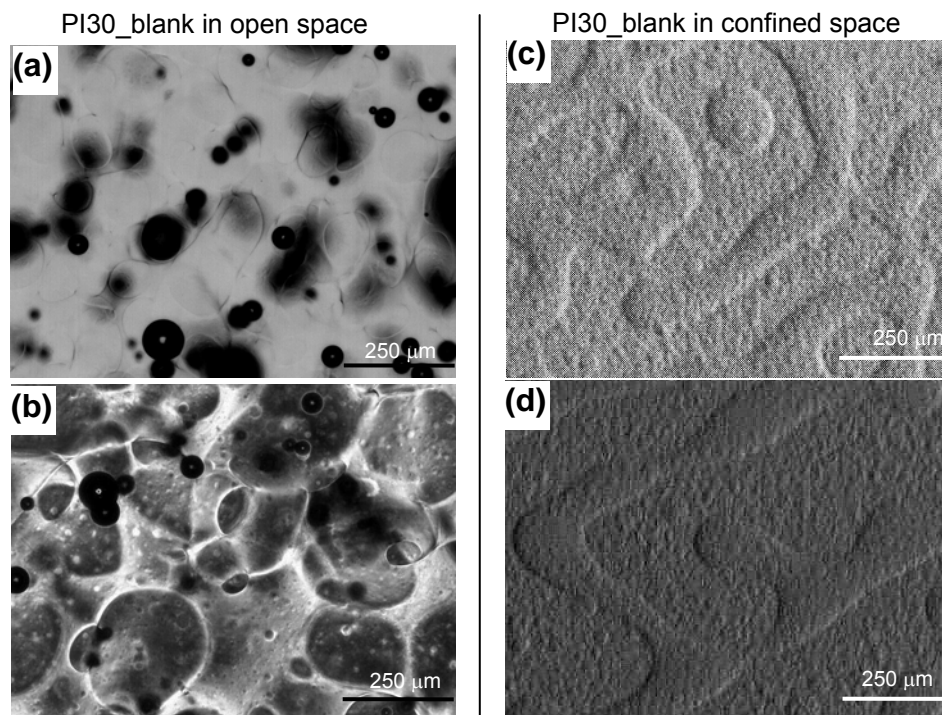
Figure 47. Side-by-side micrograph comparison of PI30_blank in open space and confined space

(a)(b) open space; (c)(d) confined space at two different times after blending or preshearing.

(a,c) t~30 min. (b,d) t~60 min.

Figure 48 shows the morphology development for PI30_Y1wt PI in the shear cell. At

t~30 min, the average domain size is just below the gap size 150 μm. The structure has pillar

perpendicular to the focus plane and appears differently to PI30_blank (Figure 46c). However,

the bicontinuous structure collapsed gradually afterwards. At t~60 min, it is a layer structure at

most area. Only a few "necks" remain near the right, bottom corner of Figure 48d. A sequence

of pictures (not shown) taken at every minute for the whole evolving process (~60 min) show

that the bicontinuous structure collapses due to the thinning of the pillars (i.e. necks

perpendicular to the picture plane) and necks. We speculate that the preferential wetting of the

118

polymer component on the glass surface for a thin sample (150 µm) may accelerate this collapse process, causing the faster morphology development in the confined space. Figure 49 shows the comparison to the same sample in open space.
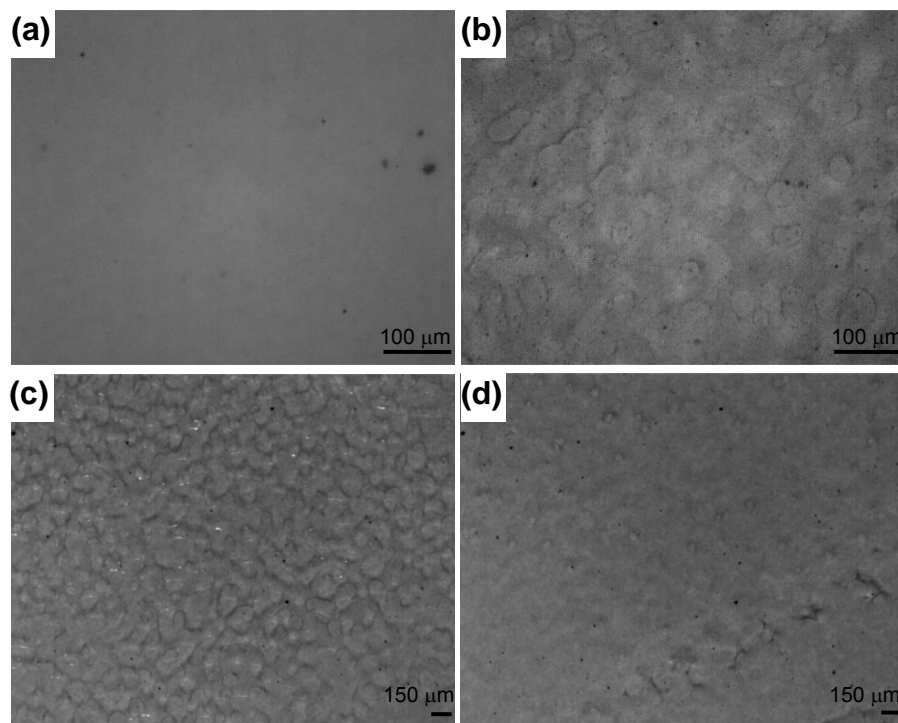
Figure 48. Micrographs of PI30_Y1wtPI in a shear cell at the time denoted after the preshearing.

(a) t=0 min. (b) t=10 min. (c) t=30 min. (d) t=56 min.

PI30_Y1wtPI in open space   PI30_Y1wtPI in confined space
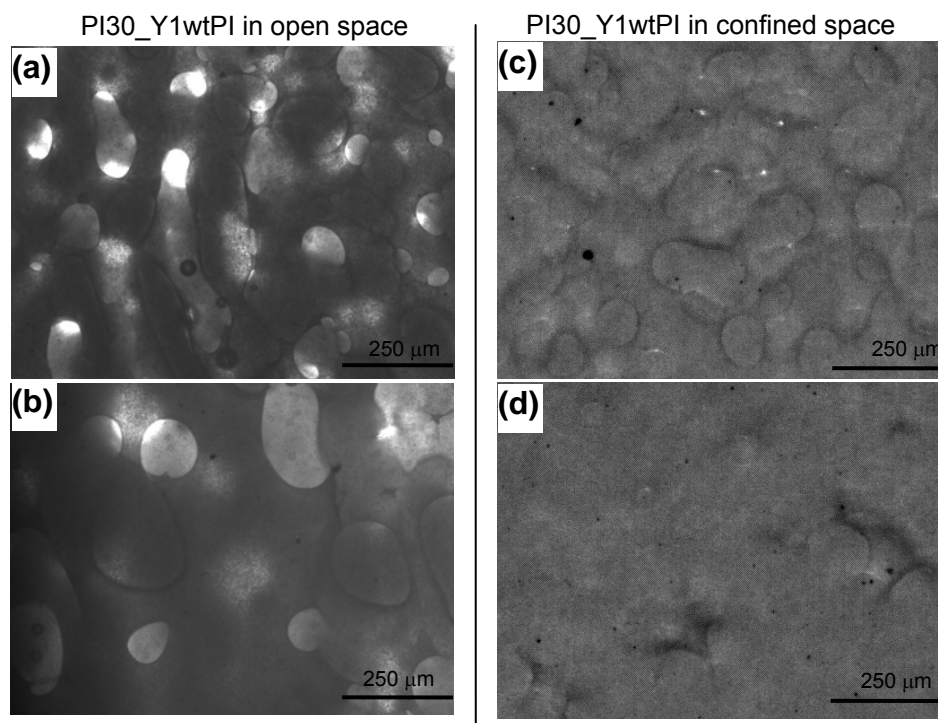
Figure 49. Side-by-side micrograph comparison of PI30_Y1wtPI in open space and confined space

(a)(b) open space; (c)(d) confined space at two different times after blending or preshearing.

(a,c) t~30 min. (b,d) t~60 min.

Figure 50 shows the morphology development of PI30_Y3wtPI in the shear cell. Due to the intense light scattering and adsorption from the yellow particles, it is difficult to get good images. In the inset of Figure 50c, only a small section appears in focus. Under every out-of-focus dark spot, there is actually a pillar structure. The particle concentration at the pillars based on per area is higher than others, therefore those spots appear darker. In Figure 50d, the bicontinuous structure has partially collapsed, leaving region of lighter and darker spots.

120
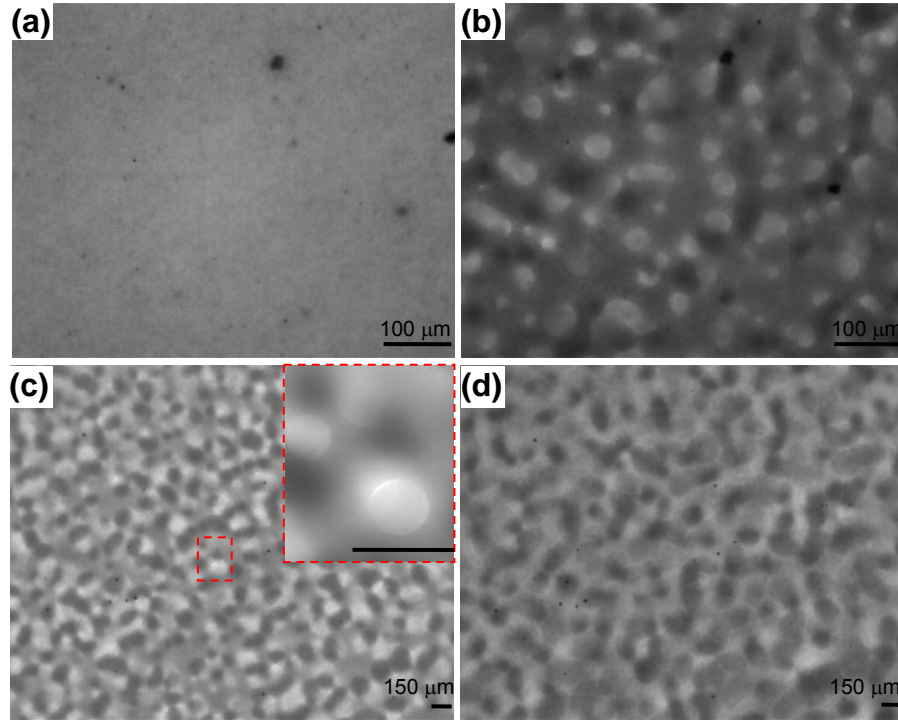
Figure 50. Micrographs of PI30_Y3wtPI in a shear cell at the time denoted after the preshearing.

(a) t=0 min. (b) t=10 min. (c) t=33 min, inset for t=30 min (d) t=60 min.

The comparison of PI30_Y3wtPI in open vs. confined space shows dramatic difference. While the thick sample in a Petri dish was able to maintain the bicontinuous structure (see Figure 51b), the sample in the thin confined space collapsed into a layered structure. As we adjusted the focal plane, the plane first coming into focus usually has particles everywhere. Therefore, we speculated that there was a preferential wetting layer on the glass surface. The wetting effect is expected to be much more profound in a thin sample. We hypothesize that the wetting effect affects the morphology development, which may explain the unexpected rheological data (not much difference between particle-free and particle containing samples).
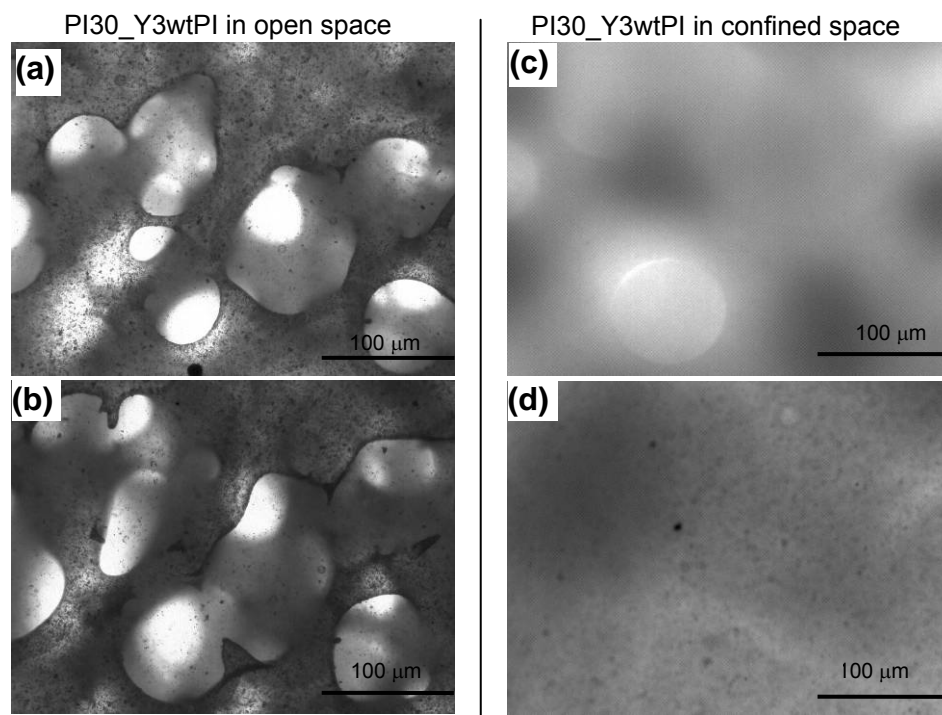
Figure 51. Side-by-side micrograph comparison of PI30_Y3wtPI in open space and confined space

(a)(b) open space; (c)(d) confined space at two different times after blending or preshearing.

(a,c) t~30 min. (b,d) t~60 min.

To conclude Section 5.3.3, we confirmed that the simple shearing can reset the bicontinuous morphology in the confined space between plates from the optical visualization in a shear cell. Therefore, the power law behavior of the storage modulus vs. angular frequency at the low frequency region is indeed characteristic of bicontinuous structure for the current system. For all the PI30 blend samples, the preshearing at 1000 Pa can rest the bicontinuous morphology and gives similar G' curves for all blend samples. However, we do not fully understand why the particle-free and particle-containing samples behave so similarly in the time evolution of rheological data, while we observe the dramatic effect of interfacial particle jamming for thick samples in Petri dishes. We presumed that the preferential wetting of one of the polymer components may accelerate the collapse of a bicontinuous structure in a confined geometry.

Therefore, the rheological measurement in the cone and plate geometry is not suitable for the current system as the sample is thin (linear thickness between 29~349 μm). In the future, we might try the parallel plate geometry with a mm-sized gap for the rheological measurements. The drawback of the parallel plate method is that it may not generate a uniform bicontinuous morphology because the stress applied is a function of radius. In turn, the parallel plate method is not adequate for studying the morphology development of the current bicontinuous morphology generated by shear stress. However, it may provide more information to support our hypothesis of the surface wetting effect on the collapse of the bicontinuous morphology in a confined geometry.

5.4 DISCUSSION

5.4.1 Proposed particle transfer and particle adsorption mechanism

In Section 2.1, we mentioned that partially wettable particles (i.e. contact angle, $0° < \theta < 180°$ tend to adsorb at the fluid-fluid interfaces. There is an energy benefit as the particle cross-sectional area replaces the unfavorable fluid-fluid interface (see Figure 52a). The theoretical pictures (Figure 52a and b) represents well an oil-water system and any other system that has a relatively large desorption energy as compared to thermal motion energy and the preferential interaction energy between the particles and their preferred phase, if any. However, for certain systems that have small interfacial tension, or nanoparticles, or contact angle close to $0°$ or $180°$, the energy trap at the interface is relatively small compared to this preferential interaction energy between the particles and phase B (see Figure 52c). Therefore, from a thermodynamic point of view, the

123

ultimate state of the particles could be staying in phase B. The relative depth between the energy trap at interface and the energy well in phase B is system dependent. It is unknown for our current system (FeOOH particles in PI/PIB blend), since the pair interaction between FeOOH particles and phase B is unknown and the contact angle is hard to measure.

From the experimental observation described in Section 5.3.1 (Figure 37 and Figure 38), we presumed that the thermodynamic picture (i.e. free energy curve as a function of particle position) for our current system is close to Figure 52c. When the depth of the particle desorption energy and the depth of preferential interaction energy is comparable, the relative depth and the detailed particle transfer process will determine the distribution of particles.
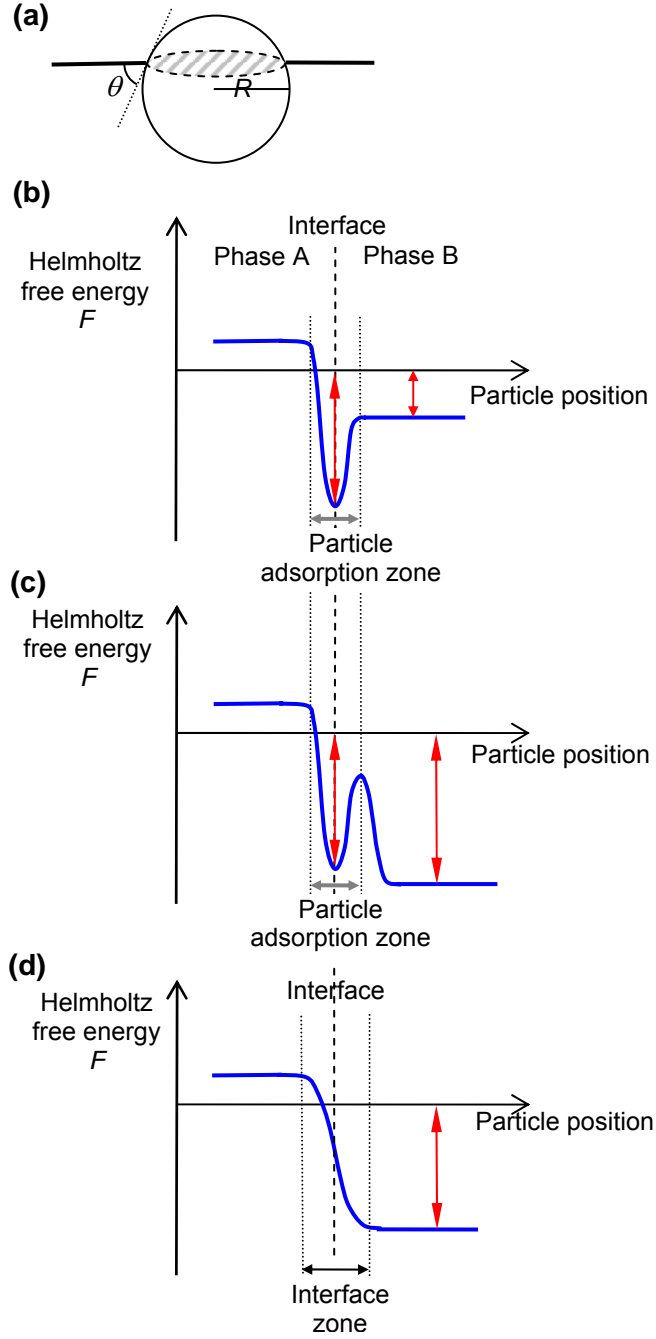
Figure 52. Schematic representation of a particle adsorbed at interface and the associated free energy.

(a) Schematic representation of a particle replacing the unfavorable fluid-fluid interface of the denoted cross-sectional area. (b) Free energy curve as a function of particle position. The particle has preferential interaction with phase B as compared to phase A, but the energy trap at interface dominates. (c) Free energy curve as a function of particle position. The energy trap at interface is comparable in size to the preferential interaction. (d) Free energy curve as a function of particle position for a particle fully wetted by phase B under equilibrium.

Beside the thermodynamic pictures above (Figure 52b and c), there is another possibility discussed by Fenouillot et al.[38] in a recent review paper. The review article focuses mainly on high temperature melt-blended polymer blends. They pointed out that if particles are incorporated into the polymer component having the lower affinity with particles and then mixed with the higher affinity polymer, the particles can transfer across the interface during mixing, and this may temporarily places the particles near or at the interface. If mixing is stopped at the adequate time, the particles will remain at the interface upon cooling the blend whose morphology is then quenched into a non-equilibrium state. In other words, there exists an optimal mixing time that results in the most particles distributed near or at the interface. In this case, the particles are not partially wettable to the polymer-polymer interface. We summarized their thermodynamic picture in Figure 52d.

We believe that Figure 52d is not the case for our system. The reasoning comes from two observations below. Firstly, when we first incorporate particles into PIB component before mixing with the other component, we observe that some particles appear at the interface at the later stage (~1 hr for PI30_Y1wtPIB) of morphology development, as shown in Figure 53. The thermodynamic picture in Figure 52d is less likely to result in this observation.
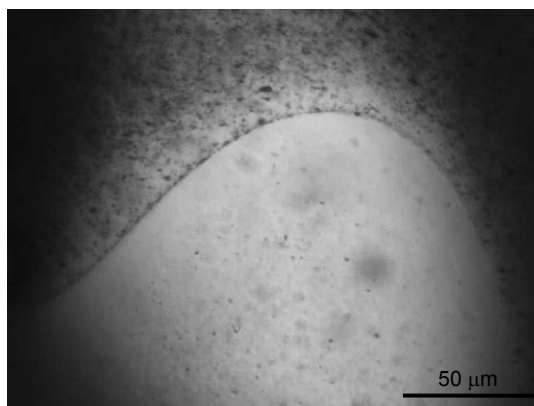
Figure 53. Some particles appeared at the interface at a later stage of morphology development when particles initiates from PIB component.

Secondly, we tried different length of hand blending time, including 2, 5, 10 and 20 min for sample PI30_Y1wtPI. Particle adsorption at the early stage is evident for all trials. We were not able to distinguish any difference on the adsorption efficiency among them. Intense mixing does not seem to bring more particles to the interface. Repeated mixing only reset the phase separation and particle adsorption process. Therefore, we believe that the thermodynamic picture Figure 52c closely represents our system. We will propose a detailed particle transfer and particle adsorption mechanism in the following.

Figure 54 show the proposed mechanism. Because the polymer components we used have low molecular weights and thus short chain length, the polymer coils are much smaller than the particles. We therefore use a continuum model to represent the polymers, instead of drawing the individual polymer chains. We also use dark or light color to represent the composition ratio of PI and PIB; pure PI is represented as black in color and pure PIB is represented as white. In Figure 54a, elongated FeOOH particles dispersed in PI component are mixed with pure PIB. In Figure 54b, due to the partial miscibility and the short chain length, the flow during hand blending induces phase mixing between PI and PIB. During the shear flow, the polymer coils

are likely to be extended short chains, and the components are homogeneously distributed. The PI polymer chains that initially adsorbed at the particle surface remain on the particle surface as a boundary layer, but they will slowly be replaced by PIB chains due to the more favorable interaction between PIB and particles. In Figure 54c, as the blending flow stops, the PI and PIB components phase separate via a spinodal decomposition process at room temperature. A new interface forms between the PI-rich and PIB-rich phases. Because the adsorbed PI polymer chains on particles have not yet be replaced by PIB chains, particles partition into PI-rich phase at this stage.

In Figure 54d, as the PI polymer chains at particle surface exchange with PIB chains nearby in the PI-rich phase, the particles move toward the interface (equivalently, the interface moves toward particles) due to the flow caused by domain coarsening. When particles encounter the interface, only particles with "the correct orientation" would get adsorbed at the interface (Figure 54d). We presumed that the correct orientation is when the long axis of particles is parallel to the interface. In that way, more unfavorable fluid-fluid interfacial area can be replaced by the presence of a particle. The particles without correct orientation (or do not orient fast enough to adsorb) would transfer across the interface due to the preferential interaction with PIB-rich phase.

Certainly, this orientation argument is fully speculative. The true reason cannot be tested. In the best scenario, the adsorption efficiency of the same particles of different geometries can be compared. It is not possible for our current system, because FeOOH particles are crystalline and thus have a defined shape (elongated). Nevertheless, it is reasonable to state that during a particle transfer process, the efficiency of particle adsorption is not 100% even though there may be an energy "local minimum" (see Figure 52c). We continue our model description in Figure 54e.

At the last stage (Figure 54f), for the transferred particle, the surface is completely covered with the preferred PIB chain, while a portion of particles are adsorbed and trapped at the interface. The proposed mechanism is also in line with the thermodynamic picture Figure 52c.

The thermodynamic pictures also provide us clues on the strategy for efficient particle adsorption. For the case in Figure 52b, the mixing procedure does not make any difference to the final percentage of particle adsorption. For the cases in Figure 52b and c, it is crucial that we incorporate particles into the lower affinity phase in order to get sufficient particle adsorption.
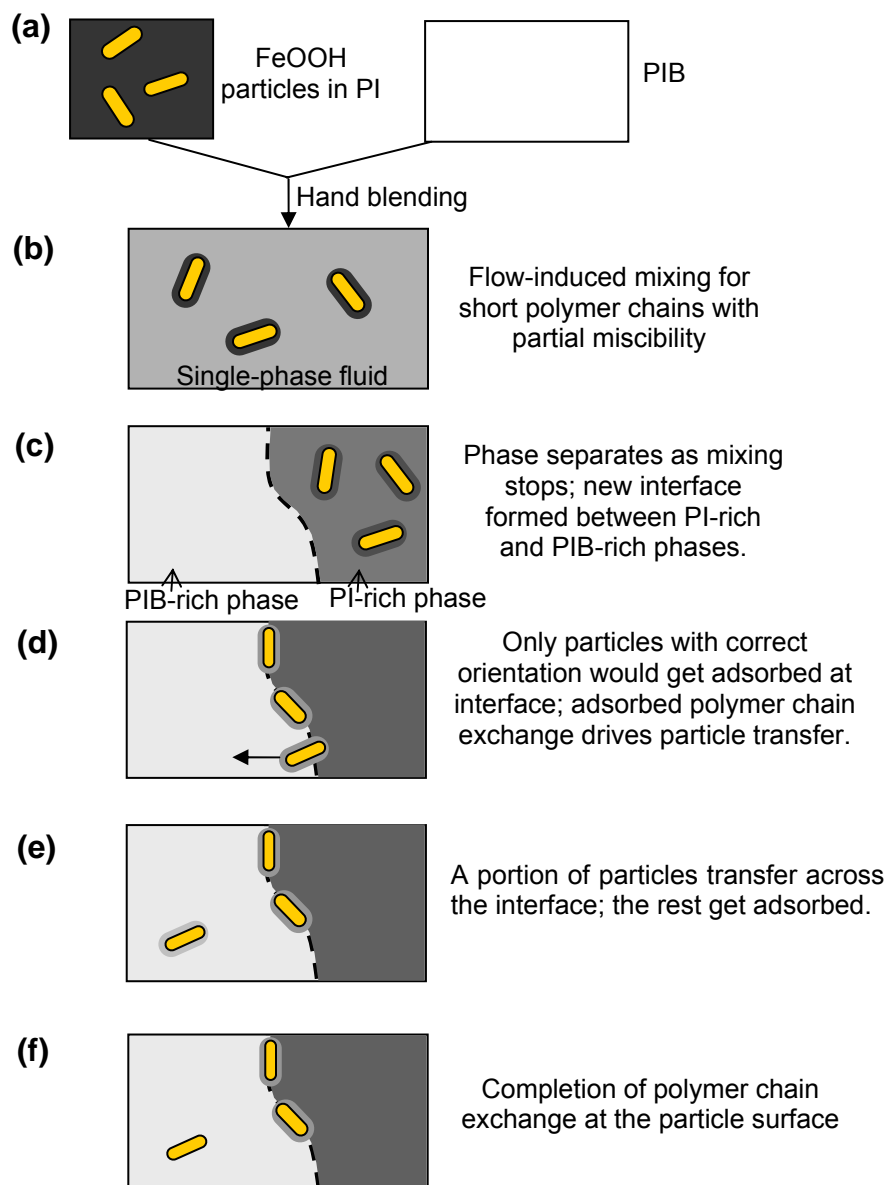
Figure 54. Proposed particle adsorption and particle transfer mechanism for FeOOH particles/PI/PIB blends.

This mechanism is proposed for the blend samples where the particles are initially dispersed in PI, the

PI30_Y1wtPI blend for example.

5.4.2 Analysis of volume ratio

Most often, bicontinuous morphology are found when the components have equal volume for a viscosity-matched system or less than 50 vol% for the less viscous component for a viscosity-unmatched system. In the equation form,

$$\frac{\phi_{A,bicon.}}{\phi_{B,bicon.}} \cdot \frac{\eta_B}{\eta_A} \cong 1 \tag{5.1}$$

where $\phi_{A,bicon.}$ and $\phi_{B,bicon.}$ are the volume fractions of component A and B at the phase inversion point, respectively. η_A and η_B are the viscosities for component A and B. At the PI30 composition, if we ignore the mutual solubility of PI and PIB, the calculation gives the following,

$$\frac{\phi_{A,bicon.}}{\phi_{B,bicon.}} \cdot \frac{\eta_B}{\eta_A} = \frac{29.9}{70.1} * \frac{68.9}{131} = 0.22 \ll 1 \tag{5.2}$$

Therefore, at the first glance, it is unexpected that the current PI/PIB system can give a bicontinuous morphology for PI30 samples. We attribute the off-center composition to the partial miscibility between PI and PIB. To determine if this is indeed the case, we conducted a test to determine the volume ratio of PI-rich phase and PIB-rich phase at equilibrium. A hand-blended sample of 20 gram PI30_blank was loaded into a graduated centrifugal tube. Phase separation of the two phases occurred in the tube until both the top and the bottom phase become clear and unified. The process takes weeks. Centrifuge was not helpful as the density difference between the phases is small. Drops were distorted in shapes after centrifuge, but the coalescence was not accelerated. The volumes were finally read off the graduated tube after the separation process is mostly completed. The volume fraction of PI-rich phase was determined to be 0.4. Assuming the increase volume fraction is only caused by PIB dissolved in PI, the viscosity for

the PI-rich phase ($\eta_{PI-rich}$) was corrected to 115 Pa.s. Therefore, the correction of viscosity would decrease the viscosity ratio term and makes the calculation in Eq. (5.2) closer to unity. After the correction, $\frac{\phi_{A,bicon.}}{\phi_{B,bicon.}} \cdot \frac{\eta_B}{\eta_A}$ is equal to 0.4 instead of 0.22. The mutual miscibility only partially explains why the volume fraction is off-center. A more precise model that is better than Eq. (5.2) may be needed to further explain the composition forming the bicontinuous structure for the current system.

From a different point of view, we have speculated in Section 5.4.1 that the bicontinuous morphology is generated by flow-induced mixing/demixing via a spinodal decomposition process. If the speculation is true, the criteria of generating a bicontinuous morphology may be less sensitive to the volume ratio and viscosity ratio of the two phases.

5.5   CONCLUSION

We demonstrated an example of bijel composite materials using the polymer blend system PI/PIB and FeOOH particles. The bicontinuous structure is created by hand blending the components in a Petri dish. It is speculated that the shearing flow induces a phase mixing, and the demixing via the spinodal decomposition process takes place to resume the concentration fluctuation upon the cessation of flow. We speculate that the partial miscibility between the PI and the PIB components and the low molecular weights of components are responsible for this uncommon flow-induced mixing.

Furthermore, we proposed a particle transfer and adsorption mechanism in order to explain two experimental observations: (1) only if particles are initially dispersed in PI, can the

added particles arrest the bicontinuous structure efficiently (see Figure 40); (2) Particle adsorption is not 100% and some particles appear in one of the bulk phases, which was later determined to be PIB. Based on experimental evidence including the microscopic images and rheological measurements for particle dispersions, we attribute the stabilization of the evolving bicontinuous morphology to interfacial particle jamming. The bicontinuous morphology can be arrested at a smaller length scale by increasing the particle loadings (see Figure 40). A bijel-structured polymer blend is thus realized.

The rheological data, however, cannot show a significant difference between particle-free and particle-containing samples. We presume that the thin sample in the cone and plate geometry makes the surface wetting effect not negligible. The surface wetting may accelerate the collapse of the bicontinuous structure in a confined, thin sample.

Beside the particle transfer model, we also proposed a thermodynamic picture to explain the observations, and we also suggested a strategy for efficient particle interfacial adsorption (i.e. mixing particles with the lower affinity component first). The mixing procedure could be crucial to determine the adsorption efficiency depending on the thermodynamic picture of a system.

6.0   POLYMER BLEND WITH NONRELAXING DROPS

The most common morphology for immiscible polymer blends is a droplet-matrix morphology. In this chapter, we further extend the application of interfacial particle jamming to control the morphology of a droplet-matrix blend. Specifically, we utilize the drop coalescence induced by flow conditions to generate elongated drops and show that particle-coated elongated drops do not relax their shape over time upon cessation of flow, which is a signature of interfacial particle jamming. By applying the flow, an intrinsically-isotropic droplet-matrix morphology is converted to an anisotropic morphology (i.e. droplet-matrix morphology with many elongated drops) due to interfacial particle jamming on drop surfaces.

The system of interest is FeOOH particles in PI/PDMS blend. The PI/PDMS blend is a "model" system in the sense that the two immiscible polymers are chosen for their experimentally-convenient attributes such as thermal stability, low cost, transparency, etc. Most importantly, both the polymers are viscous liquids at room temperature and hence the blends can be prepared by hand-blending with a spatula, without requiring polymer processing equipment. FeOOH particles have been shown to be interfacially active for this blend system[74]. The goal of this chapter is to investigate the morphological and rheological effects of interfacially-active particles in a droplet-matrix polymer blend. We utilize rheology as the tool to trace the drop relaxation and the change of the mean drop size, as well as the elastic recovery of the blend after cessation of shear stress.

Besides, we also unexpectedly observed "particle-assisted network structures" that to our knowledge, have never been noticed for the PI/PDMS system. The network structures are stable over time. After careful examination of particle-free blends, we observe the existence of a very transient bicontinuous structure immediately after blending. We will discuss the formation of this network structure.

6.1   MATERIALS

FeOOH particles were used in this study (see details in Section 3.1). Polyisoprene (PI) and polydimethylsiloxane (PDMS) were the two polymer components. In order to keep data interpretation simple, we chose to work with a viscosity-matched system. The viscosity of the PI component is 131 Pa.s at 25˚C. Since there was no PDMS of such viscosity commercially available, we decided to mix two available PDMS products of different average molecular weights to obtain the PDMS component of viscosity 131 Pa.s. The two commercial products are Rhodorsil Fluid 47V100,000 and Rhodorsil Fluid 47V200,000. We estimated a mixing ratio based on the blending rule proposed by Montfort et al.[75] This rule reads $\eta_{blend}^{*a} = w_1\eta_1^{*a} + w_2\eta_2^{*a}$ where the constant a=0.294, w_1 and w_2 are weight fractions of components, η_1^*, η_2^* and η_{blend}^* are complex viscosities of components and blend, which are close to the steady-shear viscosities for Newtonian fluids. The mixing ratio was 0.588 to 0.412 by weight. The viscosity of the home-mixed PDMS batch was measured to be 130 Pa.s. The properties of all components are listed in Table 9.

Table 9. Properties of components for PI/PDMS system.

Note that the PDMS component is home-mixed in order to match the viscosity of the PI component.

		Supplier	Cat.#	MW (g/mol)	Viscosity [a] (Pa.s)		Density [b] (g/cm^3)
Polyisoprene (PI)		Kuraray Co, Ltd	LIR-30	29,000	131		0.91
Home-mixed Polydimethylsiloxane (PDMS)	PDMS 1	Rhodia Chemicals	Rhodorsil Fluid 47V 100,000	135,600	94	130 (mixed PDMS)	0.972
	PDMS 2	Rhodia Chemicals	Rhodorsil Fluid 47V 200,000	200,000	195		
Iron oxyhydroxide (FeOOH)		Elementis Pigments Inc.	4088D	/	/		4.03

[a]. Steady-shear viscosity measured by an AR2000 rheometer.
[b]. Quoted by manufacturer

6.2 METHODOLOGY AND CHARACTERIZATION

6.2.1 Generating droplet-matrix morphologies by hand blending

Since the polymer components (PI and PDMS) are both molten at room temperature, mixing was performed by hand blending with a plastic spatula in a Petri dish. The stress applied during hand blending broke big lumps of polymer into small drops. For particle-free blends, the blends turned opaque almost immediately and had an elastic texture as compared to the transparency and viscous texture of components. We presume that the color change indicates formation of drops and new interfaces which scatter light due to the reflective index difference at interface. The droplet-matrix morphology was confirmed under an inverted microscope. We chose to work with the polymer blend compositions that are close to the midway composition (50/50), so there

would be a large amount of drops formed in the matrix at a given stress. The expectation is that more drops give more drop coalescence events, and make it more likely to observe elongated drops which form from drop coalescence under flow conditions.

The sample designation for this FeOOH particles in PI/PDMS system is PI*x_y*, where *x* is the PI weight percentage and *x*=40, 50 and 60. Most of our experiments were conducted at the PI60 composition. *y* is the weight percentage of FeOOH particles, and *y*=0, 0.25, 2, 4 and 8. The mixing sequence for particle-containing samples was always as follows. Particles were first mixed with the "majority" polymer component until a homogeneous particle dispersion was obtained, and then the particle dispersion was blended with the "minority" polymer component for 4 min.   The sample designation, its weight percentage and volume percentage are summarized in Table 10.

Table 10. Sample composition table for the PI/PDMS system

Sample designation	FeOOH wt%	PI wt%	PDMS wt%	FeOOH vol%	PI vol%	PDMS vol%
PI60_0	0	60	40	0	61.6	38.4
PI60_0.25	0.25	59.85	39.9	0.06	61.5	38.4
PI60_2	2	58.8	39.2	0.47	61.3	38.2
PI60_4	4	57.6	38.4	0.96	61.0	38.1
PI60_8	8	55.2	36.8	1.98	60.4	37.7
PI40_0	0	40	60	0	41.6	58.4
PI40_2	2	39.2	58.8	0.48	41.4	58.1
PI40_4	4	38.4	57.6	0.97	41.2	57.8
PI40_8	8	36.8	55.2	2.00	40.8	57.2
PI50_0	0	50	50	0	51.6	48.4

6.2.2 Phase-continuity test method

The morphology of a polymer blend determines the properties and thus determines the end application of the material. For a droplet-matrix morphology, the component that forms the matrix generally dominates the properties of the blend. Therefore, it is important to know which phase is the continuous phase (i.e. matrix) and which phase is the dispersed phase (i.e. drops). Because the volume fractions of the immiscible phases in the studied system are so close to each other, we cannot presume that the majority component would be the continuous phase since the phase inversion point is not necessarily 50/50. Therefore, we must conduct the phase continuity test for each composition that we work with.

In a simple form of phase continuity test, we can probe the chemistry of the matrix phase with an "agent" of known chemistry by bringing them into contact. Here, we apply one of the simplest chemistry properties, which is miscibility. We know that silicone oil (low molecular weight PDMS, Brookfield Inc., Fluid 1000, 0.975 Pa.s) is fully miscible with the PDMS component in the PI/PDMS blend but immiscible with PI. We also know that mineral oil (mixed alkane or paraffin, Fisher Scientific Inc.) is miscible with the PI component in the blend but immiscible with PDMS. Therefore, we can determine the matrix phase following the procedure below. A bent metal wire was used to pick up a small lump of the polymer blend as the sample (yellow in Figure 55a), and the sample was immersed in silicone oil or mineral oil in a Petri dish as shown in Figure 55a. When we observe the sample under microscope, if the sample lump has a sharp and roundish interface with the liquid outside, then the matrix phase is immiscible with that liquid (see Figure 55b). If the matrix phase is miscible with the testing liquid, the interface is irregular in shape and/or the sample may release the drops of the blend to the liquid (see

138

Figure 55c). We need to use both silicone oil and mineral oil as the testing liquids in order to get

unambiguous results because whether or not the interface is sharp must be judged relatively.
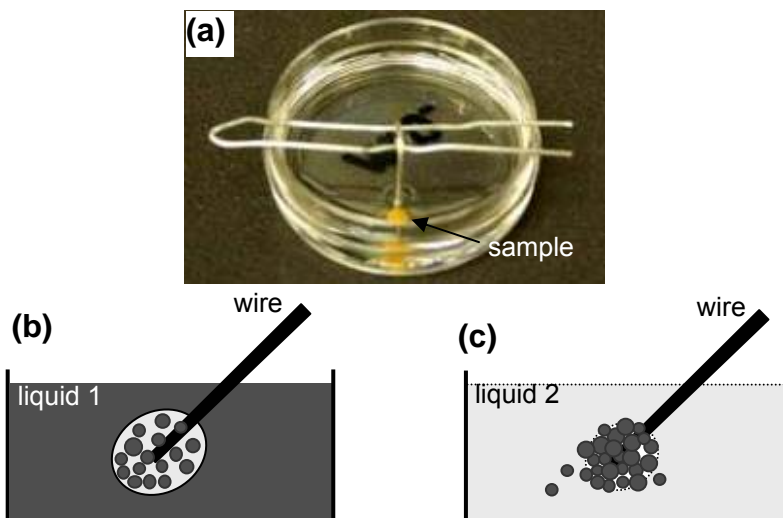
Figure 55. Setup and methodology for phase continuity test.

(a) Setup for phase continuity test. The sample (yellow in color) immersed in the liquid was placed on the tip of a

metal wire which hangs over another wire. (b) Schematic representation of a blend sample which is immiscible with

the testing liquid 1. (c) Schematic representation of the same blend sample in figure b which is miscible with the

testing liquid 2. Liquid 1 and 2 are silicone oil and mineral oil.

6.2.3   Visualization under flow conditions in a shear cell

The same home-built shear cell described in Section 5.2.3 was used in this study. A degassed

sample was sandwiched between two parallel glass plates, and the objective of a microscope was

right above the top glass plate to transmit the optical images. While the top glass plate was

always static, the bottom plate could be precisely rotated in the steady shear mode or dynamic

oscillatory mode (not used) as controlled by the rotor of a strain controlled ARES rheometer. In

this study, the gap was kept at 250 μm. The images were either transmission images which allowed us to see layers of drops stacking in one image when light source illuminated the sample from beneath, or were reflection images which only allowed the drops near the top plates to be seen when light source illuminated the top surface of a sample.

The shear history applied on a sample was composed of two steps (shown later in Figure 66, page 155). In the first step, the sample was sheared for 1000 sec at the shear rate 3 s^{-1} for the location at radius=8 mm. This corresponds to 3000 strain unit for the location at radius=8 mm from the rotation center. The purpose of this relatively high-stress step is to break large drops into tiny drops. We generally waited 10 min before we started the second step. The second step sheared a sample for 5000 sec at the shear rate 0.65 s^{-1} for the location at radius=8 mm. This corresponds to 3250 strain unit for the location at radius=8 mm. The purpose of this long-time shear at the lower stress is to permit flow-induced drop coalescence. We observed the sample for a relatively long time after the second step to trace the retraction behavior of any elongated drops.

Since the shear stress is a function of radius for the parallel plate geometry, we observe several locations of a sample along the radius, mostly at radius= 0 (rotation center), 4 and 8 mm. Because the morphology may depend on shear history, and the shear rate and shear stress are both functions of radius, the morphology information obtained from the shear cell visualization should be considered as "local" morphology information.

6.2.4 Rheological measurements---oscillatory and strain recovery

The rheological measurements were carried out in a stress controlled rheometer (AR2000, TA Instruments Inc.) with a cone and plate geometry (40 mm diameter, 1° cone). Sample temperature was maintained at 25°C with a Peltier plate. Degassed samples were subjected to a desired shear history (shown later in Figure 72, page165). Samples were first sheared at 400 Pa for 2000 strain unit, and then the subsequent recovery upon cessation of shear was monitored, followed by an oscillatory frequency sweep at amplitude of 20% strain. This sequence (steady shear for 2000 strain units, recovery and oscillatory) was repeated at four stepwise decreasing stress levels, which are 400, 200, 100 and 50 Pa (shown later in Figure 72, page 165).

We expect that the information from rheology and from the shear cell visualization can mutually support each other, and thus we may understand whether nonrelaxing drops can form from drop coalescence as induced by steady shear flow.

6.3   RESULTS

6.3.1 Stable droplet-matrix morphology and particle-assisted network structure

As mentioned in Section 6.2.1, we confirmed from microscopy that the droplet-matrix morphology readily formed upon blending for the particle-free blends. Figure 56 shows the droplet-matrix morphologies of particle-free samples PI60_0, PI50_0 and PI40_0.
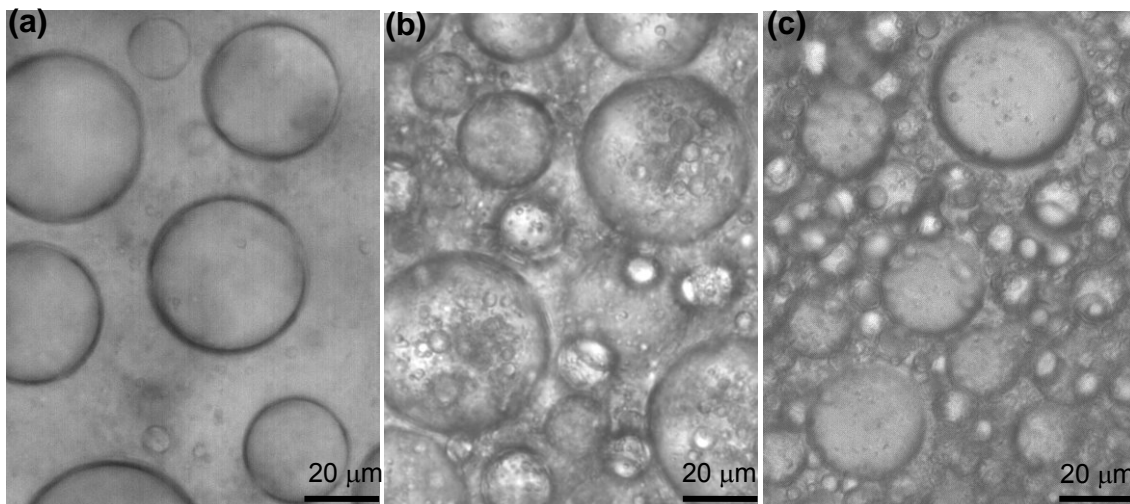
Figure 56. Stable droplet-matrix morphology of particle-free samples.

(a) PI60_0. (b) PI50_0. (c) PI40_0.

However, as we increased the FeOOH particle loading at the PI60 composition to 4 wt% or 8 wt%, we noticed that the morphology was no longer a simple droplet-matrix morphology. Besides some dispersed drops, there were some interconnected structures in samples PI60_4 and PI60_8 as shown in Figure 57. For PI60_4 (Figure 57a and b), there were drops with highly branched shapes. For PI60_8 (Figure 57c, d, e and f), large-scaled interconnected structures were found. These interconnected structures were dark in color, indicating this phase either contained particles or was being covered by particle at the surface. The other phase appeared almost transparent and was the brighter area in the micrographs. Although these dark structures were mostly interconnected to each other and thus closely assembled the bicontinuous morphology that we discussed in chapter 5, there were also a large amount of dark drops coexisted in the blend (Figure 57 c-f). Therefore, it is inappropriate to refer the structure as bicontinuous. In the following, we refer these interconnected structures as "network structures" or "particle-assisted network structures". In Figure 57e and f, we show that the network

142

structure was particularly robust. The structure did not change its shape during the 14 hr observation time.
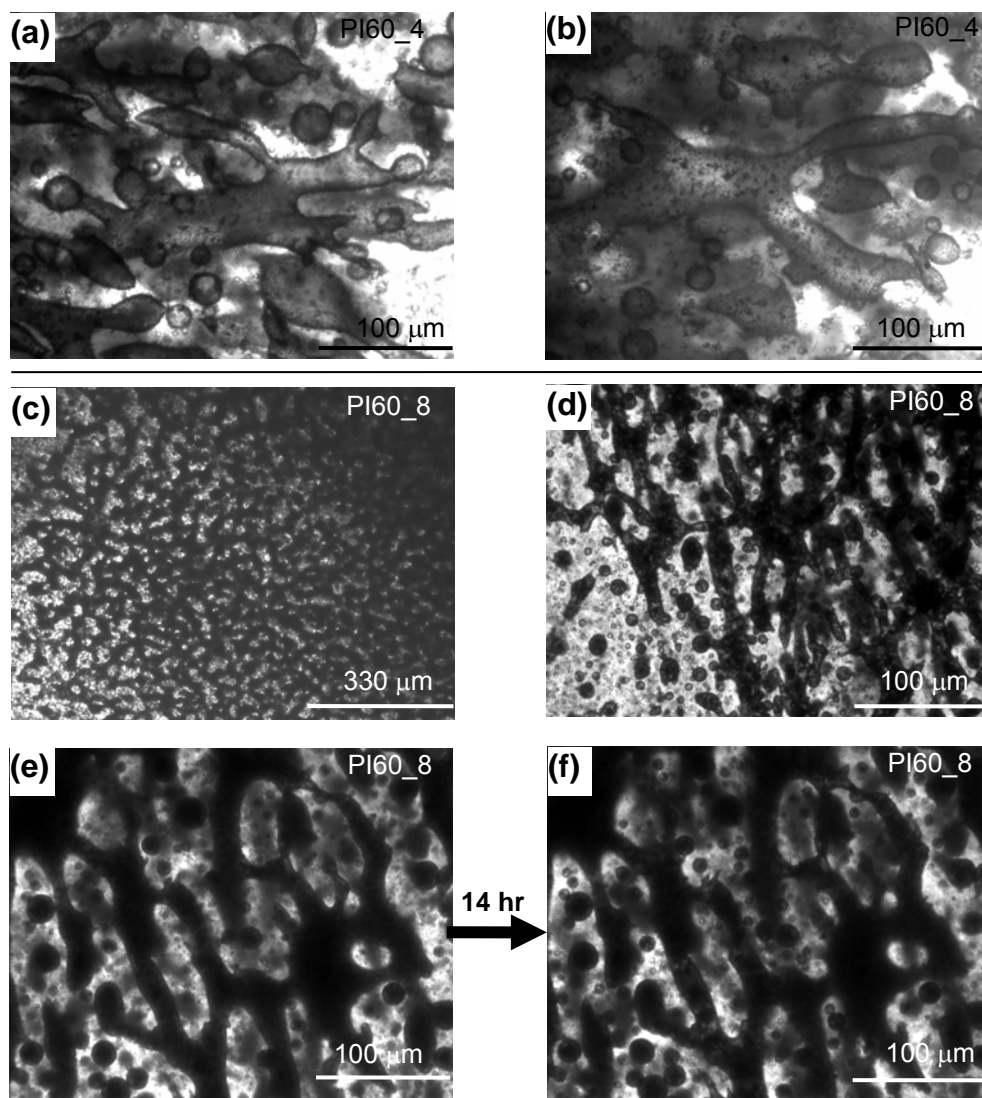
Figure 57. Branched drops of sample PI60_4 and network structures of samples PI60_8 in a Petri dish. (a)(b) Branched drops in PI60_4. (c) Large scaled network structure in PI60_8. (d) Drops coexist with network structure in PI60_8. (e)(f) The morphology did not change within 14 hr in PI60_8. For easy comparison, picture width of figure a, b, d, e and f is 330 μm.

The formation of network structures was unexpected, because the "model" PI/PDMS system was well studied in the literatures and known to have a droplet-matrix morphology[76-78].

We also checked the morphology of PI60_2 in a Petri dish, and no network structure was found. As shown in Figure 58a and b, sample PI60_2 had a droplet-matrix morphology. Most of the drops were spherical in shape, while some other drops are nonspherical or elongated. The dark outlines of drops suggest particle adsorption on the surface of drops. In Figure 58c, there are two elongated drops at the center of the picture. The drops had sharp tips which did not retract or change shapes during our observation. The two magnified micrographs, Figure 58d and e, were taken in two different focal planes. As the outline of drop was in focus (Figure 58d), the interior of drop barely contained any particles in focus. The other focal plane (Figure 58e) showed that the surface of the drop was almost covered completely by particles. Therefore, we know that the dark color of the drops is mainly due to the particle adsorption at the interface between the matrix and drops. Thus, we presume that interfacial particle jamming was responsible for the non-retracting behavior of the elongated drops.

Obviously, the formation of network structure is related to the particle loading. We presume that there is a critical particle loading, or more importantly, a critical particle adsorption area to generate the network structure. Based on the observations, we believe that the critical FeOOH particle loading should lie between 4 and 8 wt% for the PI60 composition. However, the presence of particles does not address why the network formed at the first place. Did particles induced this structure to form, or did they simply stabilize the structure that would otherwise have broken? We therefore carefully re-examined PI60_0 to see if we could find any network structure in the particle-free blend.
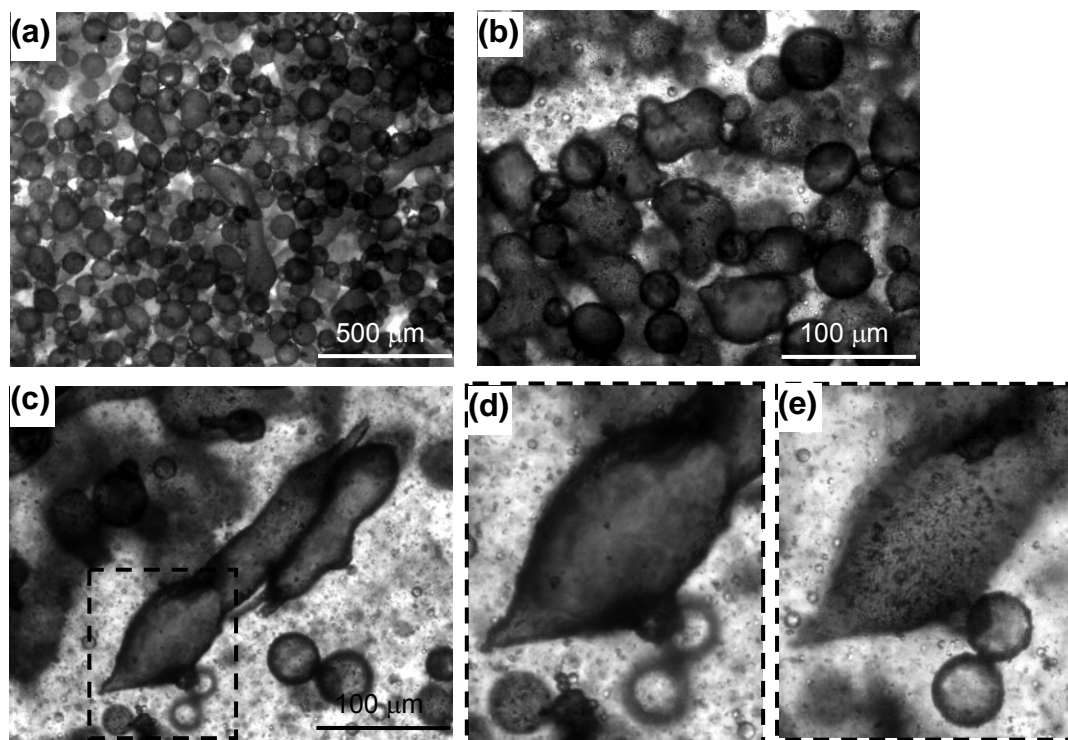
Figure 58. Droplet-matrix morphology of sample PI60_2 in a Petri dish.

(a) Most drops are round in shape. (b) Some drops have nonspherical shape. (c) Elongated drops (d) A magnified micrograph of denoted area in figure c show that there is barely any particles in focus within the drop. (e) A magnified micrograph of denoted area in figure c in a different focus plane shows that a particle monolayer covers the drop surface.

As shown in Figure 59a or c, we indeed found a network structure in PI60_0 immediately after blending (t~0 sec). The transient network structure evolved extremely fast and would revert to a droplet-matrix morphology within a few seconds. It was very difficult to take pictures capturing the network structure because putting a sample on the microscope stage and adjusting focus takes time, and we have repeated the experiment many times just to take good pictures. Only if no adjustment was needed as we quickly put the sample on microscope stage immediately after blending, can these network structure pictures be captured.
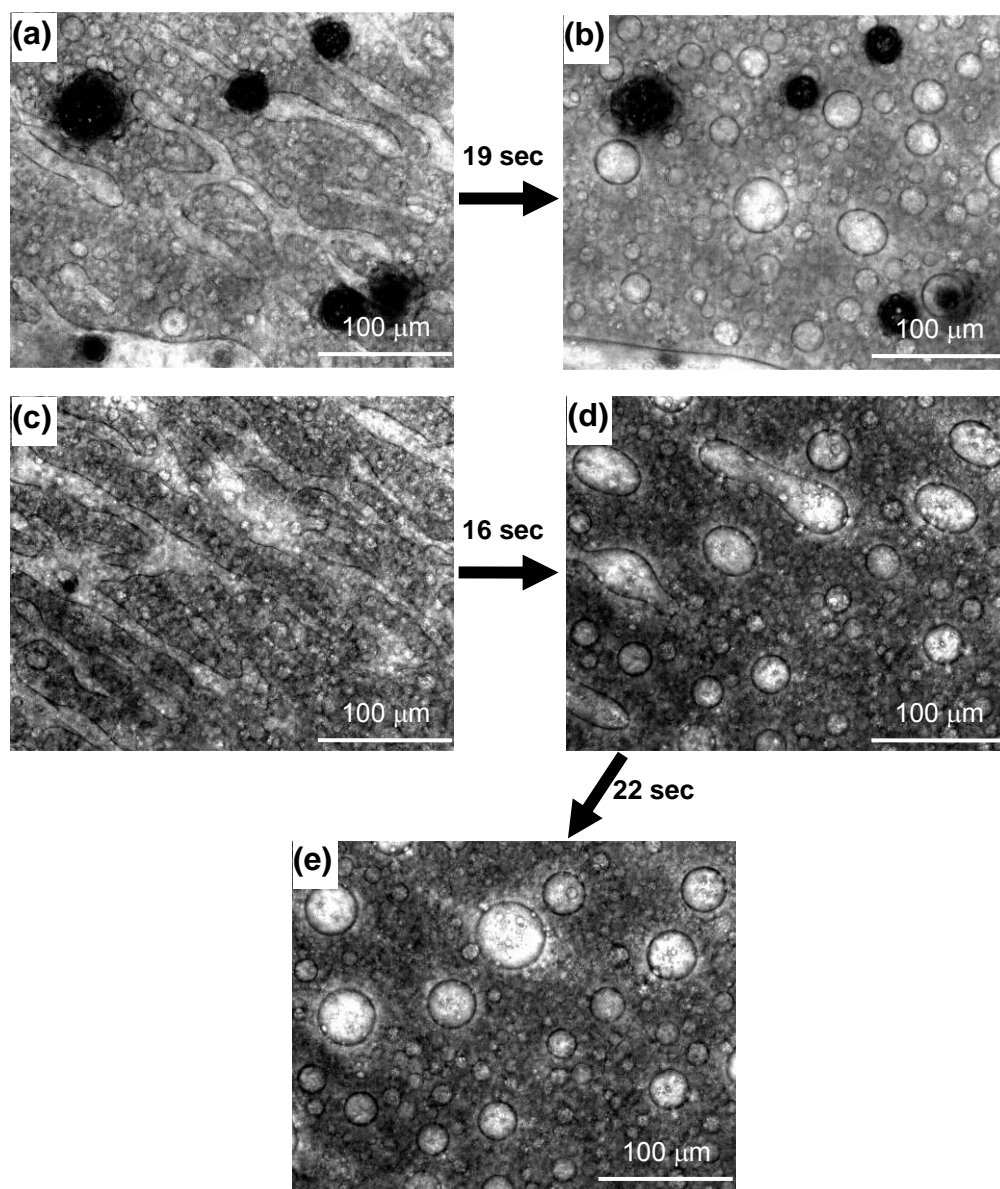
Figure 59. Two examples (a to b) (c to e) of the transient network structure of sample PI60_0 in a Petri dish. Note the very short transition time.

Further, we also checked if network structure could be formed in PI50_0 and PI40_0. Figure 60 and Figure 61 show some network-like structures in micrographs taken immediately after blending for samples PI50_0 and PI40_0, respectively. Figure 60d shows the characteristic "neck" structure of a bicontinuous morphology. All of these micrographs suggest that the

146

presence of a bicontinuous morphology at t~0 sec. We will discussion how the transient bicontinuous structure was formed in Section 6.4.1.

Based on these observations, we believe that a bicontinuous structure forms during or immediately after mixing. For the particle-free case, the structure evolves quickly into a droplet-matrix morphology. If the particle loading is sufficient, the particle adsorption amount is high enough to partially stabilize the bicontinuous structure initially formed. We presume that interfacial particle jamming stabilizes these "particle-assisted network structures".
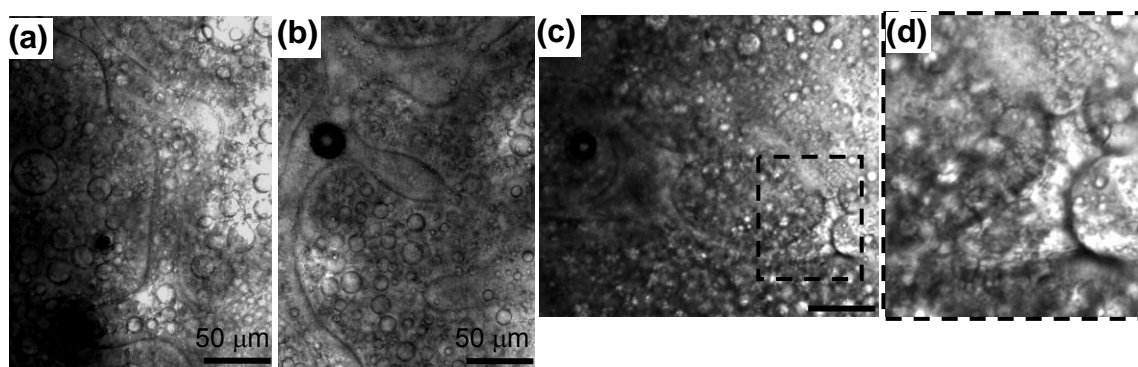
Figure 60. Transient network structure of sample PI50_0 in a Petri dish.

The denoted area in figure c was magnified in d to show the characteristic "neck" structure for a bicontinuous morphology. The scale bar in a, b and c is 50 μm.
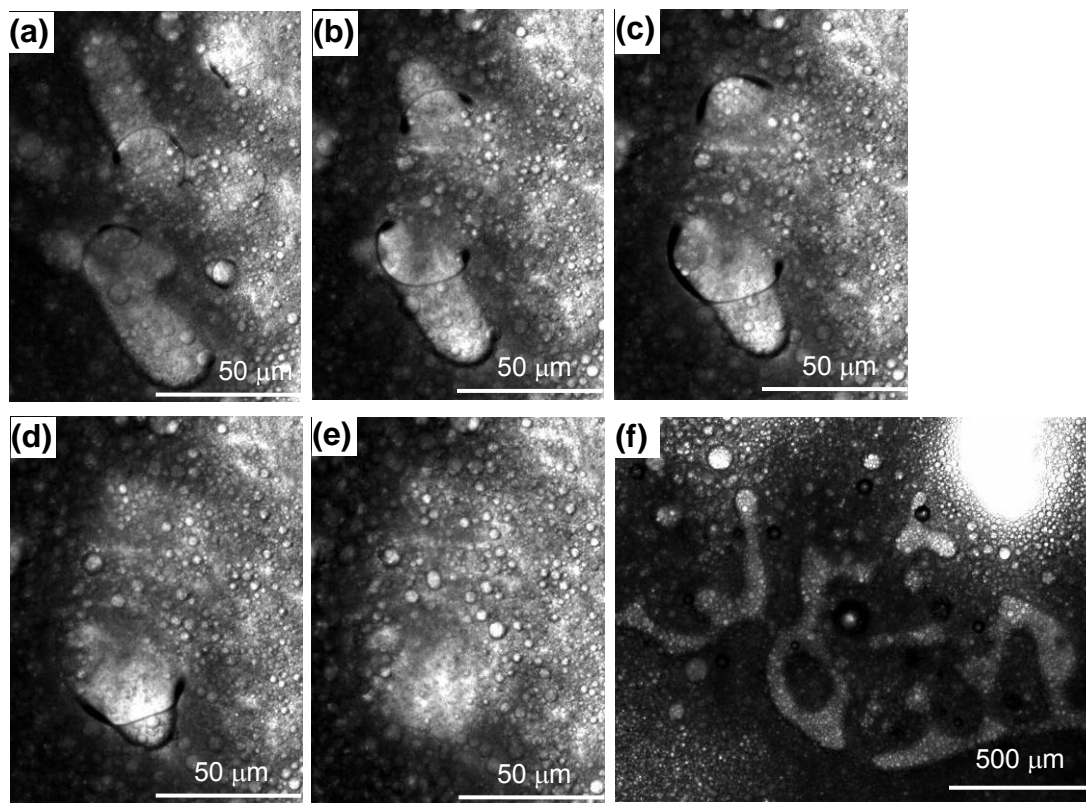
Figure 61. Transient network structures of sample PI40_0 in a Petri dish.

(a-e) A sequence of pictures taken in 1 min shows the disappearance of the transient structure. (f) A transient

network structure.

6.3.2 Phase continuity test

The results of phase continuity test for samples PI60_0 and PI40_0 are presented in this section. We also experimentally determined the phase (i.e. component) of the dark network structures that we found in PI60_8. For PI50_0, the phase continuity result was less reproducible and therefore not presented. This inconsistency may be due to experimental errors resulting from weighing components in sample preparation. Since the composition may be very close to the phase inversion point, the weighing error might be enough to cause inconsistency. Since the

PI50 composition was not the composition of most interest, we did not pursue its phase continuity further.

In Figure 62a, a sharp interface formed between blend sample PI60_0 and the testing liquid silicone oil, which was miscible with PDMS component. We therefore know that the matrix phase is PI for PI60_0. In Figure 62b, we further confirmed that PI is the continuous phase because the blend sample released drops when it was immersed in mineral oil, which was miscible with PI.
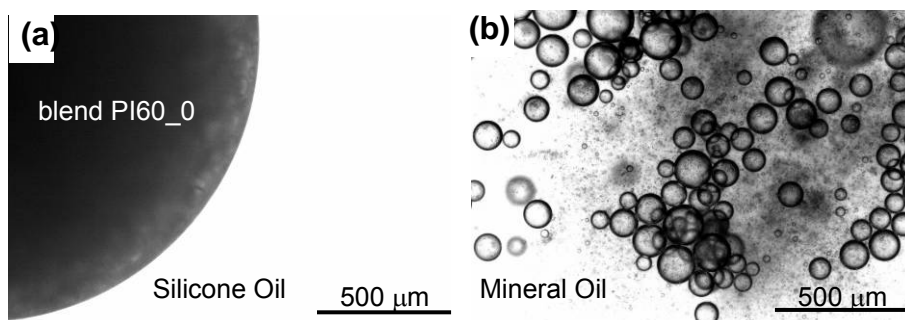
Figure 62. Phase continuity test for sample PI60_0.

(a) A sharp interface formed when immersed in silicone oil. (b) Matrix dissolved and drops were released into mineral oil. Both concluded that continuous phase is PI for PI60_0.

In Figure 63a, the blend sample PI40_0 released PI drops when it was immersed in silicone oil (low Mw PDMS), while a sharp interface was evident when it was immersed in mineral oil. Therefore, we know that the matrix phase of PI40_0 is PDMS.
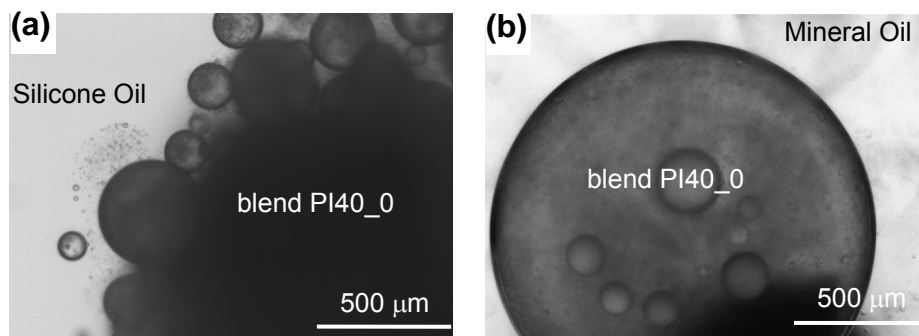
Figure 63. Phase continuity test on sample PI40_0.

(a) Matrix dissolved and drops were released into silicone oil. (b) A sharp interface formed when immersed in mineral oil. Both concluded that continuous phase is PDMS for PI40_0.

In addition, we also performed the phase continuity test on particle-containing samples, PI60_0.25, PI60_2, PI60_4, PI60_8 and PI40_8 (results not shown), in order to know if the presence of particles would change the phase continuity. In other words, we wanted to know if particles cause a shift of phase inversion point[79]. The results indicated that the particle-containing samples have the same phase continuity with the corresponding particle-free samples.

Furthermore, we modified slightly the phase continuity test method as mentioned in Section 6.2.2 to determine the phase of the dark network structure in PI60_8. A lump of blend sample on the metal wire would be too dark to observe the network structure, and the stress applied during placing the sample on wire may also affect the network structure. Therefore, we performed the test on a substrate (polystyrene Petri dish surface) in order to observe the network structure during the contact of testing liquids.

We first used low molecular weight PDMS to contact the blend. In Figure 64a and its magnified and enhanced image Figure 64b, low Mw PDMS was spreading downwards in the image. Note that the blend PI60_8 had a wetting layer on the contact line of substrate-air-blend. The contact of PDMS with this wetting layer left no interface behind, so we know that the

150

wetting layer was composed of PDMS. A particle monolayer seemed to cover most area of the blend. In Figure 64c and d, the spreading of PDMS on top of the blend sample barely affected the network structure, suggesting that a wetting layer and particle monolayer may again serve as the barrier layers at the blend-air contact surface.

We then used pure PI to contact the blend. In Figure 64e and f, as pure PI spread on the substrate (upwards in the image), it pushed the PDMS wetting layer to move together. Any PDMS material left by the wetting layer deformed into a stream (Figure 64e) and then broke up into a strip of drops due to capillary instability (Figure 64f and g). There was no interface formed between the pure PI (testing liquid) and the matrix of the blend sample. The network structure and other drops suspended in the matrix were intact, but they may slightly shift the location as affected by the flow. A particle monolayer spread at the PI/PDMS interface onto the surface of the moving PI pure polymer (Figure 64g), and we believe that the PDMS wetting layer at the blend-air contact surface spread together although we could not tell the transparent layer from microscopy. Based on these observations, we concluded the structure of the blend PI60_8 on the substrate to be the schematic representation in Figure 64h. Shall we not consider the barrier layers (PDMS wetting layer and particle monolayer), the phase of the dark network structure in PI60_8 was PDMS and the continuous phase was still PI.
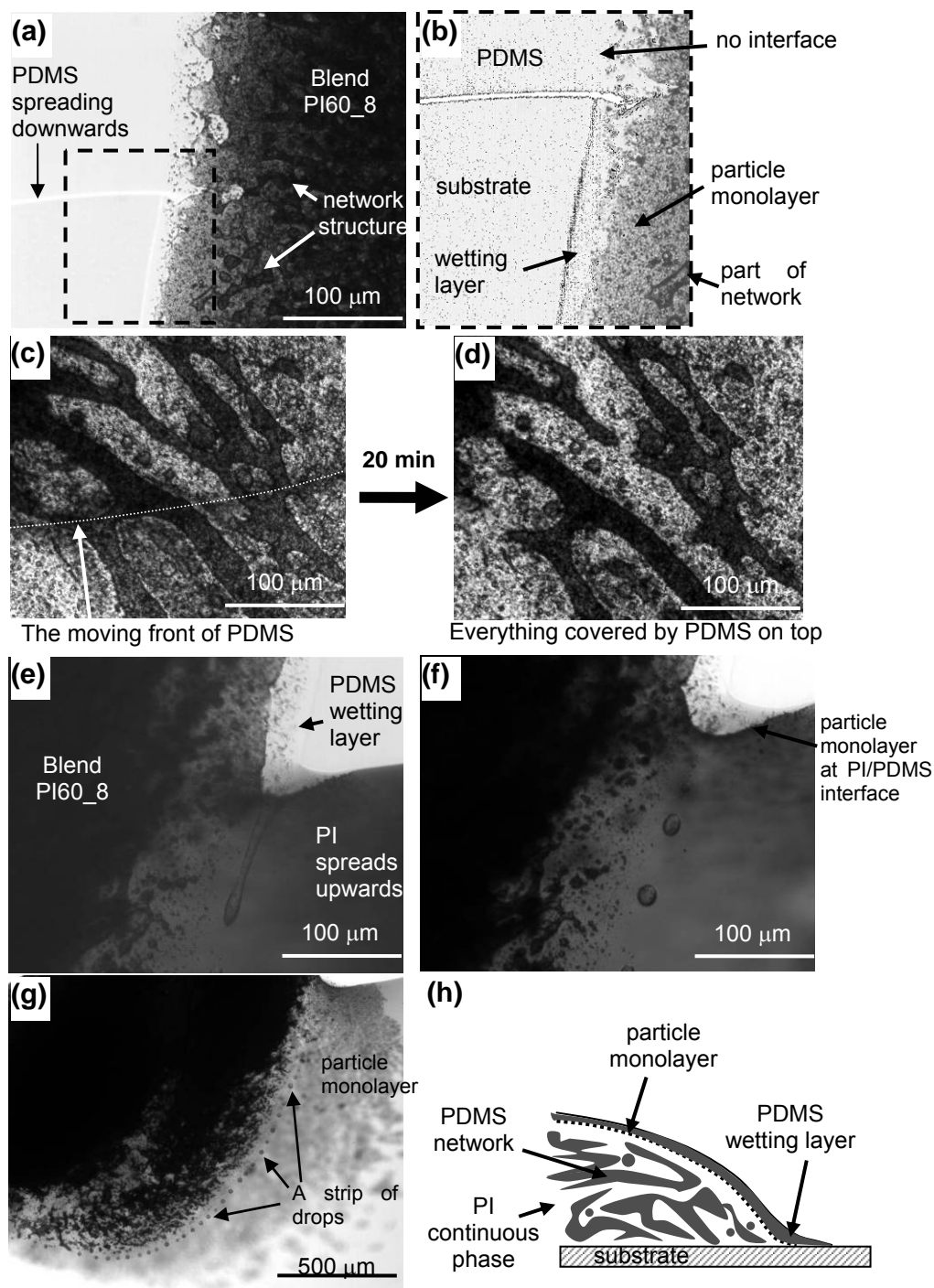
Figure 64. Phase continuity test of sample PI60_8 on a substrate.

(a) PDMS spreads downward on substrate surface. (b) Magnified and image enhanced micrograph for the denoted

area in figure a. (c)(d) The PDMS spreads on top of blend surface did not affect the network structure. (e) (f) (g) PI

spreads upward in the picture. The wetting PDMS layer forms a strip of PDMS drops. Particle monolayer spread on

PI probably with the wetting PDMS layer. (h) Proposed structure of PI60_8 on a substrate.

6.3.3   Flow-induced morphology and rheology of blends with various particle loadings

In this section, we try to correlate the shear cell visualization with the rheological measurements. We should first note the differences between them. The shear cell uses the parallel-plate geometry. The shear rate and shear stress is radius-dependent. Therefore, it provides local morphology information. On the other hand, we used the cone and plate geometry in the stress controlled rheometer. The shear stress and shear rate are uniform across the radius, but the gap is a linear function of radius.

For a droplet-matrix morphology, the velocity field determines the traveling speed of drops and thus the drop collision frequency when drop volume and number of drops are fixed. Figure 65 compares the two geometries and their gap. Table 10 summarizes the shear rate information for the shear cell at two different radii and the steady-state shear rate information for the four creep steps in rheometer for different samples. Although there are only two steady shear steps in the shear cell but four creep steps in the rheometer, the shear rates are considered comparable. The shear stresses are both in the stepping down fashion, which rationalizes the comparison.

$$v_{max}(r) = \dot{\gamma}(r) * Z_{Gap} \qquad v_{max}(r) = \dot{\gamma} * Z_{Gap}(r)$$
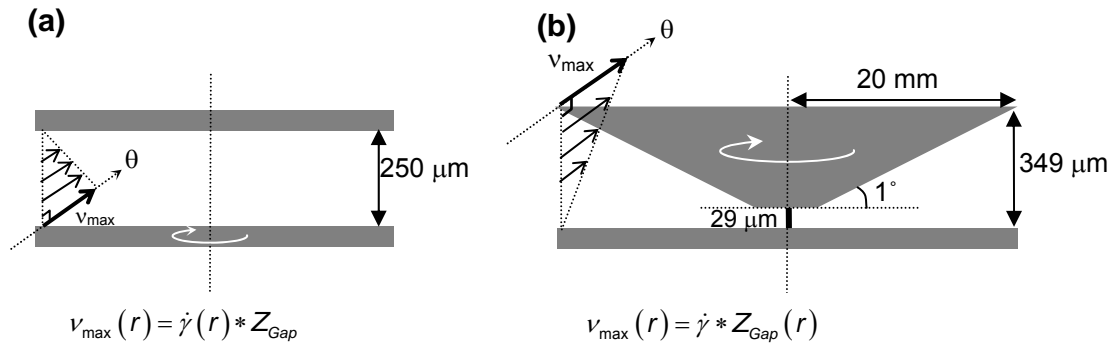
Figure 65. Geometry comparison between (a) the parallel plates and (b) the cone and plate. The maximum velocity is a function of radius. The shear rate in parallel plates and the gap in cone and plate are also functions of radius.

Table 11. The shear rates for the shear cell at different radii and the shear rates of blend samples PI60_0, PI60_2 and PI60_8 for the four creep steps in a rheometer.

	Shear cell @4mm-radius	Shear cell @8mm-radius		Steady-state shear rate (each step 2000 s.u.)		
				PI60_0	PI60_2	PI60_8
Step 1 shear rate; strain unit	$1.5\ s^{-1}$ 1500 s.u.	$3\ s^{-1}$ 3000 s.u.	Creep 1	$2.4\ s^{-1}$	$2.23\ s^{-1}$	$2.05\ s^{-1}$
			Creep 2	$1.0\ s^{-1}$	$0.90\ s^{-1}$	$0.82\ s^{-1}$
Step 2 shear rate; strain unit	$0.325\ s^{-1}$ 1625 s.u.	$0.65\ s^{-1}$ 3250 s.u.	Creep 3	$0.48\ s^{-1}$	$0.39\ s^{-1}$	$0.31\ s^{-1}$
			Creep 4	$0.22\ s^{-1}$	$0.16\ s^{-1}$	$0.11\ s^{-1}$

6.3.3.1 Shear cell visualization of blend morphology

In this section, we aim to answer the following question: can flow-induced drop coalescence generate elongated drops that do not relax due to interfacial particle jamming? To address this question, we will compare the morphologies under flow and after flow for several blend samples of increasing particle loadings.

We hypothesize elongated drops to form by two mechanisms: (1) drop/particle collisions can steadily build up particles at the interface until the deformed shape gets jammed; (2) drop/drop coalescence of particle-laden drops decreases the combined interfacial area.

In reality, we speculate that both situations happen and go hand-in-hand to increase the interfacial particle concentration. Meanwhile, the drop breakup event, which tends to decrease the particle concentration at drop surface, can also happen as long as interface is still mobile. The balance between coalescence and breakup continues until a coalescence event increases the interfacial particle concentration to the extent that the interface is not mobile to allow breakup. When the flow stops, those flow-deformed elongated drops with a densely particle-packed

interface cannot retract to spheres. Under those circumstances, we can then observe elongated drops with nonrelaxing drop shapes.

In the following, we compare four blend samples, PI60_0, PI60_2, PI60_4 and PI60_8 at three different stages (i.e. time) of the shear history (see Figure 66). Three stages that we are particularly interested in are: (1) after the first shear step (i.e. the step of 3 s^{-1} shear rate); (2) the end of the second shear step (the step of 0.65 s^{-1} shear rate); (3) at a delay time after the second shear step.

Shear rate = 3 s^{-1}

Total 3000 s.u. @r=8 mm

Shear rate= 0.65 s^{-1}

Total 3250 s.u. @r=8 mm

time

1000 sec

observation

5000 sec
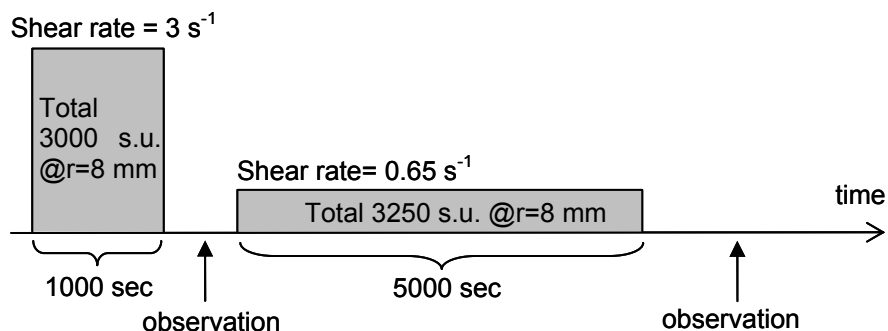
observation

Figure 66. Shear history for samples in the parallel-plate shear cell.

The main focus for the first-stage observation is to observe that drops have broken up into many tiny drops after the high shear. Due to the complication of the network structures found in PI60_4 and PI60_8, we should also verify that after the high shear, the morphology is purely a droplet-matrix morphology. The purpose for the second-stage observation is to check if any elongated drop is present. The purpose for the third-stage observation is to see if any elongated drop observed in the second-stage observation can persist without retraction and thus prove that interfacial particle jamming may have occurred as promoted by drop coalescence under the flow conditions.

Figure 67 shows the comparison after the cessation of the first shear step for four blend samples, PI60_0, PI60_2, PI60_4 and PI60_8 at both radius=8 mm and 4 mm. The shear stress at 8 mm is the double of the stress at 4 mm. All of the morphologies in Figure 67 are confirmed to be droplet-matrix. In Figure 67a and e, the drop size distribution is bi-disperse. There are less-than-20 μm-sized small drops, and ca 50 μm-sized drops. The larger drops formed from the breakup of a circular string due to capillary instability, and the circular strings were only present under flow for the particle-free sample. The formation of strings might be due to drop coalescence under flow or due to the presence of a large drop in the initial sample. We believe that if the strings could break up, they did not stick to the glass surface. We also checked the relative motion of drops and strings with respect to the image during shearing to make sure that the object of interest under observation is under the flow (instead of sticking to glass).

The elongated drops in Figure 67d also formed from the breakup of circular strings which were present during shearing. However, because the string surface might be coated by particles (evidence later), the kinetics of breakup may be affected. In Figure 67h, a presumably particle-coated string sustained for a longer time than the particle-free strings (not shown). When the presumably particle-coated strings broke up into drops (see Figure 67d), the drops may or may not fully retract to spherical shapes.

Figure 68 shows the comparison at the end of the second shear step (see Figure 66 for the shear history) for samples PI60_0, PI60_2, PI60_4 and PI60_8 at both radius=8 mm and 4 mm. All of the micrographs in Figure 68 were taken immediately after the cessation of shear with only two exceptions, which are Figure 68c and g. Micrographs of Figure 68c and g were taken near the end of the second shear step, and therefore show the small deformed drops. The large drops that we saw in Figure 67 (a, b, c, d, e, f and h) could rejoin to form the circular strings. The particle-free strings however did not survive from the repeated shearing and disappeared at

156

the observation location. Only particle-containing samples (Figure 68b, c, d, f and h) have the strings at the end of the second shear step, which implies that the presence of particles have contributed to the stability of strings, either by interfacial contribution or/and by bulk contribution. The darker outlines of drops and of strings in Figure 68b, c, f and g suggest particle adsorption at the interface. Because pictures in Figure 68d and h were taken in reflection mode (surface illumination), the drops do not have darker outlines but instead appear bright white in reflection. Note that there are numerous elongated drops in Figure 68d and h. The arrows point out a few examples. We will discuss the retraction kinetics of these elongated drops later.

Figure 67, Figure 68 and Figure 69 are organized as such the comparison in time sequence (end of 1st shear step, end of 2nd shear step, and at a delay time after the 2nd shear step) is also possible. However, we note that there might be minor position errors on tuning the observation locations (where the center of picture is at 8 mm or 4 mm) because we moved the customized microscope on a manual microstage. The positions of strings were also not fixed because strings may break up into drops under the shear stress of flow and new strings may also form from drop coalescence. Nevertheless, sometimes the locations of strings and large drops are highly correlated among Figure 67, Figure 68 and Figure 69.

Figure 69 shows the comparison at a delay time after the second shear step again for four samples at two radii. The delay time is noted for each picture. As we compare Figure 68b with Figure 69b, and Figure 68f with Figure 69f, we can tell that strings broke into drops. The "lemon-shaped" drop in Figure 69b is particularly interesting, and we will discuss its retraction in Figure 70. While some elongated drops from Figure 68d and h were able to maintain their shapes at the delay time (arrows pointing at a few examples in Figure 69d and h), most of other small drops in Figure 69 are spherical. More details are discussed in Figure 71.

157
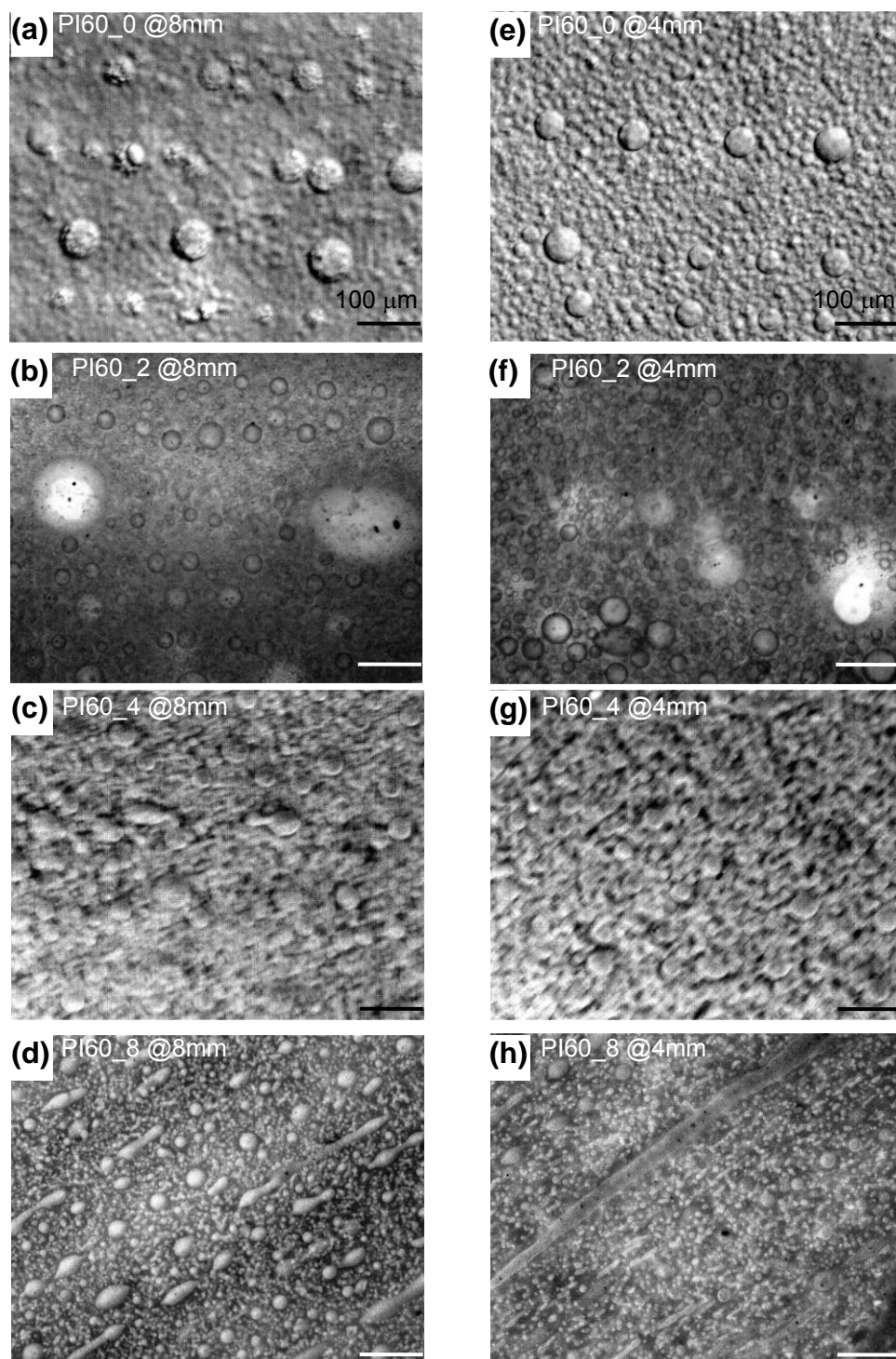
Figure 67. Comparison of four PI/PDMS blend samples at two radii after the first shear step.

The four blend samples in the shear cell are PI60_0, PI60_2, PI60_4 and PI60_8.

(a-d) at radius of 8 mm; (e-h) at radius of 4 mm. The scale bars are 100 μm.

158
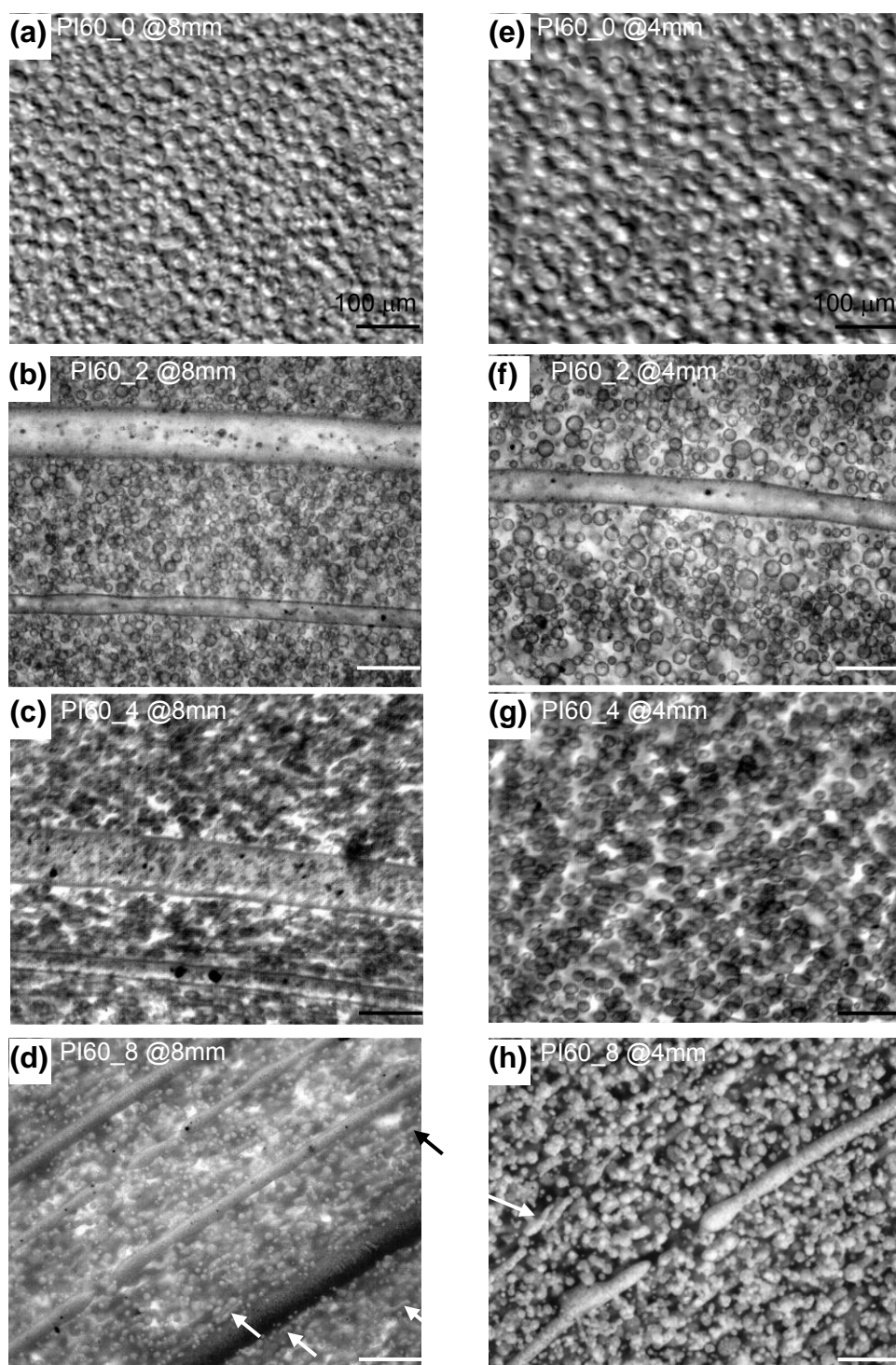
Figure 68. Comparison of four PI/PDMS blend samples at two radii at the end of the second shear step.

The four blend samples in the shear cell are PI60_0, PI60_2, PI60_4 and PI60_8.

(a-d) at radius of 8 mm; (e-h) at radius of 4 mm. The scale bars are 100 μm.
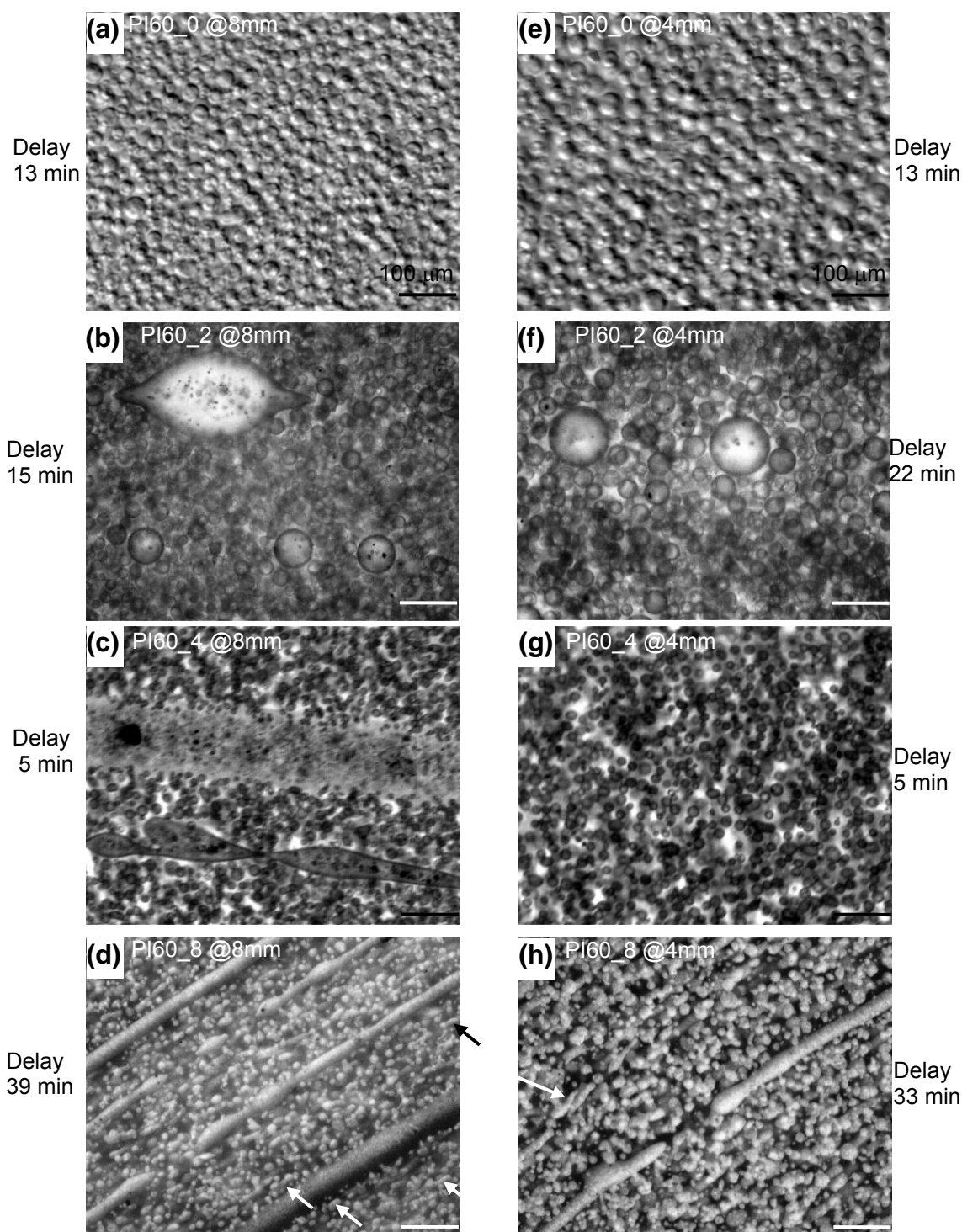
Figure 69. Comparison of four PI/PDMS blend samples at two radii at a delay time after the second shear step. The four blend samples in the shear cell are PI60_0, PI60_2, PI60_4 and PI60_8. (a-d) at radius of 8 mm; (e-h) at radius of 4 mm. The delay time are noted for each graph. The scale bars are 100 μm.

160

Figure 70 shows the time sequence of the breakup the two strings in Figure 68b. The first micrograph (Figure 70a) was taken during shearing, so the drops were deformed. As the shear stopped (time~0 sec), the small deformed drops in the inset of Figure 69b retracted back to spheres (Figure 69c) within 1 min. The thinner string also has developed the pinched points of capillary instability from Figure 69b to c (marked by the white arrows). Capillary instability arises because as a string breaks into drops with a finite wavelength (i.e. spacing), the total surface area of drops is smaller than that of a string. The thinner the string is, the more the interfacial energy reduces and thus a larger driving force. The observation is consistent with this expectation. The inconsistent spacing between the big drops in Figure 70d and e is probably because the thin string did not have a uniform diameter before the instability breakup process started. Later in the time sequence, the primary string broke up in Figure 70f. The retraction of the "lemon-shaped" drop was particularly slow, and never completely back to a sphere. The sharp tip of the drop was still present after 19 hr observation. We believe that only interfacial effect due to particle jamming can stop drop retraction; bulk effect can only slow down the retraction but not stop it. In addition, the interior of the drop appeared bright and contained few particles, while the outlines of drops were darker. Therefore, we presumed that the delayed (as compared to particle-free) capillary instability was caused by particle adsorption on the string surface. The presence of a sharp tip of a drop showed that the nonrelaxation behavior was very localized and persistent (~19 hr), which suggested interfacial particle jamming.

161
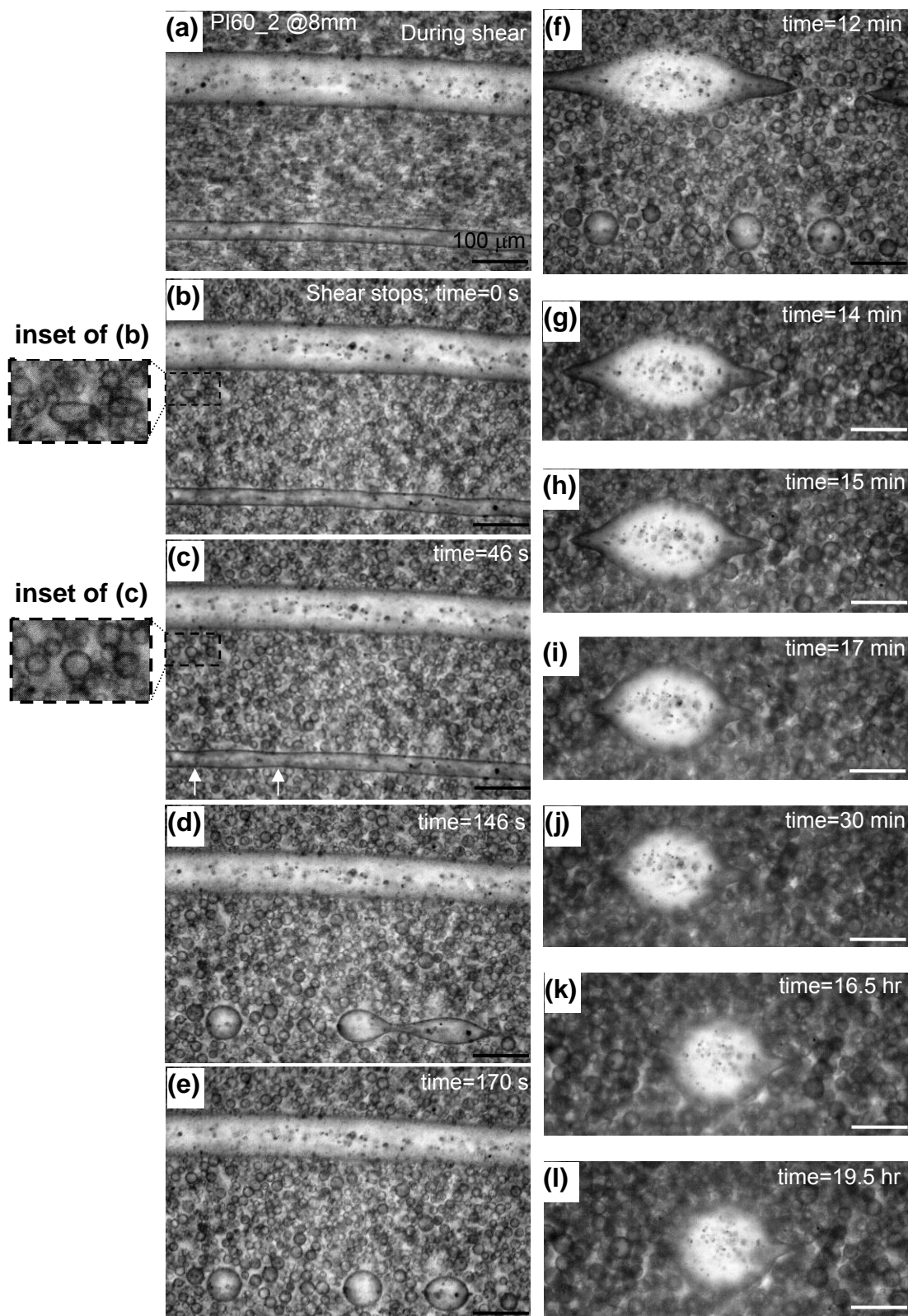
Figure 70. Instability of strings and drop retraction in blend PI60_2 in the shear cell at radius of 8 mm.

Note the presence of a tip to the right of the drop at time=19.5 hr after the shear. The scale bars are 100 μm.

Figure 71 shows the non-relaxing behavior of small drops which did not form from the breakup of strings in sample PI60_8 at radius of 4 mm after the second shear step. Besides many tiny round drops, there were several examples of elongated objects in Figure 71. We circle a few examples in Figure 71b. The elongated drops did not retract after the 16 hr observation time. Thus, we know that the presence of particles at this particle loading (8 wt%) has great impact on drop retraction kinetics. We presumed that the non-retraction behavior is caused by interfacial jamming (discussed in Section 6.4.2). Each of these tiny nonrelaxing events is expected to contribute to a change in the elastic recovery of the polymer blend and thus have a great impact overall. Since the elongated drops formed from drop coalescence, repeated shearing or shearing for a longer period of time should promote drop coalescence and generate more elongated drops.
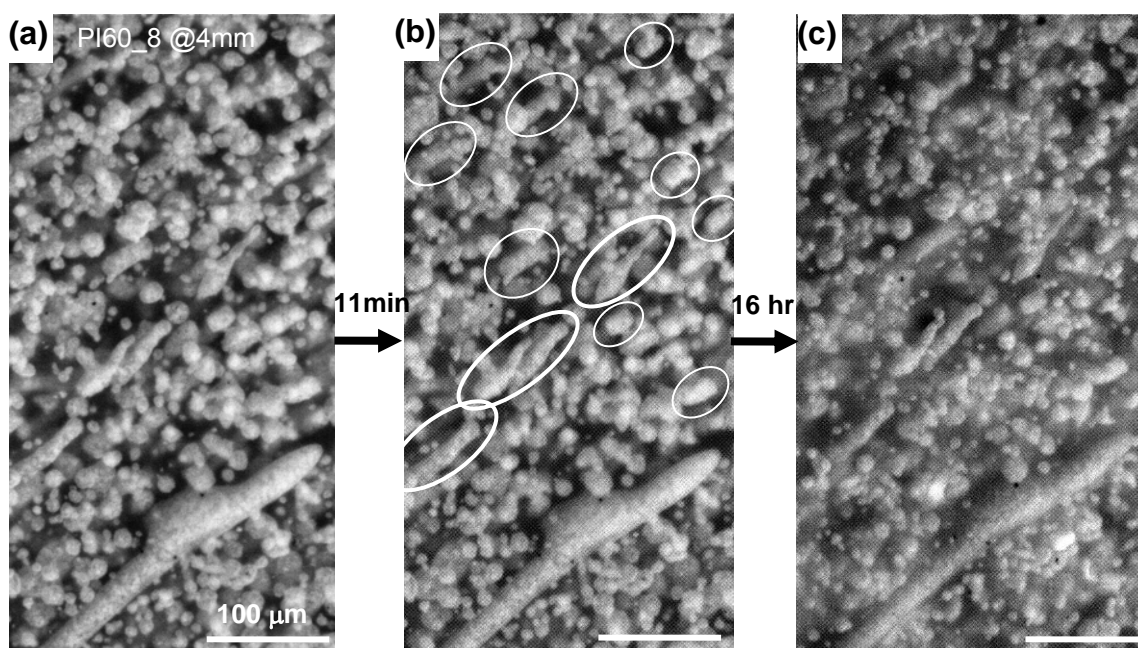
Figure 71. Nonrelaxing behavior of elongated drops in blend PI60_8 in the shear cell at radius of 4 mm. Circles point out some examples of elongated drops. The scale bars are 100 μm.

6.3.3.2 Rheological measurements of blends

We present the rheological results based on the four-step shear history (see Figure 72, the next page) for the FeOOH particles/PI/PDMS blends. Three issues must be noted. Firstly, rheological measurements provide us "averaged" information over the entire sample. It would be difficult to interpret the rheological data of a sample with morphological heterogeneity.

Secondly, the events of string breakup may complicate the interpretation of results. In some sense, we can consider a string as an ultimately long drop generated from numerous drop coalescence events. Until the pinching-off moment of the strings, we "do not" expect that the presence of strings affects the elastic recovery of blends. Once pinching occurs, the retraction of the newly-generated "daughter" drops may or may not have a profound impact on the strain recovery. If the daughter drops are small (compared to the volume of a sample) and exactly parallel to the flow, the symmetry of the drop should cancel out the strain recovery. Otherwise, it may have profound impact in the strain recovery of blends.

Last but not least, current knowledge of elastic recovery of immiscible polymer blends is mostly based on particle-free or copolymer-compatibilized blends. To the best of our knowledge, only one research[80] have studied the elastic recovery of particle-compatibilized blends. Interfacial particle jamming has never been taken into consideration. From the visualization (Section 6.3.3.1), we have established that the presence of particles at a sufficient amount (e.g. 8 wt%) has a great impact on the kinetics of drop retraction. We expect that the elastic recovery of blends must be greatly affected. Therefore, our task of correlating "interfacial" rheology and particle jamming[81] is important and challenging since the presence of particles at interface or in bulk is expected to complicate the drop behavior in immiscible polymer blends.[57]

In the following, we present the data in the same sequence of the shear history in a single cycle. The sequence is: (1) creep for 2000 strain units at the desired stress level; (2) recovery; (3) oscillatory. The viscosity measurement in the creep step and its stress dependence will be discussed first. Then, we discuss the strain recovery of blends in the recovery step. Last, we cover the storage modulus, loss modulus and complex viscosity measurements in the oscillatory frequency sweep step.
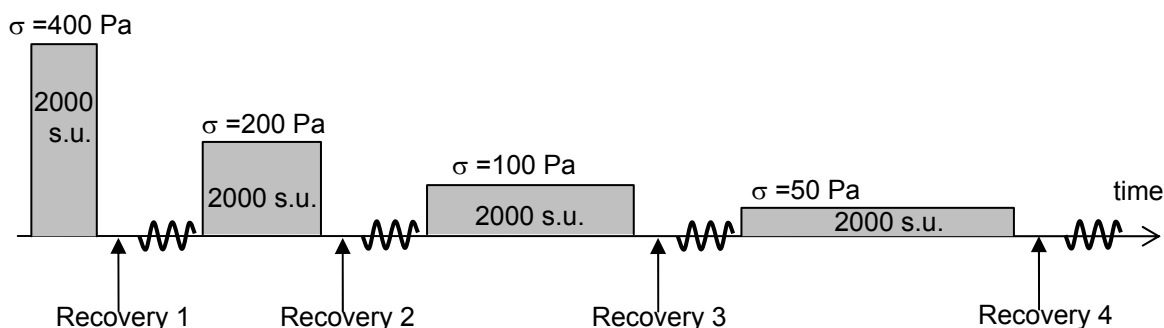
Figure 72. Shear history for samples in the rheometer using a cone and plate geometry.

The creep steps in the rheometer serve the same function to the steady-shear steps in the shear cell visualization. Figure 73a shows the raw data of viscosity measurements in creep steps for the particle-free blend PI60_0. Instead of showing the time axis as log(time) as we usually do, we choose to show the linear time axis to give information of the durations of each step (778, 1950, 4162 and 9109 sec). Each step corresponds to 2000 strain unit. This shear history is qualitatively comparable to the shear history that we applied in the shear cell (i.e. stepdown fashion, strain unit, shear rate and time duration).

During the creep step, we expect that drops continue to coalesce and break up during this period until a steady state is reached. Figure 73b plots the steady-state viscosity vs. shear stress

165

in order to show the stress-dependent behavior. We compare particle-free blend (PI60_0) with
particle-containing blends (PI60_0.25, PI60_2 and PI60_8).
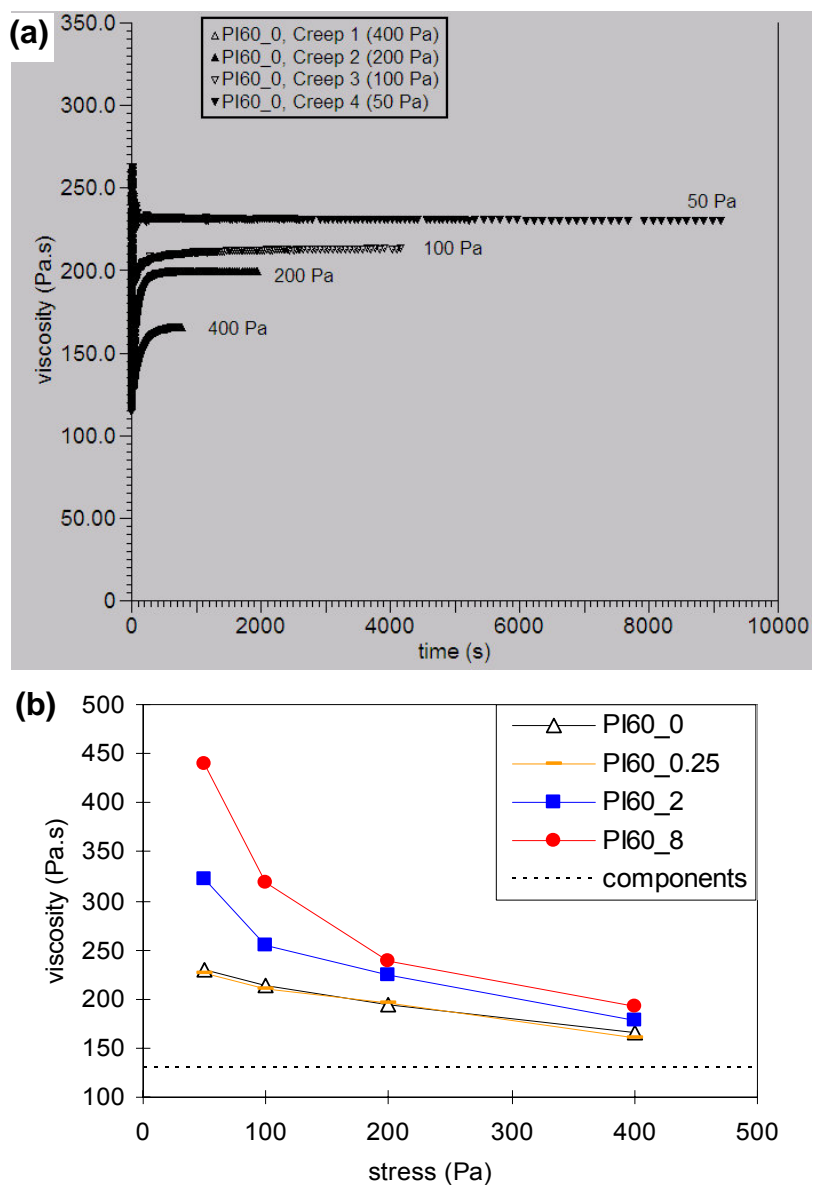
Figure 73. Steady state viscosity measurements for PI60_0, and the shear thinning behavior of PI/PDMS blends.

(a) Viscosity measurements in the creep steps of different shear stress. The time duration of each step is different but

the total strain unit is the same. (b) Shear thinning behavior of blends

166

In Figure 73b, all of the blends show a shear thinning behavior, while the viscosities and the extent of shear thinning increase with particle loading. The possible reasons are two: interfacial effect or bulk effect. For the interfacial effect, as more particles adsorb at the drop surface, the interface may become more rigid. A rigid drop is less easy to deform and shows high viscosity at low stress. This can explain the greater extent of shear thinning as the particle loading increases. For the bulk effect, if not all the particles are adsorbed at the interface, the particles left in the PI component can associate with each other as mentioned in Section 5.3.1 (see Figure 36). Furthermore, the free particles in the bulk can also associate with particles at the drop surfaces and thus generate clusters of drops sticking together. Figure 74 shows an example of sticking drops found portion of PI60_4 in a Petri dish. A continuous shear may break the agglomerate of particles or drop clusters. The association of particles is concentration dependent. This can also explain the greater extent of shear thinning behavior for high particle loading samples. At this stage, we do not know which effect dominates the shear thinning behavior. It could also be a combination effect (i.e. some drops are sticking together and some drops is rigid on interface). A comprehensive discussion about which effect is more important on controlling blend morphologies is provided in Section 6.4.2 after we collect all of the necessary information.
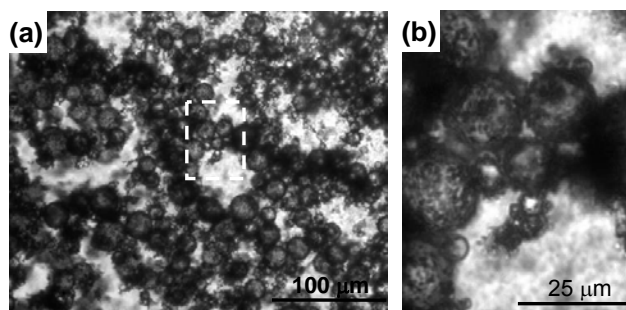
Figure 74. Drops sticking together due to particle-particle association.

(a) Sticking drops found in some region of PI60_4 in a Petri dish. (b) The magnified micrograph for the denoted area in figure a.

167

Next, we discuss the strain recovery after each creep step (400, 200, 100 and 50 Pa) for blend samples PI60_0, PI60_0.25, PI60_2, PI60_4 and PI60_8. For a given droplet-matrix morphology, a higher shear stress results in larger extent of drop deformation, and thus the ultimate strain recovery of a blend is expected to be larger. A complication comes from the fact that the morphology can change (e.g. change in drop size) during the shear history. Therefore, we need to use the particle-free blend to serve as the reference for strain recovery of each step.

Figure 75 shows the strain recovery after each creep step for PI60_0, PI60_0.25, PI60_2, PI60_4 and PI60_8. As compared to particle-free blend PI60_0, blend sample PI60_0.25 behaves essentially identical in strain recovery and PI60_2 also have similar behavior in strain recovery. This suggests that the strain recovery would not be affected much if the particle loading is low. The notable feature of PI60_4 and PI60_8 is that the recovery after 50 Pa has both a smaller ultimate recovery (γ_∞) and slower kinetics.

The semi-log plot for PI60_8 in Figure 76b shows the strain recovery value more clearly. As compared to the particle-free blend (Figure 76a), the strain recovery of PI60_8 in each recovery step is both smaller in absolute values and slower in kinetics (i.e. curves are extended in the time axis). This suggests that the drops (or some of the drops) cannot relax to the full extent, especially after a long shear history. This result is consistent with the findings of shear cell visualization: some elongated drops found in sample PI60_8 cannot relax their shapes over time upon cessation of shear flow (Figure 71).
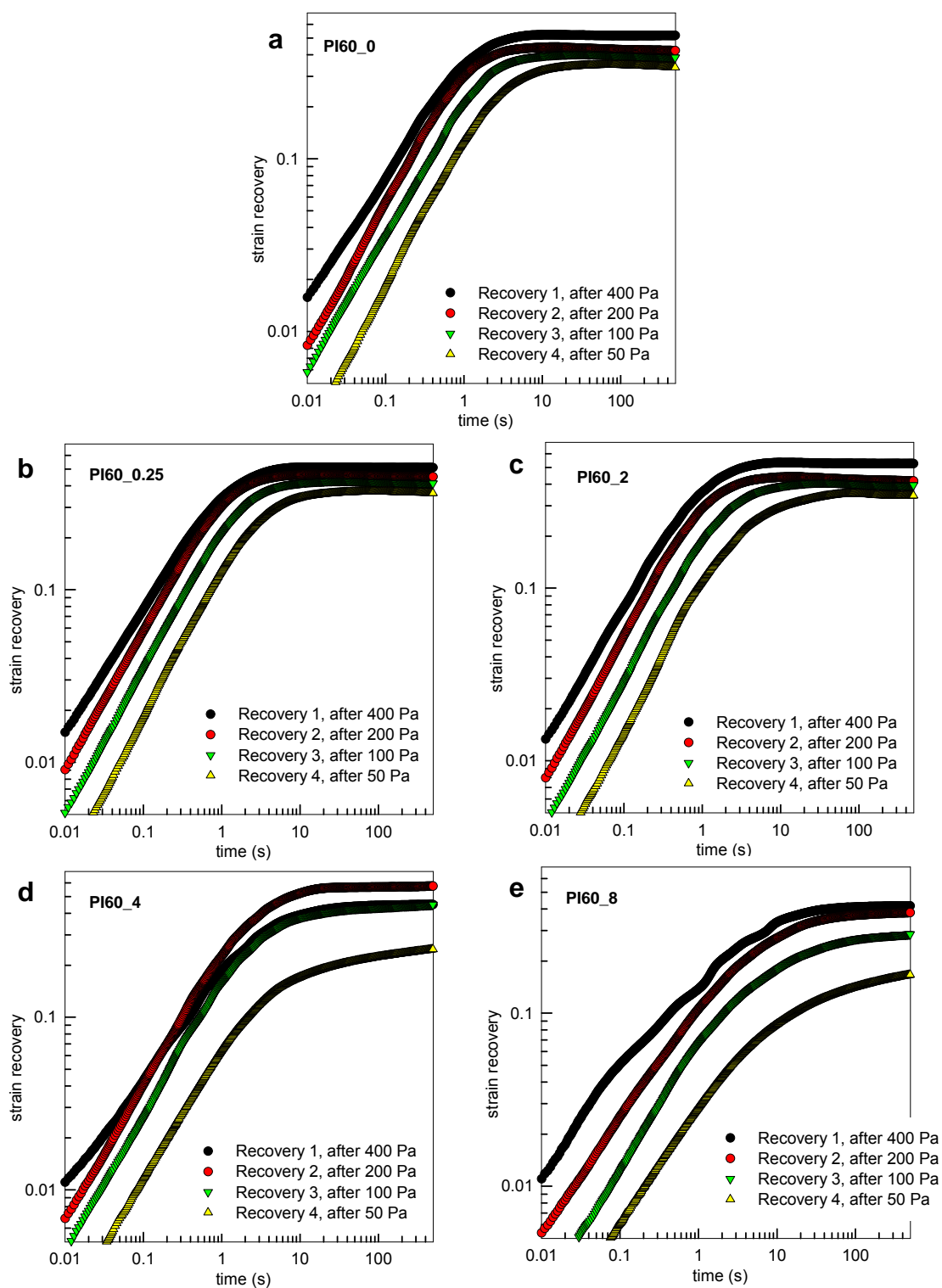
Figure 75. Log-log plot of strain recovery versus time for different PI/PDMS blend samples.

(a) PI60_0 (b) PI60_0.25 (c) PI60_2 (d) PI60_4 (e) PI60_8

In Figure 76c, the comparison of the strain recovery of step 4 for blends with various particle loadings suggests that as particle loading increases above certain threshold, strain recovery behaviors would be affected. However, we are cautious to draw a firm conclusion because inconsistency does exist for PI60_4. Its four recovery curves do not fully follow the trend of decreasing strain (Figure75d), which probably means that morphology heterogeneity such as sticking drops or some other effects such as the breakup of strings may have affected the elastic recovery behavior.
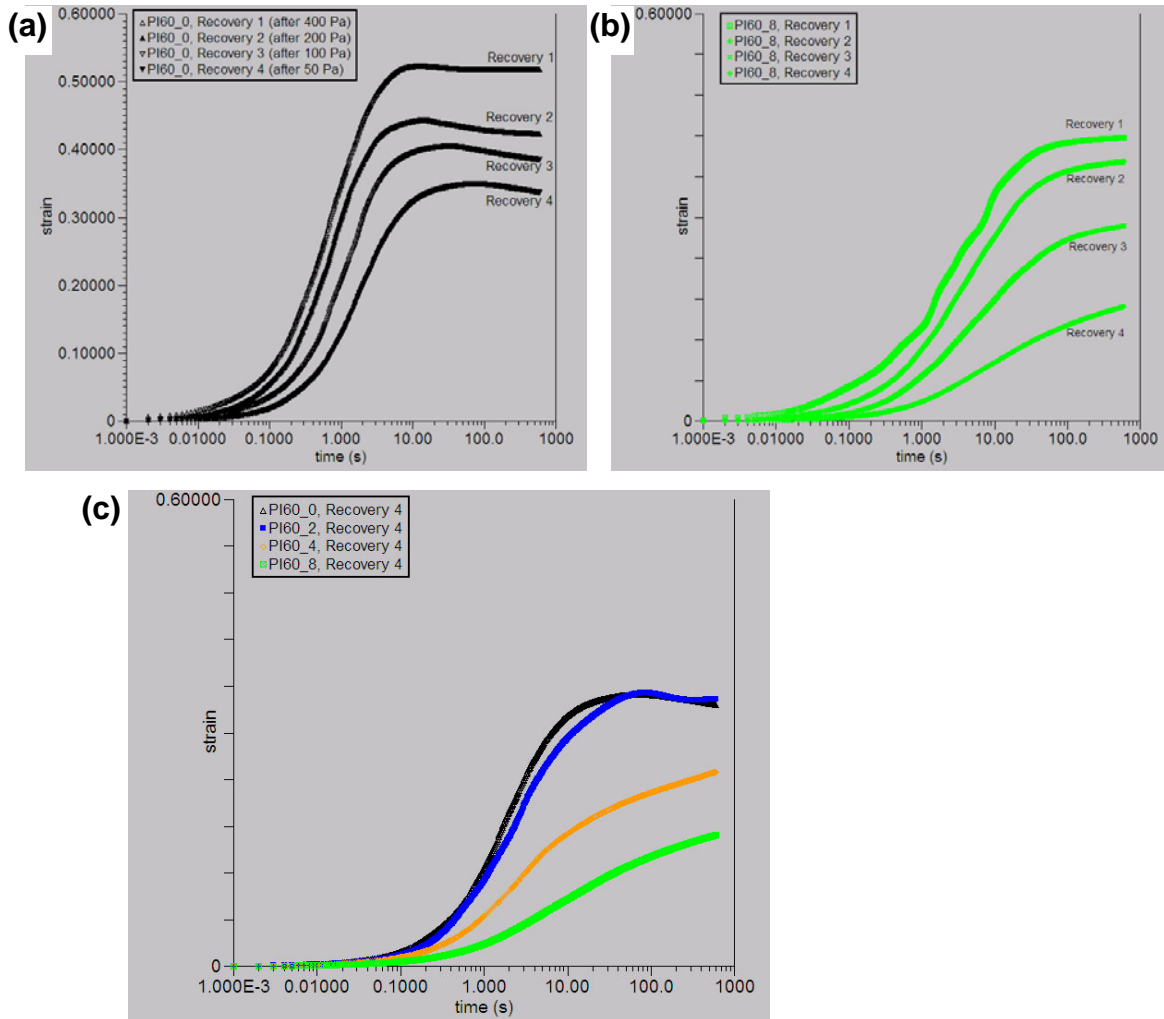
Figure 76. Semi-log plot of strain recovery versus time for different PI/PDMS blend samples. (a-b) Semi-log plot of strain recovery versus time for PI60_0 and PI60_8. (c) Comparison of strain recovery in semi-log plot for samples of various particle loadings after the creep step of stress=50 Pa.

170

The dynamic oscillatory behaviors of blends are shown in Figure 77 and Figure 78. While Figure 77 shows all of the four storage modulus (G') curves and complex viscosity (η^*) curves of each frequency sweep step and thus provides more information, we re-plot the G' curves for the first and fourth frequency sweep step in Figure 78 in order to show clearly the trend of shoulder shift for each sample. For the G' curves in Figure 77, the lowest particle loading blend, PI60_0.25, has almost identical results with PI60_0. As particle loading increases, the absolute G' values increase. For G' curves, the shoulder shift toward the lower frequency means the growth of the mean drop size. The G' shoulder shifts slightly less for PI60_2 than for PI60_0.25 (see Figure 78 for a qualitative shoulder shift). This can also be judged by the value difference between the first and the fourth frequency sweep at about 2 rad/s frequency. The G' curves of PI60_4 nearly overlap at the shoulder, indicating the drop size does not grow through the shear history. For PI60_8, the plateau of the first G' curve at the low frequency indicates a gel-like or nonrelaxing behavior. Two possible reasons come from: (1) nonrelaxing elongated drops; (2) drops sticking together. The disappearance of a clear G' shoulder suggested the first reason is more likely. We are not 100% sure about the reason based on the data. However, since we did not observe any drop sticking together under the flow condition in the shear cell experiment, we presume that this plateau is probably attributed by the nonrelaxation behavior of the elongated drops. This is consistent with the fact that PI60_8 is the only sample that showed elongated drops after cessation of flow.

For the complex viscosity curves, PI60_0 and PI60_0.25 have a plateau at the low frequency region, indicating the structures are able to relax. As the particle loading increases, the complex viscosity values at the low frequency increase dramatically while the viscosity at 100 rad/s frequency for all of the blends are comparable (between 113~140 Pa.s). In a broad

sense, this is consistent with the greater extent of shear thinning behavior for high particle loading samples that we mentioned earlier this section.

To summarize this section, the rheological measurements showed that: (1) there is a greater shearing thinning behavior for high particle loading samples; (2) there is a smaller extent and a slower kinetics of strain recovery for PI60_8; we presume the inconsistency in the elastic recovery for PI60_4 may result from the complication of string breakup or drops sticking together; (3) Data for PI60_4 suggests that it is possible to stop drop growth in the flow condition when the particle loading is sufficient. As suggested by the disappearance of G' shoulders and the plateau at low frequency, drops in PI60_8 may not be able to relax like the drops in PI60_0.
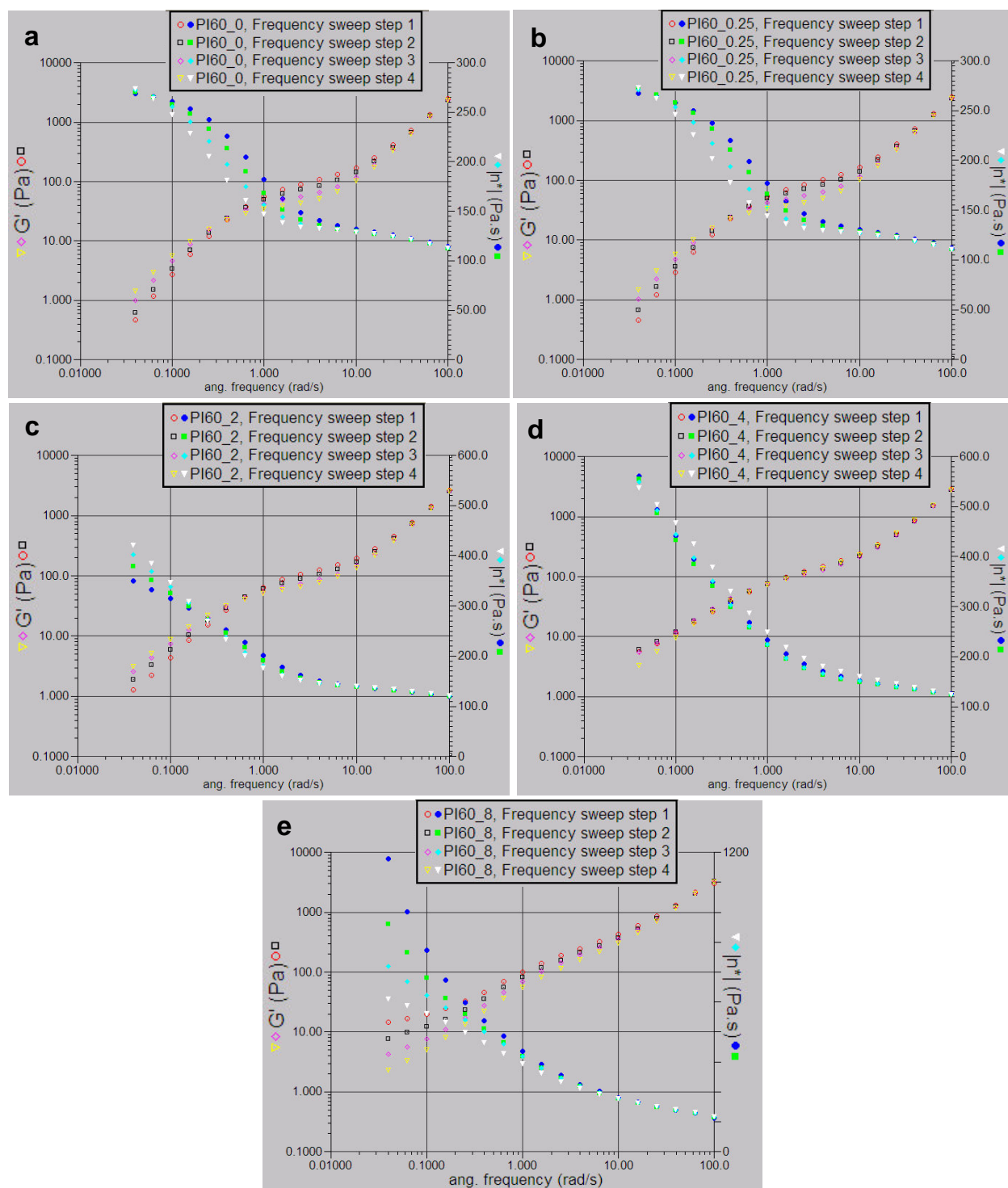
Figure 77. Dynamic oscillatory behavior of the PI/PDMS blends with different particle loadings.

(a) PI60_0 (b) PI60_0.25 (c) PI60_2 (d) PI60_4 (e) PI60_8.
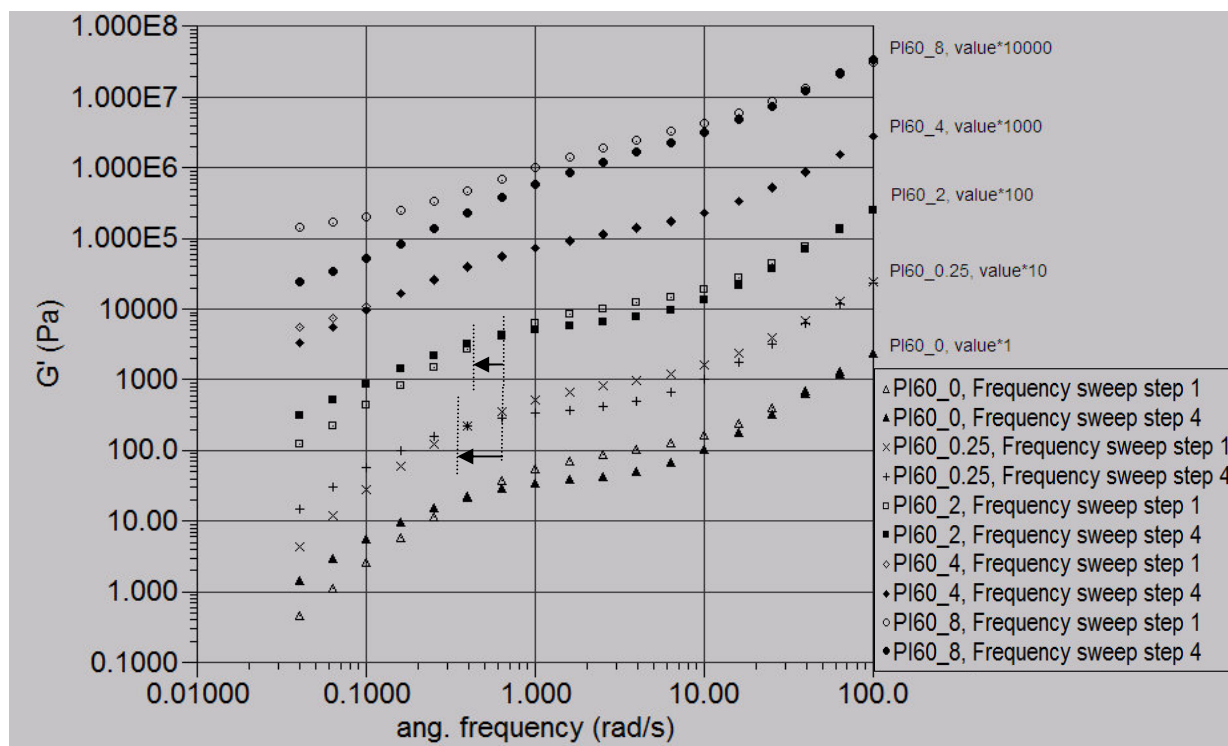
Figure 78. The G' curves measured in dynamic oscillatory for PI/PDMS blends of various particle loadings.

Note the curves of particle-containing blends were shifted upwards by integer orders noted on the side.

6.4   DISCUSSION

6.4.1   Transient network structures in particle-free blends and particle-assisted network structures

In Section 6.3.1, we showed the stable droplet-matrix morphology and the transient bicontinuous morphology immediately after blending for the particle-free PI/PDMS blends. In this section, we discuss the formation, the loss and the stabilization of this transient bicontinuous structure. We will also compare the PI/PDMS system (chapter 6) to the PI/PIB system (chapter 5).

174

Our hypothesis and reasoning is described in the following. Since the components are immiscible, numerous droplets form under the shear stress of blending. The shear stress applied determines the steady-state drop size, which is also the characteristic length scale of a droplet-matrix morphology. Any drop coalescence event can always reduce the interfacial area. However, the retraction of any elongated structure such as a dumbbell-shaped drop resulted from the coalescence of two drops may not be permitted under the applied shear stress. We presume that the combination consequences of, (1) random drop coalescence events and (2) no retraction of elongated structures under the applied stress, result in the formation of the bicontinuous structure or transient network structure that we observed immediately after blending.

Upon the cessation of flow and shear stress, the characteristic length scale is no more a fixed value. The fluid retraction of any elongated structure, which is essentially the coarsening process of a bicontinuous structure, occurs very fast as driven by the interfacial tension between PI and PDMS. Thus, the transient network structure of particle-free blends evolves and reverts to a droplet-matrix morphology in the time scale of seconds, resulting in the loss of the transient network structures.

For any immiscible systems, the interfacial tension induces a domain coarsening process (i.e. fluid retraction from thin to thick region), whose time scale for domain growth (τ) is proportional to length scale*viscosity/interfacial tension ($L\eta/\sigma_{AB}$). Since domain coarsening occurs when the applied stress is removed, we consider it as a quasi-quiescent condition because the Reynolds number (Re= $(dL/dt)\rho L/\eta$) of fluid retraction is much less than 1.

$$Re \approx \frac{(10 \text{ μm/s})*(1000 \text{ kg/m}^3)*10 \text{ μm}}{131 \text{ Pa.s}} = 7.6*10^{-10} \ll 1 \qquad (6.1)$$

where we assume that the length scale is 10 μm, and the fluid at the middle of a neck travels 10 μm in a second to merge into the thick part of the bicontinuous structure.

The PI/PDMS system is an immiscible polymer blend system which has relatively large interfacial tension (~2.7 mN/m[74]) as compared to the PI/PIB system (~0.3 mN/m[74]) studied in chapter 5. This results in a fast and untraceable domain coarsening rate in the particle-free blends. In contrast, the PI/PIB system is a partially miscible system with a relatively small interfacial tension. Therefore, it has a traceable domain coarsening rate. In both systems, sufficient particle adsorption at the interface can be used to slow down or nearly cease the domain coarsening rate. However, we believe that the particle adsorption process is different in these two systems.

As mentioned earlier in this section, the network structure of the PI/PDMS system is likely generated by the random drop coalescence. Particles can adsorb at the interface during mixing whenever a particle encounters the interface if the viscous force induced by the flow does not exceed the interfacial force acting upon the particle (i.e. particles do not desorb by the flow). The drops resulted during blending are likely coated with particles. When these particle-coated drops coalesce randomly to form the network structure, interfacial particle jamming is likely to occur and thus stabilize the network structures. The phase continuity tests show that for PI60 composition, both the drops and the dark network structure are composed of PDMS phase. The further support our hypothesis that the network structure is formed by random drop coalescence. In short, we attribute the stabilization of particle-assisted network structures to the interfacial particle jamming.

For the PI/PIB system, we speculate that the demixing via a spinodal decomposition process after the flow-induced mixing generates the bicontinuous morphology. There is essentially no fluid/fluid interface during the blending process. Particles can only adsorb at the interface after the interface is formed. The particle adsorption efficiency is not very high due to

176

the presumed thermodynamic picture of type 2 in Figure 52c (with a small particle adsorption well).

The particle adsorption rate and efficiency for the PI/PDMS system seems to be higher. Enough amounts of particles were able to adsorb within the combination of mixing time (4 min) and domain coarsening time (< 1 min). Also, only 4~8 wt% of particles is enough to stabilize a network structure of domain size less than 100 μm (see Figure 57) for PI/PDMS system, while 3~6 wt% of particles can stabilize the bicontinuous structure of domain size sub-millimeter (see Figure 40). Thus, we presume that the thermodynamic picture of type 1 in Figure 52b (with a deep particle desorption well) may closely represent the PI/PDMS system.

6.4.2 Bulk rheological evidence to support the interfacial effect hypothesis

We aim to distinguish the interfacial effect and the bulk effect in this section. We utilize rheology to provide us information. To sum, three key observations in this chapter includes:

1. Stabilization of a transient network structure into a stable network structure by adding sufficient particles

2. Delayed and incomplete capillary instability of strings due to the presence of particles

3. No shape relaxation of elongated or any non-spherical structures due to the presence of particles

We have presumed that all of these observations were mainly attributed by the presence of particles at the interface (i.e. interfacial effect), instead of the presence of particles inside the polymer phase (i.e. bulk effect). This hypothesis is based on several supporting evidence as follows:

(1) Detailed microscopic observation: some of the micrographs clearly show that the interior of drops, which are the PIB phase for the PI60 composition, contained few particles as we change the focal planes (for example, Figure 58). Darker outlines of drops and other structures suggest particle adsorption at the interface.

(2) Localized and persistent non-relaxation of nonspherical structures: The non-relaxation behavior of non-spherical drops is often localized and persistent during a long observation time. We believed that the bulk effect can only slow down the retraction, but it cannot arrest the structure for such a long time (15~20 hr) at the particle loadings of study, which are far below percolation threshold of particles in 3D space. However, interfacial jamming requires much lower particle loadings, and it can achieve long-term stability if the interface becomes immobile.

(3) At the low particle loading (0.25~8 wt% or 0.06~2 vol%), the bulk effect is expected to be weak.

To further support our hypothesis on the interfacial attribution, we provide bulk rheology for the particle dispersions. Particles left in the bulk are expected to affect the fluid components. If both of the fluid components are Newtonian, we can attribute the blend behavior to interfacial effect. We present the oscillatory data for the components and two concentrations of particle dispersion (1wt% and 8 wt%) for both particle in PI and PDMS phase.

Figure 79a shows the dynamic oscillatory results. For particle dispersion in PDMS, as we increase the particle weight percentage from 0% (pure component), 1% to 8%, the storage modulus (G') curves barely change. The complex viscosity curves are essentially identical for pure PDMS and 1% dispersion, but 8 % dispersion has higher complex viscosity. The three curves for complex viscosity are flat at the low frequency region, which is an indication that the

fluids are Newtonian. Newtonian behavior is important evidence because only if the drop phase fluid is Newtonian, we may attribute the three key observations above to interfacial effect. If the drop phase is non-Newtonian, we expect that the drop deformation and retraction will be affected. Figure 80 shows the micrograph of the particle dispersion in PDMS. The particles are uniformly distributed and have no obvious structure even at 16 wt% in PDMS. This is mutually supportive to the bulk rheology measurements of particle-PDMS dispersions. Figure 79b shows the bulk rheology for particle-PI dispersions. The 1wt% particle-PI dispersion behaves almost identical to pure component PI; there is little effect on the viscosity, and the G' curves overlap above 2 rad/s in frequency. On the other hand, the oscillatory behavior of the 8wt% particle-PI dispersion deviates from that of pure PI: the complex viscosity curve has a decreasing trend, indicating shear thinning, and the G' curve also deviates from that of pure PI. These non-Newtonian behavior, however, are expected as we have learned in Section 5.3.1 that FeOOH particles in PI can associate with each other to form aggregated structures (see Figure 36d).

In summary, bulk rheology supports partially our hypothesis. The particle-PDMS dispersions are Newtonian fluids up to at least 8 wt%, while the 8 wt% particle-PI dispersion is not Newtonian. For both of the 1% particle dispersions, they are essentially Newtonian and essentially no effect on increasing the complex viscosity. As mentioned above, micrographs show little particles left in the bulk phases. At such a low particle concentration in the bulk, we believe that the bulk contribution to the three key observations is little. Therefore, we attribute the non-relaxation of elongated structures, the particle-stabilized network structures, and the delayed and incomplete capillary instability, mainly to the interfacial effect. Especially, the very slow kinetics (essentially no relaxation) suggests that interfacial jamming should have occurred.
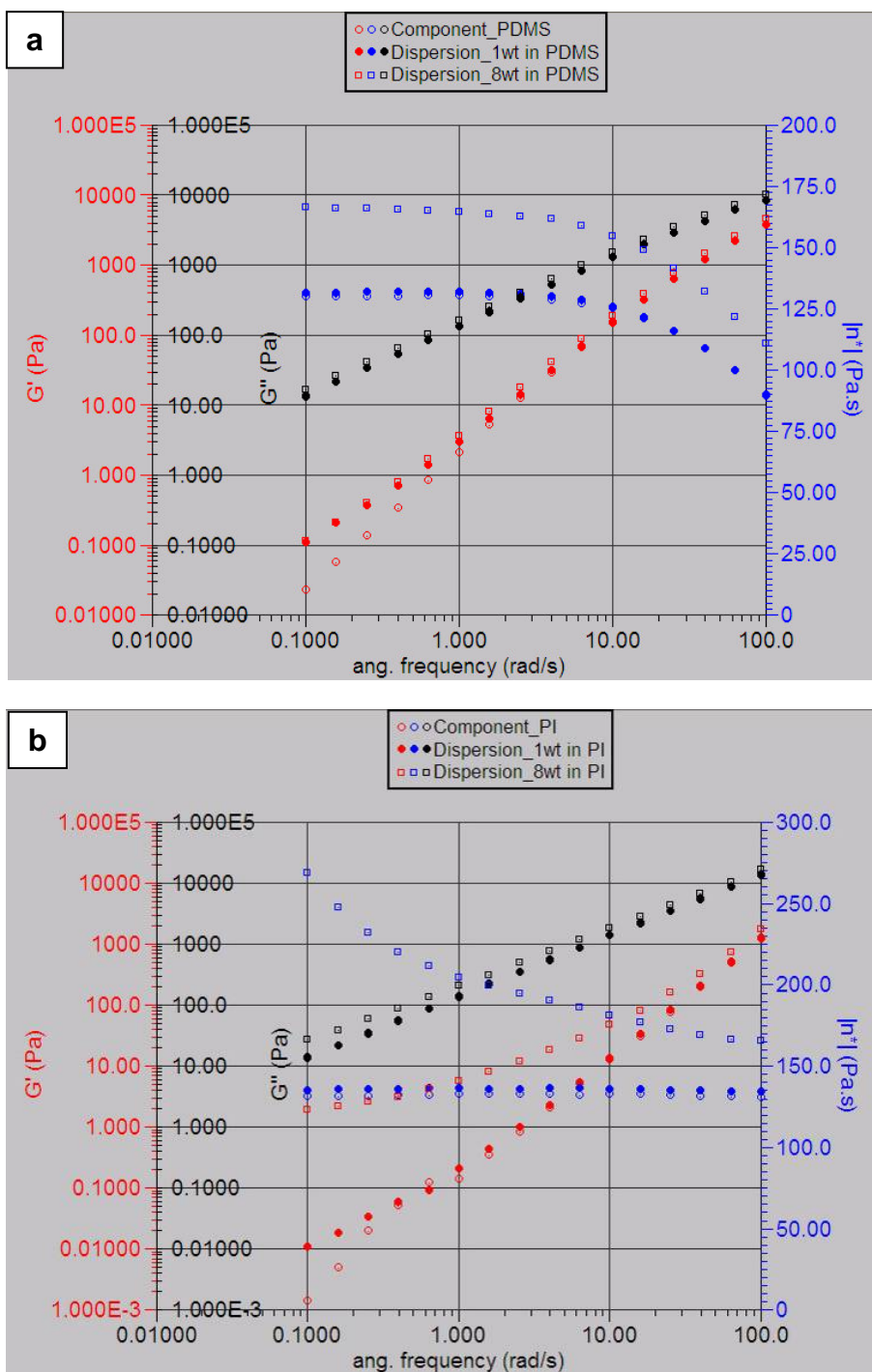
Figure 79. Dynamic oscillatory results of pure components, particle-PDMS dispersions and particle-PI dispersions. (a)Component PDMS, and 1wt% and 8wt% particles-PDMS dispersion. (b)Component PI, and 1wt% and 8wt% particles-PI dispersion

180
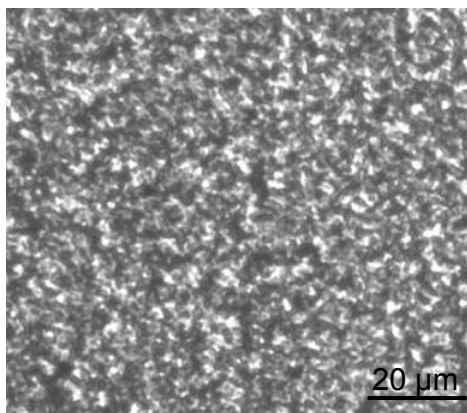
Figure 80. Particle-PDMS dispersion at 16 wt%.
The dispersion is homogeneous and contains no aggregated structures. The scale bar is 20 μm.

6.5   CONCLUSIONS

In this chapter, we further extend the application of particle jamming to control the morphology of a droplet-matrix PI/PDMS blend. The flow-generated elongated drops do not relax the nonspherical shape during a long observation time (~16 hr). Thus, interfacially-active particles can be used to control the morphology of blends, presumably via interfacial particle jamming. These elongated drops are expected to make the structure anisotropic.   An anisotropic polymer blend may have potential to be a structural material that has stronger mechanical strength in the direction parallel to the long axis of elongated drops.

We also discovered the particle-assisted network structure in the PI/PDMS system, which is well studied and known to be droplet-matrix. Transient network structures were also found in the particle-free blends. We hypothesized that the formation of network structure is due to random drop coalescence during the blending. We attributed the stabilization of network to particle adsorption and interfacial particle jamming.

7.0   SUMMARY AND FUTURE WORK

This thesis provides a broad investigation on behaviors of particle-laden interfaces. The covered topics span from oil/water interfaces to polymer/polymer interfaces. The morphologies of interest include both the droplet-matrix morphology and the bicontinuous morphology.

Fundamental understanding on two interface-attributed phenomena, spreading and jamming, has been obtained; applications of interfacial jamming on controlling the morphologies of polymer blends have been demonstrated. Thereby, our contributions include:

- Comprehensive study on the film-climbing phenomenon in unstable Pickering emulsions; including generality of film-climbing, film structure, surface pressure calculation and measurements, substrate hydrophobicity and prewetting, and the correlation of the wall-coverage with film mobility and wrinkling.

- Development of the spinning drop tensiometer method to study interfacial jamming; first effort to conduct a systematic study on interfacial-tension-driven jamming without using an externally-imposed monolayer compression; identification of shape hysteresis, dynamics-dependence, and the monolayer behavior at a nonpolar/nonpolar fluid interface.

- Demonstration the effectiveness of interfacial jamming on stabilizing a bicontinuous polymer blend; realization the particle-polymer composite material, bijel; recognition the asymmetry of mixing sequence; hypothesis of the flow-induced mixing/demixing

and a proposal of particle transfer/adsorption mechanism.

- The discovery of particle-assisted network structures and transient network structure in PI/PDMS blends; investigation of the relaxation kinetics of flow-induced jammed morphology; observation of the delayed capillary instability and drop retraction; correlating rheological measurements to morphology visualization.

As there are endless possibilities of particle-laden interfaces, our contribution would be like a letter in the dictionary of interfacial phenomena. The study presented in this dissertation could hardly be complete and comprehensive. In the following, thereby we list some future work related to this dissertation.

The future work for PI/PIB blends would be:

- To use the parallel-plate geometry with a large gap size in rheometer to verify the speculation of surface wetting effect on collapsing the bicontinuous structure in a confined geometry.

- To support the flow-induced mixing hypothesis by viscosity measurements in a rheometer.

- To extract the domain coarsening rate from a large quantity of images and to quantify the effect of jamming.

The future work for PI/PDMS blends would be:

- To obtain the intermediate steps on the stabilization process of the particle-assisted network structure.

In the future, we wish to study the relaxation behavior of a promptly-jammed particle monolayer using the spinning drop tensiometer technique. This 2D glass relaxation may be an analog to the well-appreciated 3D glass transition. We suspect that the area of a slightly-jammed monolayer can spontaneously reduce its area because the phase in which the monolayer is being trapped is not a thermodynamically-defined phase. Much insight on the nature of the jamming transition can be elucidated.

BIBLIOGRAPHY

1. Pickering, S. U., Emulsions. *Journal of the Chemical Society, Transactions* **1907,** 91, 2001-2021.

2. Kralchevsky, P. A.; Paunov, V. N.; Ivanov, I. B.; Nagayama, K., Capillary Meniscus Interaction between Colloidal Particles Attached to a Liquid-Fluid Interface. *J. Coll. Int. Sci.* **1992,** 151, (1), 79-94.

3. Pieranski, P., Two-dimensional interfacial colloidal crystals. *Phys. Rev. Lett.* **1980,** 45, (7), 569-572.

4. Aveyard, R.; Clint, J. H.; Nees, D.; Quirke, N., Structure and collapse of particle monolayers under lateral pressure at the octane/aqueous surfactant solution interface. *Langmuir* **2000,** 16, (23), 8820-8828.

5. Subramaniam, A. B.; Abkarian, M.; Mahadevan, L.; Stone, H. A., Non-spherical bubbles. *Nature* **2005,** 438, (7070), 930-930.

6. Melle, S.; Lask, M.; Fuller, G. G., Pickering emulsions with controllable stability. *Langmuir* **2005,** 21, (6), 2158-2162.

7. Alargova, R. G.; Warhadpande, D. S.; Paunov, V. N.; Velev, O. D., Foam superstabilization by polymer microrods. *Langmuir* **2004,** 20, (24), 10371-10374.

8. Thareja, P.; Ising, B. P.; Kingston, S. J.; Velankar, S. S., Polymer foams stabilized by particles adsorbed at the air/polymer interface. *Macromolecular Rapid Communications* **2008,** 29, (15), 1329-1334.

9. Dinsmore, A. D.; Hsu, M. F.; Nikolaides, M. G.; Marquez, M.; Bausch, A. R.; Weitz, D. A., Colloidosomes: Selectively permeable capsules composed of colloidal particles. *Science* **2002,** 298, (5595), 1006-1009.

10. Lin, Y.; Skaff, H.; Emrick, T.; Dinsmore, A. D.; Russell, T. P., Nanoparticle assembly and transport at liquid-liquid interfaces. *Science* **2003,** 299, (5604), 226-229.

11. Wang, D. Y.; Duan, H. W.; Mohwald, H., The water/oil interface: the emerging horizon for self-assembly of nanoparticles. *Soft Matter* **2005,** 1, (6), 412-416.

185

12. Stratford, K.; Adhikari, R.; Pagonabarraga, I.; Desplat, J. C.; Cates, M. E., Colloidal jamming at interfaces: A route to fluid-bicontinuous gels. *Science* **2005,** 309, (5744), 2198-2201.

13. Kim, B. J.; Fredrickson, G. H.; Hawker, C. J.; Kramer, E. J., Nanoparticle surfactants as a route to bicontinuous block copolymer morphologies. *Langmuir* **2007,** 23, (14), 7804-7809.

14. Balazs, A. C.; Emrick, T.; Russell, T. P., Nanoparticle polymer composites: Where two small worlds meet. *Science* **2006,** 314, (5802), 1107-1110.

15. Subramaniam, A. B.; Mejean, C.; Abkarian, M.; Stone, H. A., Microstructure, morphology, and lifetime of armored bubbles exposed to surfactants. *Langmuir* **2006,** 22, (14), 5986-5990.

16. Cheng, H. L.; Velankar, S. S., Film climbing of particle-laden interfaces. *Coll. Surf. A* **2008,** 315, (1-3), 275-284.

17. Cheng, H. L.; Velankar, S. S., Controlled Jamming of Particle-Laden Interfaces Using a Spinning Drop Tensiometer. *Langmuir* **2009,** 25, (8), 4412-4420.

18. Kralchevsky, P. A.; Denkov, N. D.; Danov, K. D., Particles with an undulated contact line at a fluid interface: Interaction between capillary quadrupoles and rheology of particulate monolayers. *Langmuir* **2001,** 17, (24), 7694-7705.

19. Danov, K. D.; Kralchevsky, P. A.; Naydenov, B. N.; Brenn, G., Interactions between particles with an undulated contact line at a fluid interface: Capillary multipoles of arbitrary order. *J. Coll. Int. Sci.* **2005,** 287, (1), 121-134.

20. Loudet, J. C.; Alsayed, A. M.; Zhang, J.; Yodh, A. G., Capillary interactions between anisotropic colloidal particles. *Phys. Rev. Lett.* **2005,** 94, (1).

21. Horozov, T. S.; Aveyard, R.; Clint, J. H.; Binks, B. P., Order-disorder transition in monolayers of modified monodisperse silica particles at the octane-water interface. *Langmuir* **2003,** 19, (7), 2822-2829.

22. Binks, B. P.; Lumsdon, S. O., Influence of particle wettability on the type and stability of surfactant-free emulsions. *Langmuir* **2000,** 16, (23), 8622-8631.

23. Binks, B. P.; Clint, J. H., Solid wettability from surface energy components: Relevance to pickering emulsions. *Langmuir* **2002,** 18, (4), 1270-1273.

24. Binks, B. P., Particles as surfactants - similarities and differences. *Curr. Opin. Coll. Int. Sci.* **2002,** 7, (1-2), 21-41.

25. Binks, B. P.; Lumsdon, S. O., Pickering emulsions stabilized by monodisperse latex particles: Effects of particle size. *Langmuir* **2001,** 17, (15), 4540-4547.

26. Horozov, T. S.; Binks, B. P., Particle-stabilized emulsions: A bilayer or a bridging monolayer? *Angew. Chemie-Int. Ed.* **2006,** 45, (5), 773-776.

27. Stancik, E. J.; Fuller, G. G., Connect the drops: Using solids as adhesives for liquids. *Langmuir* **2004,** 20, (12), 4805-4808.

28. Stancik, E. J.; Kouhkan, M.; Fuller, G. G., Coalescence of particle-laden fluid interfaces. *Langmuir* **2004,** 20, (1), 90-94.

29. Aveyard, R.; Clint, J. H.; Nees, D.; Paunov, V. N., Compression and structure of monolayers of charged latex particles at air/water and octane/water interfaces. *Langmuir* **2000,** 16, (4), 1969-1979.

30. Schwartz, H.; Harel, Y.; Efrima, S., Surface behavior and buckling of silver interfacial colloid films. *Langmuir* **2001,** 17, (13), 3884-3892.

31. Horozov, T. S.; Binks, B. P.; Aveyard, R.; Clint, J. H., Effect of particle hydrophobicity on the formatlon and collapse of fumed silica particle monolayers at the oil-water interface. *Coll. Surf. A* **2006,** 282, 377-386.

32. Xu, H.; Melle, S.; Golemanov, K.; Fuller, G., Shape and buckling transitions in solid-stabilized drops. *Langmuir* **2005,** 21, (22), 10016-10020.

33. Monteux, C.; Kirkwood, J.; Xu, H.; Jung, E.; Fuller, G. G., Determining the mechanical response of particle-laden fluid interfaces using surface pressure isotherms and bulk pressure measurements of droplets. *Phys. Chem. Chem. Phys.* **2007,** 9, (48), 6344-6350.

34. Vella, D.; Aussillous, P.; Mahadevan, L., Elasticity of an interfacial particle raft. *Europhys. Lett.* **2004,** 68, (2), 212-218.

35. Paul, D. R.; Barlow, J. W., Polymer blends (or alloys). *J. Macromol. Sci. Revs. Macromol. Chem.* **1980,** C18, 109-168.

36. Potschke, P.; Paul, D. R., Formation of Co-continuous structures in melt-mixed immiscible polymer blends. *J. Macromol. Sci.-Polym. Rev* **2003,** C43, (1), 87-141.

37. Grace, H. P., Dispersion phenomena in high viscosity immiscible fluid systems and applications of static mixers as dispersion devices. *Chem. Eng. Comm.* **1982,** 14, 225-277.

38. Fenouillot, F.; Cassagnau, P.; Majeste, J. C., Uneven distribution of nanoparticles in immiscible fluids: Morphology development in polymer blends. *Polymer* **2009,** 50, (6), 1333-1350.

39. Larson, R. G., Flow-Induced Mixing, Demixing, and Phase-Transitions in Polymeric Fluids. *Rheol. Acta* **1992,** 31, (6), 497-520.

40. Wolf, B. A., Theoretical description of phase separation in flowing polymer solutions. *Macromolecular Chemistry Rapid Communications* **1980,** 1, 231.

41. Silberberg, A.; Kuhn, W., Miscibility of liquids influenced by rate of shear. *Nature* **1952,** 170, 450.

42. Utracki, L. A., *Polymer Blend Handbook*. Kluwer Academic Publishers: 2003; p 170-171.

43. Chung, H.; Ohno, K.; Fukuda, T.; Composto, R. J., Self-regulated structures in nanocomposites by directed nanoparticle assembly. *Nano Lett.* **2005,** 5, (10), 1878-1882.

44. Veenstra, H.; Van Dam, J.; de Boer, A. P., On the coarsening of co-continuous morphologies in polymer blends: effect of interfacial tension, viscosity and physical cross-links. *Polymer* **2000,** 41, (8), 3037-3045.

45. Yuan, Z. H.; Favis, B. D., Coarsening of immiscible co-continuous blends during quiescent annealing. *AIChE J.* **2005,** 51, (1), 271-280.

46. Tomotika, S., On the instability of a cylindrical thread of a viscous liquid surrounded by another viscous fluid. *Proc. Roy. Soc. Lon.* **1935**, 322-337.

47. Clegg, P. S., Fluid-bicontinuous gels stabilized by interfacial colloids: low and high molecular weight fluids. *J. Phys.-Condes. Matter* **2008,** 20, (11).

48. Kim, E.; Stratford, K.; Adhikari, R.; Cates, M. E., Arrest of fluid demixing by nanoparticles: A computer simulation study. *Langmuir* **2008,** 24, (13), 6549-6556.

49. Herzig, E. M.; White, K. A.; Schofield, A. B.; Poon, W. C. K.; Clegg, P. S., Bicontinuous emulsions stabilized solely by colloidal particles. *Nature Materials* **2007,** 6, (12), 966-971.

50. Vinckier, I.; Moldenaers, P.; Mewis, J., Elastic Recovery of immiscible blends 1. Analysis after steady state shear flow. *Rheol. Acta* **1999,** 38, (1), 65-72.

51. Thareja, P. Study of particles at fluid-fluid interfaces. University of Pittsburgh, Pittsburgh, 2008.

52. Vinckier, I.; Moldenaers, P.; Terracciano, A. M.; Grizzuti, N., Droplet size evolution during coalescence in semiconcentrated model blends. *AIChE J.* **1998,** 44, (4), 951-958.

53. Palierne, J. F., Linear rheology of viscoelastic emulsions with interfacial tension. *Rheol. Acta* **1990,** 29, 204-214.

54. Graebling, D.; Muller, R.; Palierne, J. F., Linear viscoelastic behavior of some incompatible polymer blends in the melt. Interpretation of data with a model of emulsion of viscoelastic liquids. *Macromolecules* **1993,** 26, (2), 320-329.

55. Oldroyd, J. G., The elastic and viscous properties of emulsions and suspensions. *Proc. Roy. Soc. Lon.* **1953,** A218, 122-132.

56. Brandriss, S.; Margel, S., Synthesis and Characterization of Self-Assembled Hydrophobic Monolayer Coatings on Silica Colloids. *Langmuir* **1993,** 9, (5), 1232-1240.

57. Thareja, P.; Velankar, S. S., Particle-induced bridging in immiscible polymer blends. *Rheol. Acta* **2007,** 46, (3), 405-412.

58. Mayya, K. S.; Sastry, M., A new technique for the spontaneous growth of colloidal nanoparticle superlattices. *Langmuir* **1999,** 15, (6), 1902-1904.

59. Binks, B. P.; Clint, J. H.; Fletcher, P. D. I.; Lees, T. J. G.; Taylor, P., Growth of gold nanoparticle films driven by the coalescence of particle-stabilized emulsion drops. *Langmuir* **2006,** 22, (9), 4100-4103.

60. Xu, H.; Goedel, W. A., Particle-assisted wetting. *Langmuir* **2003,** 19, (12), 4950-4952.

61. Goedel, W. A., A simple theory of particle-assisted wetting. *Europhys. Lett.* **2003,** 62, (4), 607-613.

62. Binks, B. P.; Clint, J. H.; Fletcher, P. D. I.; Lees, T. J. G.; Taylor, P., Particle film growth driven by foam bubble coalescence. *Chem. Comm.* **2006**, (33), 3531-3533.

63. Asekomhe, S. O.; Chiang, R.; Masliyah, J. H.; Elliott, J. A. W., Some observations on the contraction behavior of a water-in-oil drop with attached solids. *Ind. Eng. Chem. Res.* **2005,** 44, (5), 1241-1249.

64. Aveyard, R.; Binks, B. P.; Clint, J. H.; Fletcher, P. D. I.; Horozov, T. S.; Neumann, B.; Paunov, V. N.; Annesley, J.; Botchway, S. W.; Nees, D.; Parker, A. W.; Ward, A. D.; Burgess, A. N., Measurement of long-range repulsive forces between charged particles at an oil-water interface. *Phys. Rev. Lett.* **2002,** 88, (24).

65. Basavaraj, M. G.; Fuller, G. G.; Fransaer, J.; Vermant, J., Packing, flipping, and buckling transitions in compressed monolayers of ellipsoidal latex particles. *Langmuir* **2006,** 22, (15), 6605-6612.

66. Vonnegut, B., Rotating bubble method for the determination of surface and interfacial tensions. *Rev. Sci. Inst.* **1942,** 13, 6-9.

67. Martin, J. D.; Velankar, S., Effect of surfactant on the viscous Raleigh-Tomotika instability. *In preparation*.

68. Martin, J. D.; Velankar, S. S., Unusual behavior of PEG/PPG/Pluronic interfaces studied by a spinning drop tensiometer. *J. Coll. Int. Sci.* **2008,** 322, (2), 669-674.

69.   de Hoog, E. H. A.; Lekkerkerker, H. N. W., Breakup of an elongated droplet in a centrifugal field. *J. Phys. Chem. B* **2001,** 105, (47), 11636-11640.

70.   Liu, A. J.; Nagel, S. R., Nonlinear dynamics - Jamming is not just cool any more. *Nature* **1998,** 396, (6706), 21-22.

71.   Safouane, M.; Langevin, D.; Binks, B. P., Effect of particle hydrophobicity on the properties of silica particle layers at the air-water interface. *Langmuir* **2007,** 23, (23), 11546-11553.

72.   Si, M.; Araki, T.; Ade, H.; Kilcoyne, A. L. D.; Fisher, R.; Sokolov, J. C.; Rafailovich, M. H., Compatibilizing bulk polymer blends by using organoclays. *Macromolecules* **2006,** 39, (14), 4793-4801.

73.   Vinckier, I.; Laun, H. M., Manifestation of phase separation processes in oscillatory shear: droplet-matrix systems versus co-continuous morphologies. *Rheol. Acta* **1999,** 38, 274-286.

74.   Thareja, P.; Velankar, S. S., Interfacial activity of particles at PI/PDMS and PI/PIB interfaces: analysis based on Girifalco-Good theory. *Coll. Polym. Sci.* **2008,** 286, (11), 1257-1264.

75.   Montfort, J. P.; Marin, G.; Arman, J.; Monge, P., Blending law for binary blends of fractions of linear polystyrene. *Polymer* **1978,** 19, (3), 277-284.

76.   Kitade, S.; Ichikawa, A.; Imura, N.; Takahashi, Y.; Noda, I., Rheological properties and domain structures of immiscible polymer blends under steady and oscillatory shear flows. *J. Rheol.* **1997,** 41, (5), 1039-1060.

77.   Van Hemelrijck, E.; Van Puyvelde, P.; Velankar, S.; Macosko, C. W.; Moldenaers, P., Interfacial elasticity and coalescence suppression in compatibilized polymer blends. *J. Rheol.* **2004,** 48, (1), 143-158.

78.   Van Hemelrijck, E.; Van Puyvelde, P.; Macosko, C. W.; Moldenaers, P., The effect of block copolymer architecture on the coalescence and interfacial elasticity in compatibilized polymer blends. *J. Rheol.* **2005,** 49, (3), 783-798.

79.   Binks, B. P.; Lumsdon, S. O., Transitional phase inversion of solid-stabilized emulsions using particle mixtures. *Langmuir* **2000,** 16, (8), 3748-3756.

80.   Thareja, P.; Moritz, K.; Velankar, S. S., Effect of interfacially-active particles on the drop size in blends of model immiscible homopolymers. *submitted* **2009**.

81.   Liu, A. J.; Nagel, S. R., *Jamming and Rheology*. Taylor & Francis: London, 2000.